A CASE STUDY OF BLAST VIBRATION MODELLING IN THE HANASON SERVTEX QUARRY, GARDEN RIDGE CITY, TEXAS

A Thesis

by

MOHAMED MAHMOUD AHMED RADWAN

Submitted to the Office of Graduate and Professional Studies of
Texas A&M University
in partial fulfillment of the requirements for the degree of

MASTER OF SCIENCE

Chair of Committee,	Mark Everett
Committee Members,	Christopher Mathewson
	Minsu Cha
Head of Department,	Michael Pope

December 2016

Major Subject: Geophysics

ABSTRACT

Comprehensive evaluation of the vibrations transmitted to the site from external sources constitute a significant environmental facet of building and facility design. External sources include, but are not limited to railways, machinery, highway traffic, and quarrying operations. The vibrations magnitudes is crucial to assess if we aim to properly predict the levels of excitation at buildings near vibration sources. However, predicting vibrations in terms of both amplitudes and frequency is problematic. This complication occurred due to the lack of a full understanding of seismic wave propagation in soil, uncertainty of soil properties, and the lack of accurate models for vibration sources and the resulting near- and far-field behavior. Nevertheless, in spite of these and other obstacles, it is conceivable to use available empirical and numerical data to make realistic assessments of the propagating waves. Blast vibrations are an inescapable occurrence in the vicinity of quarries, if blasting techniques are used in quarrying operations. Vibrations may degrade the environment, and cause annoyance to the population in the neighborhood of the quarry.

In the study area, it has been found that the changes in the peak particle velocity (PPV) is more influenced by the degree of consolidation and the direction of fractures rather than by the types of lithology. Given the fact that, the tectonics' normal fault will produce two types of zones, the consolidated (downthrown, up thrown) and the unconsolidated, the analysis of the PPV and frequency was attributed to the mechanism of wave propagation in the body of these materials. Furthermore, due to the coverage of a large range of measurements and the complex tectonics involved, 5 propagation

mechanisms have been proposed for the explanation of the data. Effect of fractures and fluid saturations and faults has been incorporated in the analysis.

There are no significant lithology differences inside each of the specified zones, so the wave propagation in each material was not considered as a tool to differentiate between the different zones. However, different locations in the same zone showed an amplification and attenuation in the PPV, even though they were measured at the same scaled distance (equal blasting energy). This was attributed to the transmission of the wave at the boundary (sedimentary contact or fracture) for different formations such as limestone and clay (the predominant lithology in the area).

This thesis is describing the process of different model constructions and validations for the five mechanisms using empirical and numerical models. A qualitative geological interpretation has been given, exploiting the optimized parameters of the models.

.

DEDICATION

I dedicate this thesis to my family for their continuous support and encouragement

ACKNOWLEDGEMENTS

I would like to express my sincere appreciation to my supervisor, Professor Dr. Mark Everett. I am grateful for his assistance and guidance throughout my studies and research. I am heartily thankful to him, whose encouragement, management, and support from the preliminary to the concluding level enabled me to develop an understanding of this subject.

I wish to extend my appreciation to Dr. Christopher and Dr. Cha for devoting their invaluable time to review my research work and evaluate its results. Their comments during the course of my studies are highly appreciated.

I would like to thank George Hyde for his help in providing the data and knowledge in this project.

I wish to express my love and gratitude to my beloved family for their understanding and endless support shown throughout the duration of my study.

I would like to thank Christine Noshi for her great support and passion that she provided throughout the program.

NOMENCLATURE

ANNs	Artificial Neural Networks
PPV	Peak Particle Velocity
AOP	Air Over Pressure
FFBP	Feedforward Back Propagation Neural Networks
CFBP	Cascade-Forward Back Propagation Neural Networks
FEA	Finite Element Analysis
SRA	Source-Receiver Azimuth

TABLE OF CONTENTS

Page

LIST OF FIGURES

LIST OF TABLES

CHAPTER I

INTRODUCTION

1.1 Statement of Problem and Motivation

Various sources of vibrations are involved in construction and mining projects such as blasting, heavy equipment, pile driving and dynamic compaction. Elastic vibrations that are generated by these sources may harmfully affect the nearby residential areas. Their effects include annoyance of people and cosmetic and structural damage to the buildings. Comprehensive evaluation of the vibrations transmitted to the site from external sources constitute a significant environmental facet of building and facility design. External sources include, but are not limited to railways, machinery, highway traffic, and quarrying operations. The vibrations magnitudes is crucial to assess if we aim to properly predict the levels of excitation at buildings near vibration sources. However, predicting vibrations in terms of both amplitudes and frequency is problematic. This complication occurred due to the lack of a full understanding of seismic wave propagation in soil behavior, the difficulty in defining accurate values of soil properties, and the difficulty of accurately modeling the sources of vibration and the resulting near- and far-field behavior. Nevertheless, in spite of these and other obstacles, it is conceivable use available empirical and numerical data to make realistic assessments of the propagating waves. Blast vibrations are an inescapable occurrence in the vicinity of quarries, if blasting techniques are used in quarrying operations. Vibrations may degrade the environment, and cause annoyance to the population in the neighborhood of the quarry.

Rock blast vibrations are an inescapable occurrence in the vicinity of quarries, if raw material is to be obtained by blasting techniques. Vibrations may degrade the quality of life and property values, particularly in the case of a dense population living in the neighborhood of the quarry. Generally, observations of peak particle velocities (PPV) values are used in efforts toward reduction of ground vibrations and increase safety. A number of empirical equations between PPV, the charge weight and source-receiver distance have been presented in the literature.

More advanced numerical approaches used to predict ground vibrations involve the analysis of block systems (Mortazavi and Katsabanis., 2001). In such approaches, authors formulated systems of simultaneous equations and solved them by minimizing the energy required to bring the system into equilibrium.

On the empirical side, the Federal Institute for Geosciences and Natural Resources (BGR) recorded vibrations of more than 400 production blasts in the vicinity of about 150 quarries. Large scatter was observed in plots of amplitude versus distance. This scatter makes it mandatory to continue to search for alternative techniques to understand the vibration transmission caused by rock blasting.

Vibration problems can be separated into two classes. The first class, which is the focus of the present research, concerns vibrations with small amplitudes where the main effect is on human perception or on sensitive instruments. Acceptable vibration levels are very low and often specified on a subjective basis determined by complaints of the residents. The second class, which is not of concern here, involves vibrations which are large enough to cause or contribute to significant (i.e. non-cosmetic) damage of structures.

These cases are not common in quarry blasting but can be of concern in densely populated areas or near vibration-sensitive structures, such as fragile historic monuments or buildings on poor foundations. It is difficult to correlate ground motion features induced by a quarry blast to damage of surface structures. Peak particle velocity (PPV) is considered the most appropriate vibration parameter in quarrying that can be used to assess potential damaging ground motions to structures. Maximum allowable vibration levels in terms of PPV for buildings near blasting operations have been suggested, according to various field measurements in the past several decades, The USBM (United States Bureau of Mines) set acceptable PPV values at 23 mm/s for structures located on hard rock, 11 mm/s for those on weak rock and 6 mm/s for those on soil (Siskind, 1980). However, to obtain these values the study included only low-rise residential buildings. Therefore these criteria might not always apply in practice for assessing structural safety. This is due primarily to the fact that the USBM standards do not fully consider the range of effects of structural type, structural condition, subsurface geology and conditions near the source.

1.2 Case Study

The Hanson-Servtex limestone quarry is the site of the case study that forms the focus of this research. The quarry is located in Comal County, Texas and is situated on ~3,000 acres near the Balcones fault zone. The quarry is owned and operated by the Hanson Company which acquired the operations in 1977 from Servtex Materials Company. The quarry was started in 1936 by two local New Braunfels, Texas, citizens. Most of the quarry blasting operations are now performed within the limits of the adjacent city of Garden Ridge. Despite the efforts by the blaster to undergo required design and safety measures that ensures acceptable vibrations levels as stipulated by USBM, the vibrations have become a source of annoyance for residents living near the quarry. As a result, a number of complaints have been received by the Garden Ridge city office due to blasting activities in the quarry. People are sensitive to both the air overpressure and the ground vibrations which they fear might be causing cosmetic or even structural damage to their homes.

Although the vibration levels obtained in the vast majority of the activities are well within the stated limits, complaints have persisted. The spatial and temporal distribution of the complaints can be extracted from information recorded by the city. The quarry is located in the Balcones faults zone which is characterized by complex geological structure due to its tectonic history. The geological structure likely plays a large role in determining vibrations levels at a particular site. A number of questions can be raised in order to understand how the vibrations are distributed within the study area, such as:

- How has the site geology affected the spatial distribution of complaints?

- Can key parameters be determined from ground vibrations to enable the establishment of tolerable noise level and maximum allowable PPV specifically for the Garden Ridge City site conditions?
- What will this maximum allowable PPV be with respect to the USBM and other international standards?
- Can the quarry activities be correlated to any cosmetic or structural damage to buildings, or harm to individuals, specifically in Garden Ridge city?

Of these important questions, the focus here will be on just the first question, namely the effect of site geology on ground vibrations observed in the residential areas of Garden Ridge near the quarry.To answer this question a number of data analysis and modelling procedures will be followed which aim at understanding the spatial distributions of observed ground vibrations and complaints in the study area. Then a set of possible geological interpretations will be derived from the observations and modelling results.

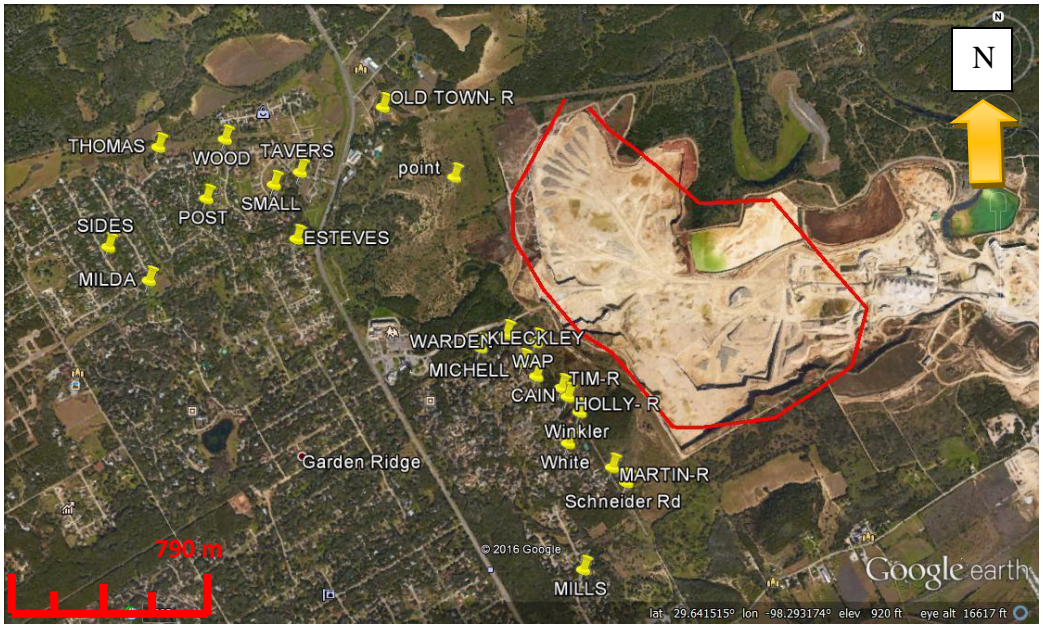

Figure 1.1: location of the studied quarry (red polygon). The yellow pushpins show the receivers locations.

1.3 Objectives and Strategies Applied

The research objective of this thesis is to study the effect of site geology on ground vibrations due to blasting at the Hanson Servtex quarry site. This study of geology aims to develop better understanding of the vibration response. This will aid in determining acceptable levels of vibrations for the nearby inhabitants and to protect the surrounding structures. The research is particularly significant for surface blasts near residential areas, in order to reduce the induced vibrations to within an acceptable limit. In the present study, ground motions were recorded at different distances from the source, and in different azimuths with respect to the predominant strike of geological faults and joints. A total of 4 years of vibration records are provided for public use by Vibra-Tech Company. The

study has been divided into two phases which analyze these data and present the results of three types of modelling procedures. These stages are summarized as follows:

1.3.1 Phase I

The purpose of the first phase is to understand how the propagation and attenuation of seismic waves is affected by spatially heterogeneous geological structures beneath the study area. Surface seismic measurements such as peak particle velocity and dominant vibration frequencies will be analyzed. The analysis is based on publicity available vibration data that is recorded in the three mutually perpendicular directions (longitudinal, transverse, and vertical) at 22 receivers at different distances and involving different source characteristics. The analysis is conducted through the implementation of the following tasks:

1) Azimuthal plots at each receiver are analyzed using semi-empirical equations in order to determine attenuation coefficient values for different source-receiver azimuths.
2) Nonlinear regression is used to determine optimum values of the parameters that appear in different semi-empirical equations.
3) Plots of the PPV versus frequency are made for each receiver in order to classify geological zones comprising the surrounding residential area.
4) The ability of different artificial intelligent methods to predict wave propagation parameters in the study area is tested. Methods such as neural networks are studied.
5) A comparative study will be performed between the different prediction methods by analyzing correlations between modeled responses and the measured data.

1.3.2 Results of Phase I

Phase I results are as follows:

1. Possible geological scenarios that explain the azimuthal distribution of the seismic wave propagation around the quarry. This information could be used for predicting the peak particle velocity and the dominant frequency at different distances and source characteristics.
2. Exploration of effects of geology on ensuring acceptable levels of the ground vibrations from the blasting. This is done by comparing the modelling results to nationally accepted criteria.

1.3.3 Phase II

Phase II is focused on building a finite element model to analyze ground vibrations at the study area. Different types of data such as well logs (sonic, neutron, and formation tops) and structural geological maps are brought together from different sources in order to minimize uncertainty of the finite element model. The results from the previous phase are also used as constraints. The development of the finite element modeling is summarized in the following steps:

1. Geometry building (geological structure).
2. Materials definition and specification (different material models will be used).
3. Mesh Generation (different types of meshing will be tested).
4. Boundary Conditions specification.
5. Generating the dynamic load (specifying the blasting parameters).
6. Time history analysis after applying the load.

7. Validation of the results by the actual measurements.

1.3.4 Results of Phase II

Phase II results are as follows:

1- A quantitative model for seismic wave propagation in the study area is explored as a function of source characteristics.

2- A more precise understanding of the spatial distribution of the observed ground vibrations.

CHAPTER II

FUNDAMENTALS OF WAVE PROPAGATION

The dynamic effect of blasting vibrations on adjacent and distant structures is influenced mainly by the geological structure beneath the site and the susceptibility of the affected structures. It is likely that potentially damaging vibrations may be induced in close vicinity to building foundations, but longer term settlements resulting from soil vibrations in loose and unconsolidated soils could also occur at various spacing from the blasting source. Generally, the effect of the elastic soil deformation on buildings may cause different damage scenarios. An example of structural damage is the sagging and hogging phenomena. Here, the contact between the building and the soil base is changed in response to surface wave propagation. Edwards et al. (1960) concluded that the main cause of this type of damage is due to the failure of the soil under these structures. Dowding (1993) provides a comprehensive review of the technical issues regarding the interaction between construction-related vibrations and structures.

In 1962, a summary of three vibration studies has been published by Duvall and Fogelson throw the Bureau of Mines (USBM RI 5968). The main purpose of this report is to establish a reliable safe limits for damage resulting from blasting vibrations. Based on this study, PPV value of 2.0 in/sec was recommended as safe limits. It later became evident that the specified limits by the USBM was not applicable under various conditions and that damage was occurring at PPV values below 2 in/sec. Consequently, in 1974 another study was published by the USBM which included an investigation of an additional sets of data that had become available since 1962 mostly from large-scale coal mines. Figure

2.2 shows the results of a recent study performed by the USBM (Siskind, 1980) summarizing the effects of blasting vibrations on low-rise buildings. The type of houses included in this study ranging from old houses with plaster to modern houses with drywalls. The damage was classified into four groups, namely major, minor, threshold and no damage.

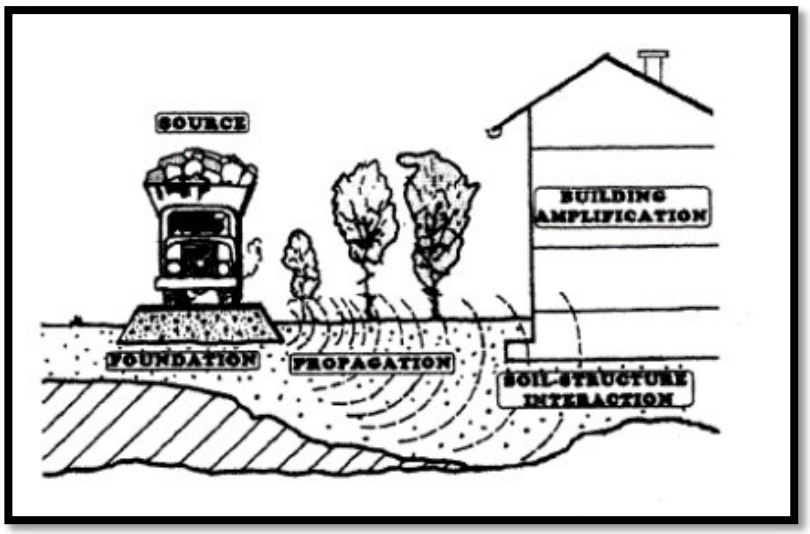

Figure 2.1.The effect of the stress waves on the adjacent buildings (Massarsch, 1993).

Measurements of vibrations included the damage resulted from ~200. The results show that different types of damage (minor, major and threshold damage) are sensitive to the ranges of PPV and dominant frequency. In a simplified version of what happens at a rock quarry during blasting, first a source is donated in a blast hole, then a chemical reaction produces a high pressure, high temperature gas. The gas pressure (detonation pressure) crushes the rock adjacent to the blast hole. The detonation pressure dissipates rapidly. The

second stage, which immediately follows, involves shock and stress wave propagation. During and after stress wave propagation, high pressure, high temperature gases are forced into radial cracks and any discontinuity such as a fracture or joint. The explosive energy takes the path of least resistance. No further fracturing occurs once the blasted rock is disjointed from the bedrock, because the gas pressure escapes. This entire process occurs within a few milliseconds after detonation of the source (Silva-Castro, 2012). As a result of the detonation pressure blasted rock fragments are pushed away from the intact bedrock (unbroken portion) which causes the bedrock to vibrate. When the vibration is transmitted through the ground, an elastic wave propagates. The propagation velocity is the speed at which the vibrations travel. As vibrations propagate away from the energy source the vibration amplitude is reduced.

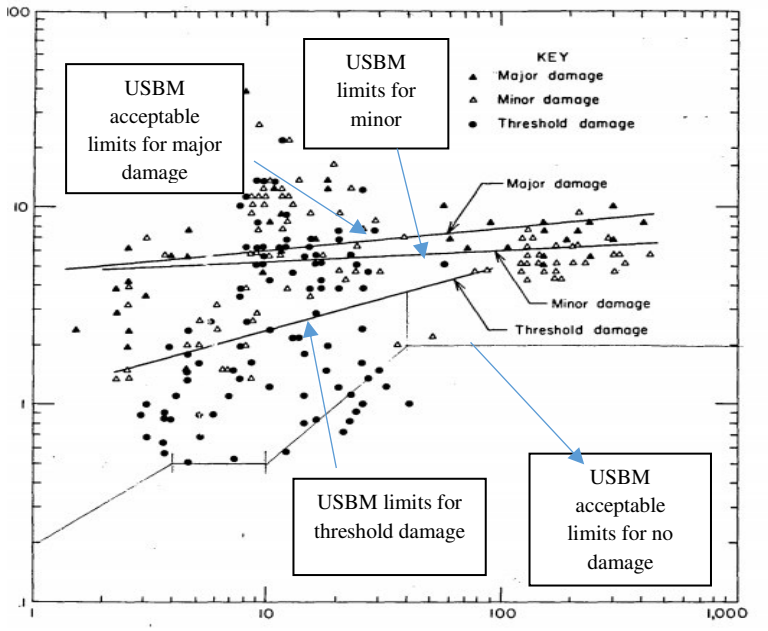

Figure 2.2. Results of studies performed by the U.S. Bureau of Mines (USBM). (Silva-Castro, 2012)

The main factors which characterize the propagation of vibrations in the ground are: 1) wave attenuation; 2) vibration focusing; 3) resonance. These phenomena are complex and are herein discussed only in a simplified way. Vibrations are a normal aspect of the environment and are caused by many everyday events such as walking, running, traffic, hammering, door slamming, and natural seismic activity.

Elastic waves, which are generated by a vibration source, attenuate as they propagate through the subsurface. Wave attenuation is caused by two different effects: 1) enlargement of the wave front as the source-receiver distance increases (geometric damping), and 2) converting the wave energy into other forms of energy (such as heat etc.) (material damping). The attenuation of waves at the ground surface due to geometric damping can be described by the following general relationship:

$$A2/A1 = (R2/R1)^{-n} \quad \text{Eq.2.1}$$

where A1 and A2 are the vibration amplitudes at source-receiver distances R1 and R2, respectively. In order to determine the exponent (n) corresponding to wave propagation type in idealized cases theoretical models constructed utilizing half-space formulation have been used (Amick et al. 2000). Table 2.1 illustrate several commonly accepted values of the exponent (n):

Table 2.1. Typical exponent values according to each wave type (Amick et al. 2000)

Source	Wave Type	Measurement Point	n
Point on Surface	Rayleigh	Surface	0.5
Point on Surface	Body	Surface	2
Point at Depth	Body	Surface	1
Point at Depth	Body	Depth	1

Rayleigh wave propagation is the most common wave propagation type in surface (or near-surface) mining and construction operations (Dowding, 1993). As vibrations propagate through the subsurface, part of the energy is consumed by friction and cohesion. The resulting reduction of the vibration amplitude is called material damping. Although the processes of attenuation are not fully understood, it is possible to include their effects in the relationship, Equation 2.2.

$$A2/A1 = (R2/R1)^{-n} * \exp^{-\alpha (R2-R1)} \quad \text{Eq.2.2}$$

The coefficient α is called the coefficient of attenuation and includes the damping properties of the geological medium. Attenuation is due to three major causes: geometric spreading, material damping, and apparent attenuation, which is the effect of material interfaces on the vibration (Yan et al., 2013). Attenuation occurs from two complementary

standpoints: (a) the decay of vibration amplitude over time at a constant location; (b) the decay of vibration amplitude at a given time with increasing source- receiver distance. The geometric spreading of a blast-induced vibration with distance typically results in an increase in wave front size (Yan et al., 2013). The decay with time of a vibration at a specific location is recorded on a seismogram, which is the vibration trace generated by a seismograph. A seismogram will typically show an amplitude peak followed by cycles of decreasing intensity before the vibration decays to the ambient background noise level or another peak amplitude spike occurs due to another blast event.

The second definition of attenuation refers to the decay of the vibration as it propagates with increasing distance. This definition is of great interest to this study. A simple idealization of this process is shown in Figure 2.3. The idealized waveform is a single spike pulse, very close to the source location (Point A). At this point, the vibration is transmitted directly through the ground. As the pulse propagates away from the source, the pulse shape distorts becoming a sinusoidal-shaped elastic vibration (Point B). By the time the vibration reaches Point B, the wave train has a longer duration and is a combination of direct transmission plus arrivals that have been affected by reflection, and refraction with geological heterogeneities.

Apparent attenuation can be defund as the effect of reflection and refraction that occurred when the wave intersect with fractures and discontinuities and other changes in lithology. This result in an attenuation of the amplitude and shape distortion of the wave train to varying degrees. Figure 2.3 is oversimplified; however, it serves to illustrate how a blast vibration generally attenuates as it propagates away from the source (Castro, 2012).

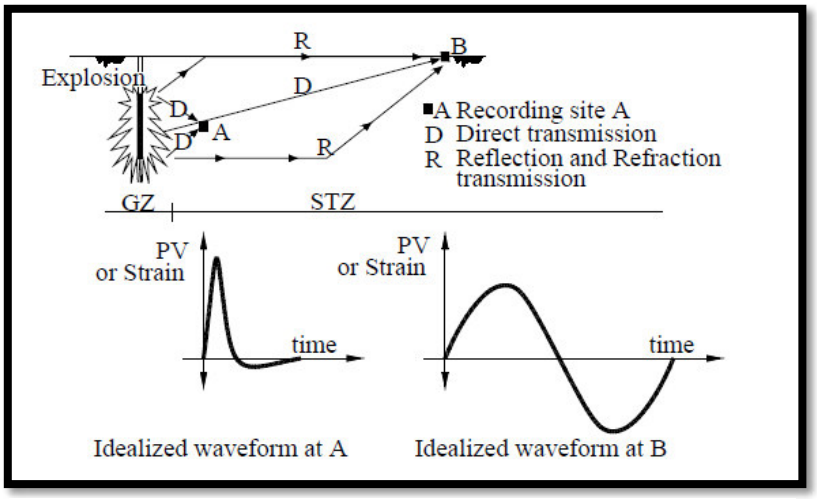

Figure 2.3: Ideal waveform due to quarry blasting (Castro, 2012)

Generally, in order to fit equation (2.2) to observed vibration data, the investigators usually follow two main approaches. The first approach is to fit the data by neglecting damping attenuation and use the exponent (geometric attenuation) as the fitting parameter. The second approach assumes that the wave propagation is dominated by Rayleigh type and the material damping parameter is used for fitting. Summary of published values of (n) from various studies according to soil types, is illustrated in Table 2.2. In this table the material damping parameter have been assumed to be equal zero. Table 2.3 summarizes a range of values of the attenuation coefficients (material damping) according to each soil types assuming a Raleigh wave propagation.

Table 2.2: Published exponent values (Geometric Attenuation) from several publications. (Amick et al. 2000).

Investigator	Soil Type	Geometric Attenuation
Wiss(1967)	Sand	1.0
Brenner & Chittikuladilok	Cays	1.5
	Surface sands	1.5
	Sand fill over soft clays	0.8-1
Attewell&Farmer	Various soils	1
Nicholls,Johnson &Duvall	Firm soils and rock	1.4-1.7
Martin	clay	1.4
	Silt	0.8
Amick&ungear	Ckay	1.5

Table 2.3: Published attenuation coefficients (material damping) from several authors.
(Amick et al. 2013)

Author	Soil type	Attenuation Coefficient
Forssblad	Silty gravelly sand	0.13
Woods	Silty fine sand	0.26
Barkan	Saturated fine grain sand in frozen state	0.06
	Clayey sand	0.04
	Marly chalk	0.1
Clough and Chameau	Sand fill over Bay Mud	0.05-0.2

The propagation of body waves and surface waves in the ground is strongly influenced by geological layering and the location of the ground water table. Reflection and refraction of body waves occur at subsurface changes of acoustic impedance. These effects are well-studied in exploration seismology but rarely taken into consideration in quarry blasting studies. Bodare (1981) pointed out the importance of refracted wave focusing which can be caused by a gradual increase of wave propagation velocity with depth. The focusing effect occurs at the ground surface at some distance from the source,

where vibrations due to direct surface wave propagation are superimposed by vibrations associated with the emergence of refracted body waves.

Different types of waves produced from controlled sources and their propagation through the ground have been discussed by Mavco (2009) and Dowding (1996). The main types of waves generated by controlled sources are longitudinal (compressive or P), shear (transverse or S) (both propagate through the body of soil or rock and hence are called body waves) and Rayleigh waves (these propagate along the surface and hence are called surface waves) (Figure 2.4), Ambraseys (1968). The body waves dominate the seismogram at close proximity to the blast while Rayleigh waves become of greatest importance at large propagation distances. Rayleigh particle motion is similar to that of fluid packets produced by dropping a stone into water. As the water wave passes, the motion of a floating cork is described by a prograde circular path whereas in rock a particle will follow a retrograde elliptical path with ratio of horizontal to vertical displacements equal to 0.7(Poggi, 2010). Among these three principal types of propagation longitudinal waves travel at the highest velocity while Rayleigh waves are characterized by slower velocities than S and P waves.

It is known that the properties of the ground stress wave from quarry blasting are different from those of seismic waves used to study earthquakes. Ground stress waves from quarry blasting usually contain relatively high-frequency energy distributed over a broad frequency band. Because the distances concerned are around 100m or so, the duration is much shorter and amplitudes are much higher than those of earthquake-generated seismic waves, for which the distances concerned are around 10-100km.

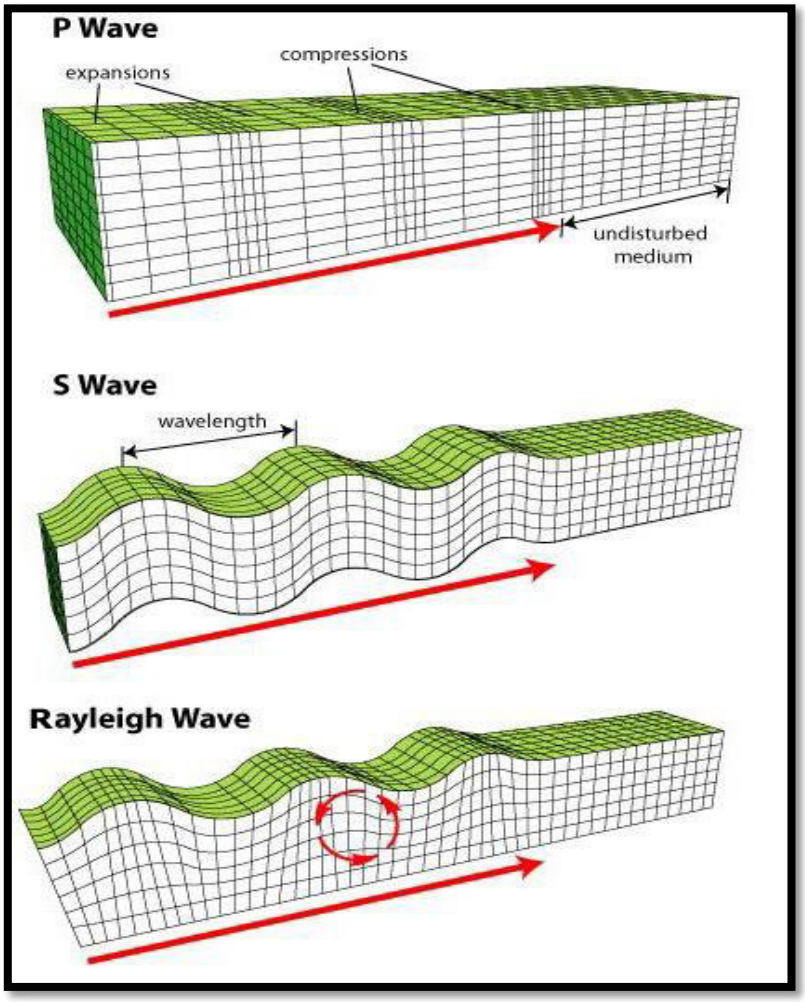

Figure 2.4: Three types of seismic wave propagation. (Ben-Menahem, 2012)

A material is called anisotropic when vector measurement of a rock property change with direction. Anisotropy causes major spatial variations in blast-induced ground motions. The dependence of seismic velocity on direction or upon angle is named as Seismic Anisotropy. Based on the axis of symmetry two main types of anisotropy have been determined, namely vertical transverse isotropy (TIV) and horizontal transverse isotropy (TIH). TIV is characterized by a vertical symmetry axis which is associated with geological layering. In case of TIH, a horizontal axis of symmetry is used to represent such type of anisotropy, which is usually useful in fractures and cracks modeling (Ruger, 1997). TIH is the type of anisotropy that is hypnotized to dominant the study.

Fault zones are usually characterized by low propagation velocity caused by a combination of clay-rich sediments, fluid concentrations and cracks (Sibson, 1977; Li and Leary, 1990). Recent studies by Li et al., 1996 have showed that fault zone trapped waves are sensitive to various possible fault structures. FZTW are produced from constructive interference of multiple wave reflections at the boundary between the high velocity intact rock and the low-velocity fault zone (Li and Vidale, 1996). They used Finite-difference simulations to demonstrate the signature of several types of complexity on seismic measured parameters (Propagation velocity and amplitudes). This study concluded that location of sources, fault zone width and kink degree have affected the seismic velocities and amplitudes. The sources that is located either in the center or near the edge of the fault zone proved to give large guided waves amplitudes (Figure 2.5). Meanwhile the sources that are positioned outside the fault zone at a large distances produced almost no signal or very small amplitudes (Figure 2.6). It also has been illustrated that late arrivals seismic

signals has been resulted in case of the large kinks angles as the wave travel a longer paths (Figure). These studies demonstrate also that the spatial variation of ground motion has a pronounced influence on site responses. This findings are useful to the explanation of amplitude and velocity variations in the study area.

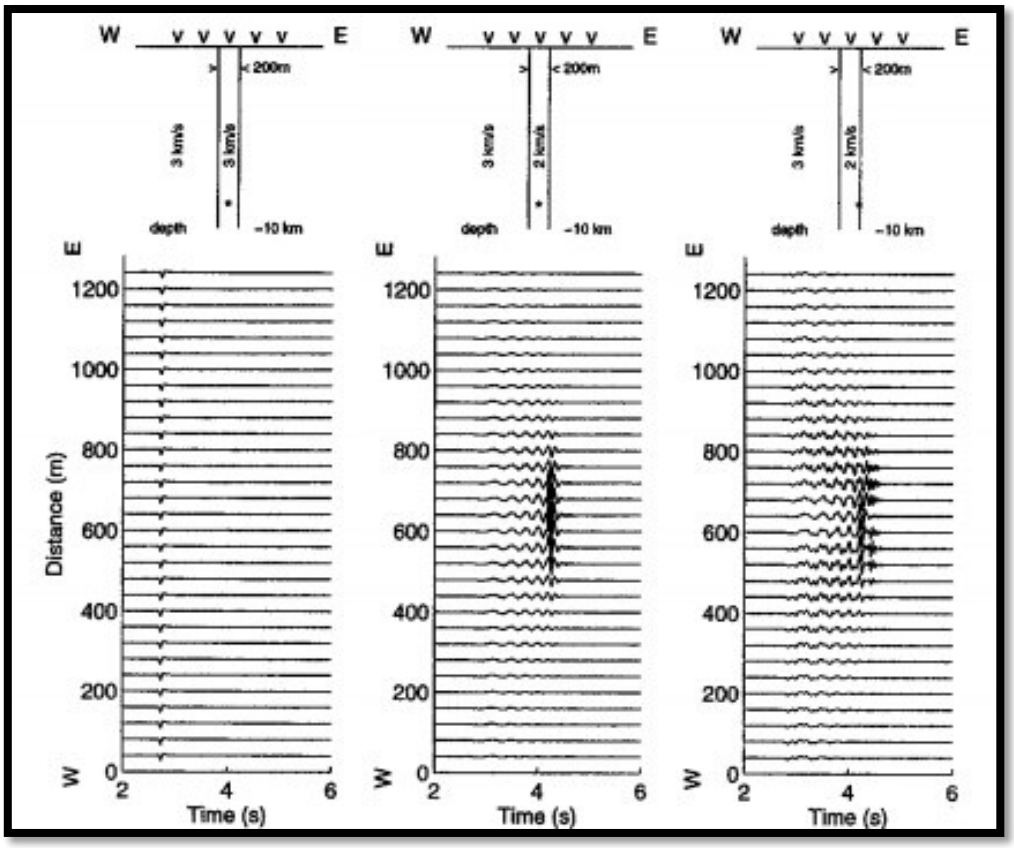

Figure 2.5: Three plots show the arrival times and amplitudes of seismic events resulted from numerical simulation (Li and Vidale, 1996). The source locations are located on or near the edge of the fault zone. Large amplitudes produced from sources near the edge.

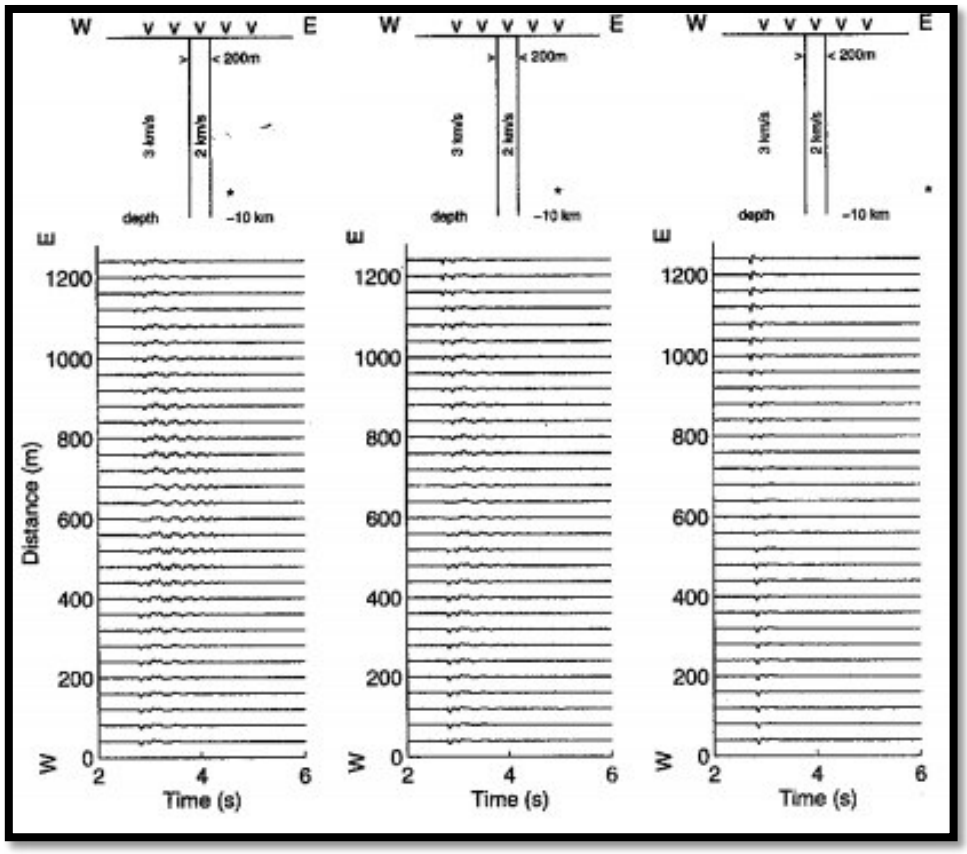

Figure 2.6 Three plots show the arrival times and amplitudes of seismic events resulted from numerical simulation (Li and Vidale, 1996). The source locations are located outside the fault zone. Very small amplitudes produced.

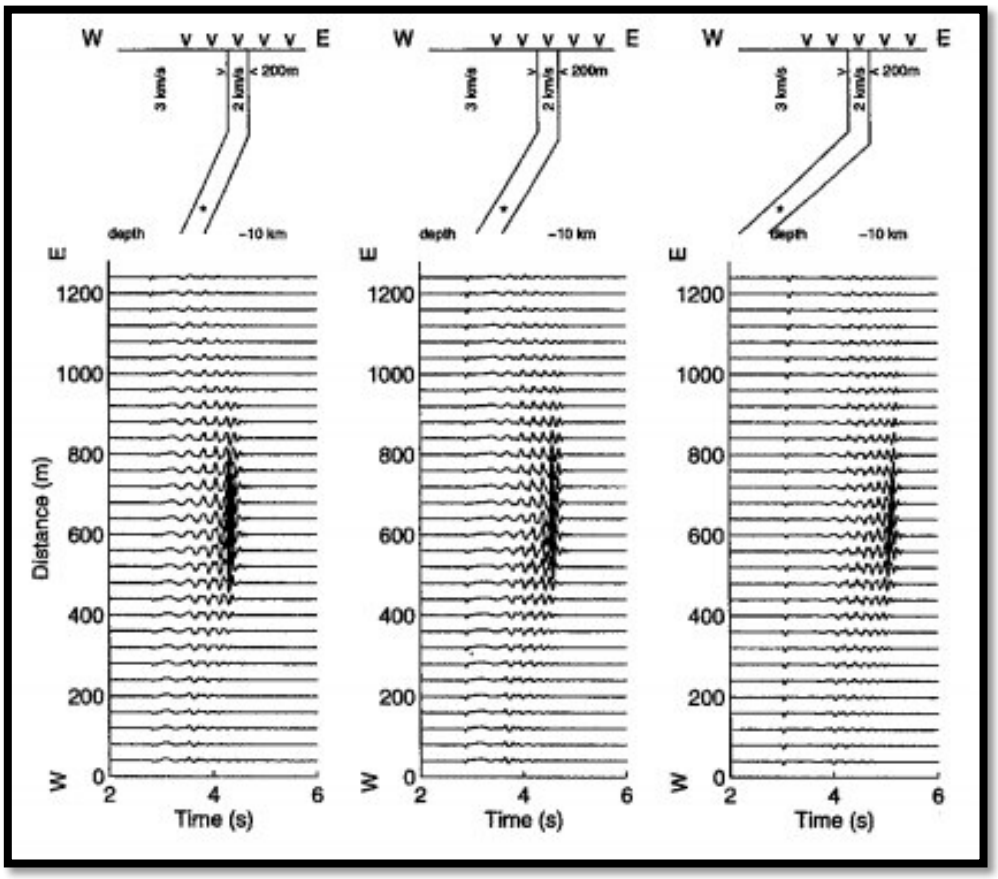

Figure 2.7 Three plots show the arrival times and amplitudes of seismic events resulted from numerical simulation (Li and Vidale, 1996). The source locations are located at the same place within the fault zone. The fault zone has different kink angles. Longer arrival times caused by larger kinks.

The available empirical attenuation relations in the literature, however, do not take account of the effect of rock mass discontinuities on stress wave propagation. Rock mass discontinuities might not appreciably affect the propagation of low frequency waves if the propagating wavelength is much greater than the characteristic separation distance of discontinuities. The discontinuities however, can attenuate near-source stress

waves because of the shorter wavelengths of such waves.

Much effort has been made to understand the propagation of stress in cracked and imperfectly elastic rocks. For example, Popp and Kern (1994) inferred crack density based on measurements of P-wave velocities in a low- porosity medium. They also found a relation between Poisson's ratio and the presence of intercrystalline fluids as applied pressure increased. Case (1980) investigated the effect of macrofractures on elastic moduli such as Young's modulus and Poisson's ratio. Zisman (1933) suggested that the increase in elastic moduli could be due to compression which aids in closing cracks in rocks. The effects of microcracks on elastic moduli has also been studied by Cleveland and Bradt (1978). In most of these studies Young's modulus was found to decrease by 10 or 20% from its value for the equivalent non-microcracked material. A number of theories have been developed to relate the average microcrack radius and density to variations in elastic moduli. Hao et al. (2001) constructed blasting experiments to study the effect of rock joints at different azimuths. It was found that seismic waves attenuate more rapidly if the travel path is perpendicular to the joints. Kaneko et al. (2008) suggested that variations in rock physical properties caused by fractures have a significant effect on elastic wave attenuation. This was also shown by Crampin (1978), who determined the anisotropy by discontinuities in the rocks. King (1986) found higher attenuation for seismic waves propagating in a direction perpendicular to joints.

In general two main approaches have been used in the studies to investigate the effect of rock joint on wave propagation. One is to examine the effects of a single joint and the other is to investigate the comprehensive effect of a number of joints using

equivalent material properties. The suitability of these two approaches depends on the spacing of joints in comparison with the wave length. The first approach is usually adopted if a single joint characterized by a large size is to be modelled, whereas the second approach is used when fractures are closely spaced compared with the seismic wave length.

CHAPTER III

VIBRATION STANDARDS AND REGULATIONS

The peak particle velocity (PPV) is defined as the maximum instantaneous particle velocity recorded on a seismogram. Resultant PPV is the vector sum of the measured PPV in the three directions (longitudinal, horizontal, and vertical) at the same measuring point. PPV unit is either inches per second (in/s) or millimeters per second (mm/s). It has been widely adopted as the best diagnostic of risk level for damage from vibrations to nearby structures. The frequency spectrum is also considered an important quantity, in addition to PPV, to describe the vibration response of structures.

Many studies have been made to associate the vibration parameters measured on seismogram such as displacement, velocity and acceleration with observed structural damage and human annoyance, (e.g. Siskind et al., 1980, Nichols et al., 1971). The best correlation was found between resulting damage and peak particle velocity (PPV). Wiss (1978) suggested a limit of 100 mm/s should be used for commercial structures. The importance of the vibration frequency for damage assessment on structures was highlighted in a number of publications, for example, Medearis (1977), Siskind et al. (1980), Dowding (1996). The U.S. Bureau of Mines have made an intensive study on the relations between vibrations/displacement and velocity and structural damage.

Various rules and regulations have been developed in several countries based on the dominant operating conditions and the types of affected structures. Consequently the allowable levels of blast vibrations differs from country to country as well as from state to state within the United States (Wiss, 1978). Most of the states have multiple damage

criteria .The main purpose of the guidelines is to guarantee that all the vibration levels are within safe limits. The office of Surface Mining (OSM) regulations and the United States Bureau of Mines (USBM) Regulations (Figures 3.1 and 3.2) have long been used as the damage criteria inside the US. These vibration limits have been determined based on many years of field investigations. The weakest building materials are usually the most critical to be protected by these limits. For instance, plaster is considered by USBM to be a fragile material that easily breaks in response to the vibrations. Threshold damage is defined as the lengthening of preexisting hairline cracks in plaster, according to the USBM. Recently, most authorities have considered 50 (mm/s) (2.0 in/s) to be an acceptable safe limits for quarry blasting. Several authors such as Crawford and Ward (1965) considered these values to be very conservative. They concluded that most of the houses may withstand higher PPV values of ~137 (mm/s) to 508 (mm/s) before experiencing minor damage depending on the structure type.

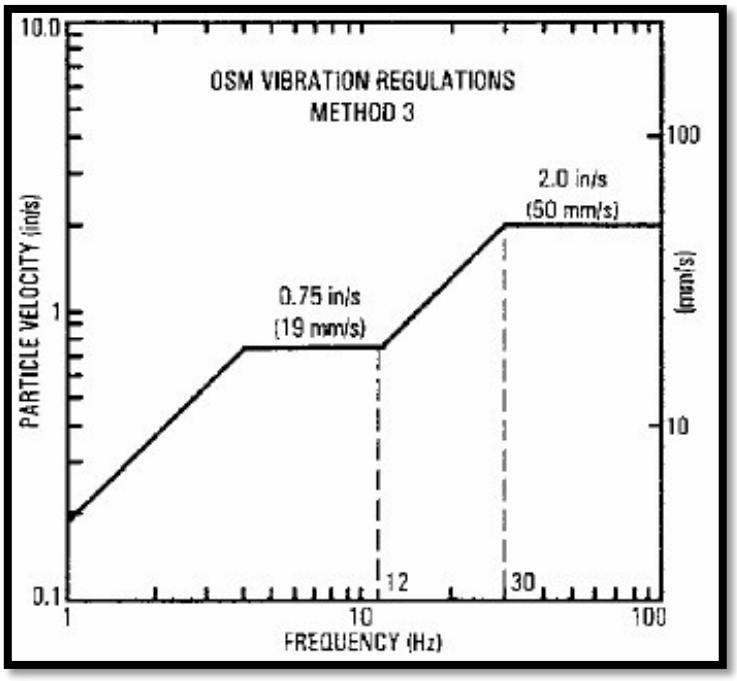

Figure 3.1: Acceptable limits according to OSM regulations.
(Siskind, 1980)

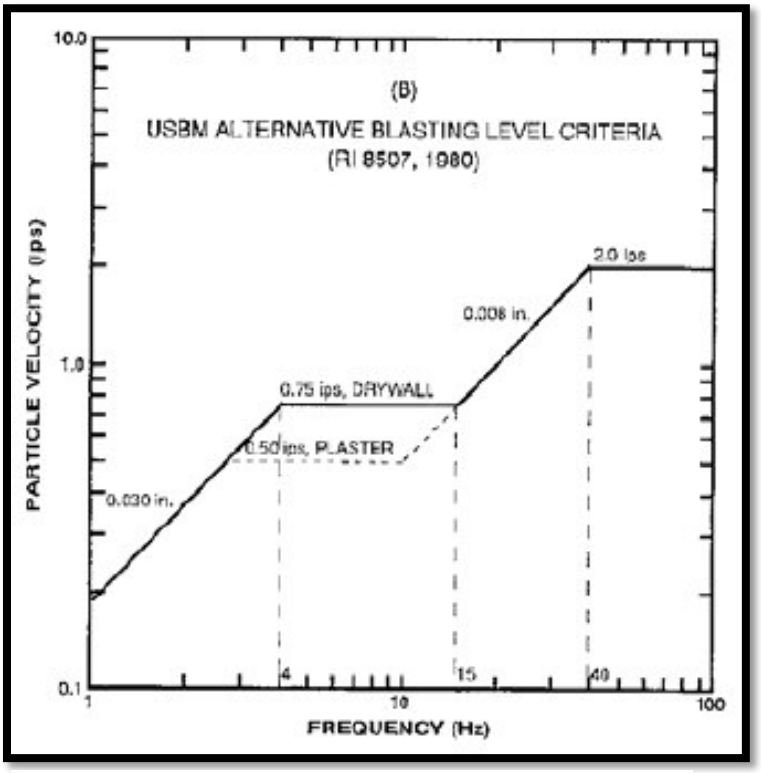

Figure 3.2: Allowable vibration limits according to the USBM regulations. (Siskind, 1980)

Based on the Bureau of Mines report RI8507, the safe limits of vibrations can be expressed as a relationship between PPV and frequency. As can be seen from figure 4.2, the limits are very conservative at low frequency. At higher frequencies the recommend limits for the PPV increase. Individual components in the house are more susceptible to vibrations at higher frequencies. This type of vibration is called the 'midwall response'. Meanwhile, if the stress wave contains a lower frequency vibrations, the entire structure may be affected. Due to the fact that most buildings have a low natural frequency,

such movement can be amplified. As a result, houses in the close proximity to the quarry blasting will experience a greater shear stress and higher potential for damage. In addition, low frequency vibrations may create an impression to people that the effects of the ground vibrations are worse than in actuality.

Vibration regulations have provided a feasible tool to prevent damage to occur to any type of building, irrespective of its age and condition. This therefore created more stringent limitations than required. The Bureau of Mines report of vibration guidelines recommends 50 mm/s for frequencies above 40 Hz. For vibration with lower frequency component, the limits become more conservative with a range of 12 to 19 mm/s. To reduce the probability of causing damage from blasting vibrations, blasts are usually design to generate high frequencies. Table 3.1 summarizes the general recommendation of the damage criteria and the allowable limits of PPV specified by Bureau of Mines and OSM (Oriard , 1999).

Table 3.1: Summary of general recommendation by Bureau of Mines and OSM for the damage criteria and the allowable limits of PPV (Oriard, 1999).

12.7 mm/s (0.5in/s)	Bureau of Mines recommended guideline for plaster-on-lath construction near surface mines (long term, large scale, low frequency vibrations) (RI 8507)
19.1mm/s (0.75in/s)	Bureau of Mines recommended guideline for sheetrock construction near surface mines (RI 8507)
25.4 mm/s (1.0in/s)	OSM regulatory limits for residences near surface mine operations at distances 92-1524 meters (301-5000 feet)
50.8 mm/s (2.0 in/s)	Widely accepted limit for residences near construction and quarry blasting (BuMin 656, RI 8507)
137mm/s (5.4 in/s)	Minor damage to the average house subjected to quarry blasting vibrations (BuMin 656)
229 mm/s (9 in/s)	About 90% probability of minor damage from construction or quarry blasting. Structural damage to some houses depending on vibration source and character of the vibrations.
501 mm/s (20 in/s)	For close-in construction blasting, minor damage to nearly all houses and structural damages to some. For low-frequencies, major damage to most houses.

In Cases where the measurements in the field do not include the frequency of the vibrations, Table 3.2 can be used instead in order to specify a safe blasting design. It should be mentioned that these values are based on the more conservative considerations for building damage. In addition, Table 3.3 shows a summary of other criteria that are followed in different countries to regulate allowable limits.

Table 3.2: Ground vibration limits specified by OSM.

Disatnce	Scaled distance	PPV
0 to 300	50	1.25(ips) 31.75(mm/s)
301 to 5000	55	1.00(ips) 25.4(mm/s)
Over 5000	65	0.75(ips) 19.05(mm/s)

Table 3.3 Summary of the damage criteria for each country. (Zeigler, 2013)

Australia (2187.2),	France (GFEE),
New Zealand (NZS/ISO 2631-2, 4403),	Slovenia (DIN 4150),
Brazil (NBR 9655),	Germany (DIN 4150) and
Britain (British Standard 7385, BS 6472),	pain (UNE 22381
ISO (International Standards Organization)	France (GFEE),
ANSI (American National Standards Institute)	India (IBS/ISO 4866, DGMS A and B)
Czech Republic (ČSN 73 0040),	ANSI S2.47 (a U.S. counterpart of ISO 4866)

CHAPTER IV

MODELLING PROCEDURES

4.1 Available Data

At the request of the Garden Ridge Quarry commission, a number of seismic monitoring stations have been installed by Vibra-Tech Company at various locations in the neighborhood to the west of the quarry. The data enable the commission to monitor the quarry blasts and analyze the resulting inconvenience and potential hazards on the residents' health, buildings, and surrounding infrastructure. Around 600 blast events have been recorded between 2012-2015 at different locations adjacent to the quarry. Ground-motion velocities were measured in three orthogonal directions (longitudinal, vertical, and transverse). Peak particle velocity has been calculated from each seismic trace as described by Dowding (1996). In addition, the associated dominant frequencies for each recorded event were calculated and attached to the data. A fast Fourier transform method has been applied by the Vibra-Tech Company in order to extract these frequencies. Figure 4.1 shows a typical Vibra-Tech event report that is used to present the collected information from each blast. These data are publicly available. Table 4.1 presents a statistical summary of all of the measured data used in this thesis. Moreover, a blast impact questionnaire has been created by the quarry commission in order to collect important information about the distribution of complaints caused by the blasting. Around 200 complaint reports have been received both electronically and in paper-based form from residents. In the report, the resident is asked to describe his/her concerns and feelings regarding the felt blast. A rating scale of annoyance from 1-5 is included on the form. The

rating classifies the human response into 5 different categories according to the perceived impact of the blast Table 4.2 presents the categories, while Figure 4.2 shows an example of an impact report that was filled out by a resident, whose personal information is kept confidential.

Table 4.1: The basic descriptive statistics of the measured PPV, Frequencies, Q_{max}, and Distances. All data from 2012-2015.

Variable	Mean	Std. Dev	Min	Median	Max	Range	Mode
F (Hz)	15.20	8.30	3.20	13.00	140.00	136.80	11.00
PPV (in /sec)	0.09	0.07	0.02	0.07	0.42	0.40	0.02
Q_{max} (lbs)	737.50	301.10	80.00	806.00	1902.00	1822.00	858.00
D (ft.)	4239.80	1854.70	1056.00	4013.00	11458.00	10402.00	3907.00

Table 4.2: The rating scale that has been provided to the residents to classify the blasting impact.

Severity Rating (1 minor- 5 major)	Description
1	Noticeable, but barely
2	A nuisance and definitely observable
3	Wake a sleeping person; alarming ; Windows rattle
4	Building movement ; pictures fall ; dishes rattle
5	Really gets your attention ; Windows cracked

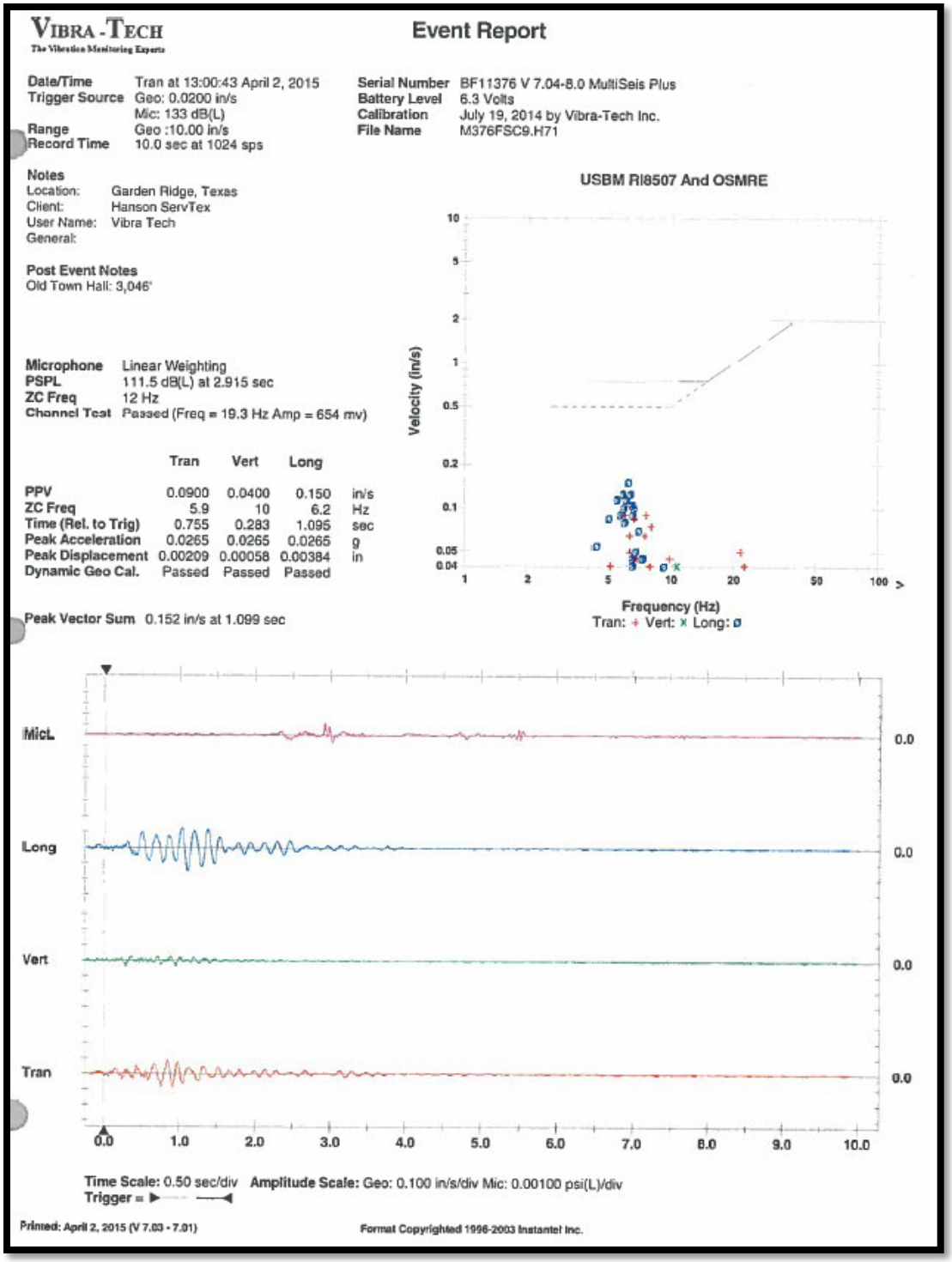

Figure 4.1: The typical Vibra-Tech event report that is used to present the measured data from each blast (Vibra-Tech Company Reports, 2015).

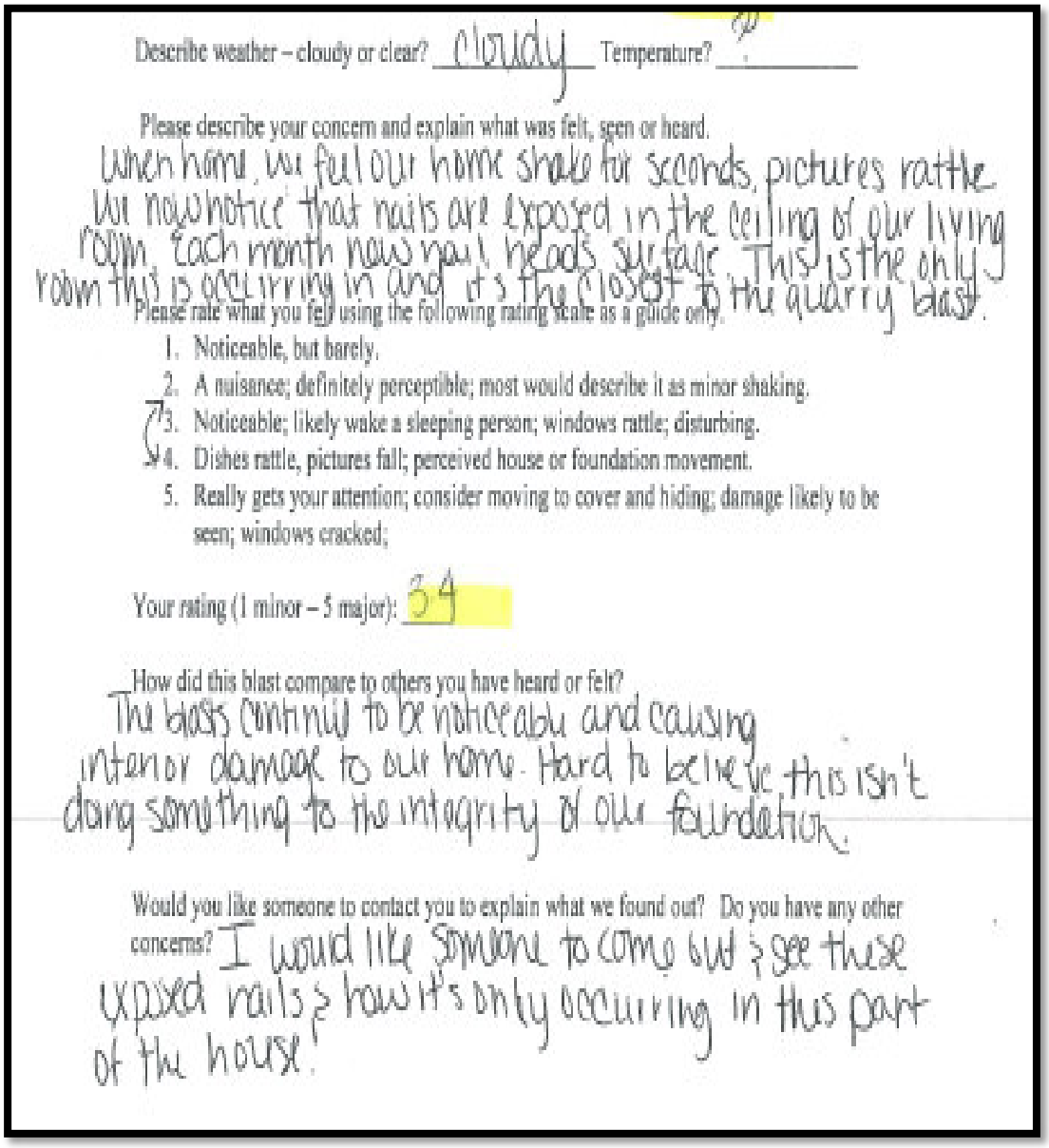

Describe weather – cloudy or clear? Cloudy Temperature? 60

Please describe your concern and explain what was felt, seen or heard.

When home, we feel our home shake for seconds, pictures rattle. We now notice that nails are exposed in the ceiling of our living room. Each month new nail heads surface. This is the only room this is occurring in and it's the closest to the quarry blast.

Please rate what you felt using the following rating scale as a guide only.

1. Noticeable, but barely.
2. A nuisance; definitely perceptible; most would describe it as minor shaking.
3. Noticeable; likely wake a sleeping person; windows rattle; disturbing.
4. Dishes rattle, pictures fall; perceived house or foundation movement.
5. Really gets your attention; consider moving to cover and hiding; damage likely to be seen; windows cracked;

Your rating (1 minor – 5 major): 3-4

How did this blast compare to others you have heard or felt?

The blasts continue to be noticeable and causing interior damage to our home. Hard to believe this isn't doing something to the integrity of our foundation.

Would you like someone to contact you to explain what we found out? Do you have any other concerns? I would like someone to come out & see these exposed nails & how it's only occurring in this part of the house.

Figure 4.2: An example of the impact report that uses the city-provided questionnaire

Figure 4.3 shows histograms of the severity of complaints in the study area. The data indicate that the complaint severity divides into a distinctive pattern of approximately six zones. Consequently, based on the specific locations of the receivers and according to

the histograms of the complaint severity, the study area is divided conceptually into six zones of different blast effect. The zones indicating the characteristic frequency and severity of these complaints are illustrated in Figure 4.4. Residents living near the OLD, ESTEVE, and WARDEN receiver locations report the highest frequency of severe complaints. At the HOLLY location, the complaints were relatively frequent but of a lesser severity compared to the above-mentioned locations. Lower numbers of complaints with severity ranging from 1 to 3 were recorded from residents living near the TAVERS receiver. Complaint severity with a broad range from 1 to 5 was found to occur toward the south of the study area, specifically at the Mills and Schneider receiver locations. Table 4.3 shows the total number of complaints that used to construct each histogram.

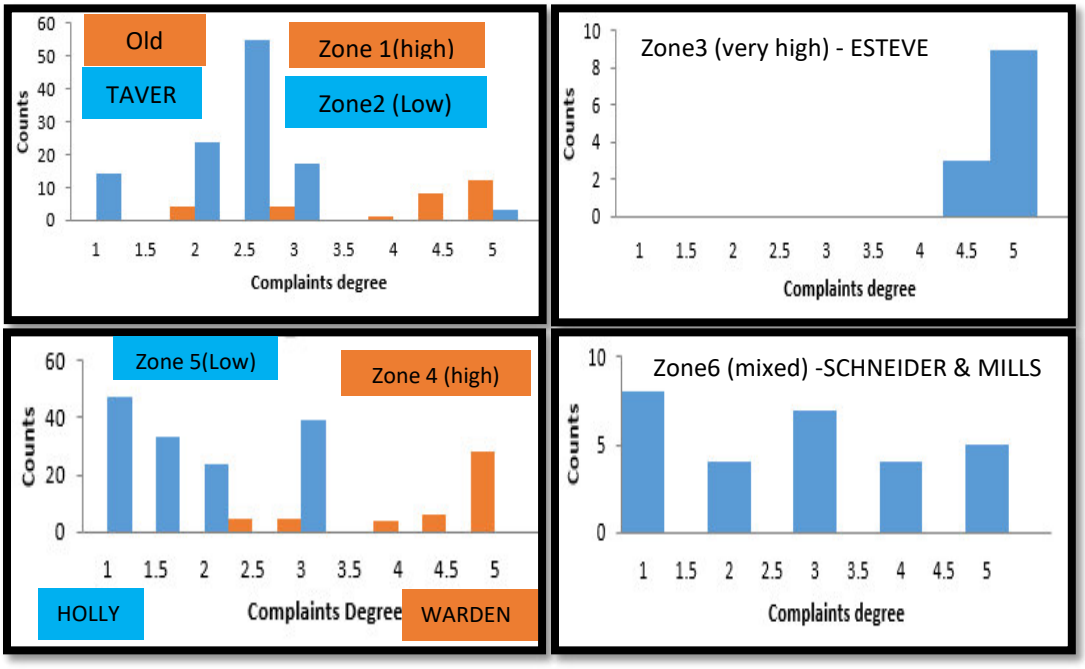

Figure 4.3: Histograms of the complaints severity according to each zone,

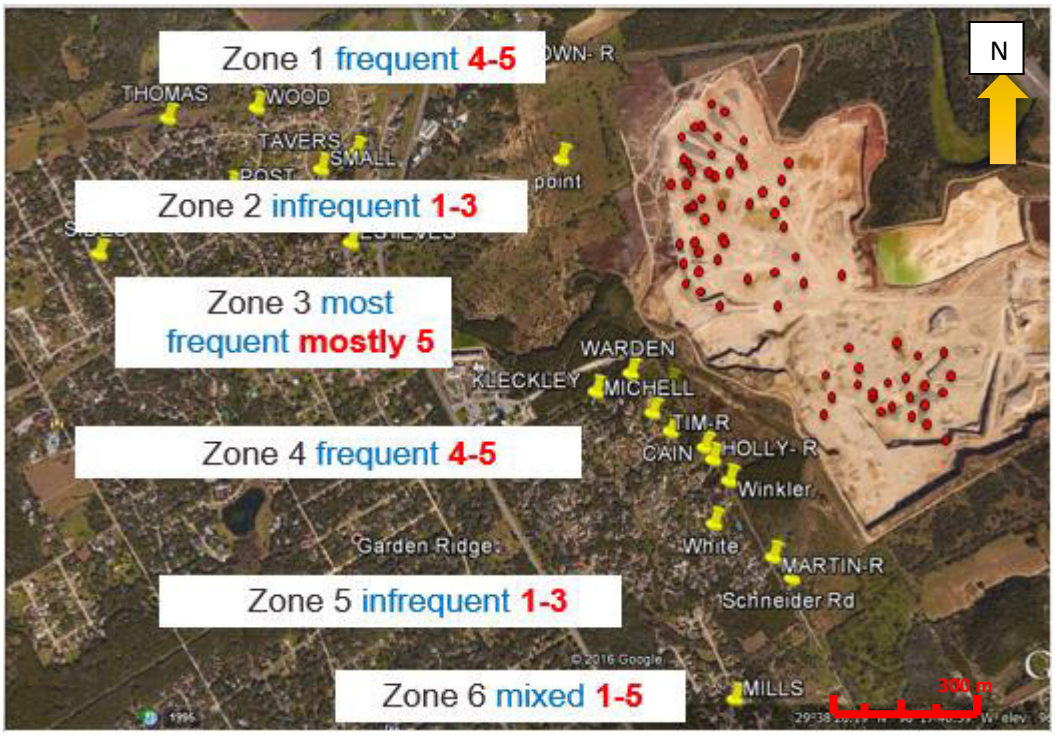

Figure 4.4: Approximate distribution of the complaint severity and its frequency overlain a satellite photo of the study area

Table 4.3: Total number of complaints according to each zone.

Zone of interest	Total number of complaint	Main receiver
Zone 1	60	OLD, WOOD
Zone 2	93	TAVERS, SMALL, POST
Zone 3	32	ESTEVES, MILDA
Zone 4	65	WARDEN, CAIN, WAP
Zone 5	74	HOLLY, WINKLER
Zone 6	45	SCHNEIDER, MARTIN, MILLS

Investigation of the geological location of the study site revealed that it located inside the region of the Balcones fault zone which is dominated by underground water aquifers. Edwards aquifer is one of the principle fresh water aquifers in south-central Texas. In this thesis, Edwards aquifer lies beneath the study site. Numerous geological studies were jointly performed by the U.S. Geological Survey and the Edwards Underground Water District in order to identify the hydrological characteristics of the Edwards aquifer. In this study, geologic maps and well logs were individually collected and compiled from the USGS reports, and were used in determining the general geological structure of the study area. These reports are open source and available for public use. Examples of such reports are the Water-Resource Investigation Reports 94-4117 and 93-4100 . Three maps in particular were found to be useful in this study; the regional structure map of the Balcones faults zone (George, 1952); the structural geological map of the San Antonio area (Veni, 1995); and finally the surface geological map of Comal County (Small, 1994). Using these maps, the geologic framework of the study area including the lithological distribution and fault locations were extracted. In general, the maps provide and reports comprehensive geological background information.

In addition, the thicknesses and rock properties of the formations present in the study area were estimated using 18 well logs measured at three locations within the San Antonio area. This wells were drilled and operated by the USGS in collaboration with the Texas Board of Water Engineers in order to assess the hydrological system of the Edwards aquifer. The well logs are found in the final reports of these assessments. An example of such a report is the “Geology and Ground water Resources of Comal County, Texas” by

George (1952). An example of 6 well logs extracted from such reports is shown in Figure 4.5. These logs include caliber, natural gamma ray, spontaneous potential, resistivity, neutron porosity, density and acoustic velocity measurements. Figure 4.6 shows the location of the well with regard to the study area.

Moreover, a number of laboratory tests found in literature provide more detailed information about the rock properties of the area and provide guidance about the typical values for geophysical parameters used in this study.

The information that has been compiled from the literature has been used in several different stages of the modelling process. The prior geological knowledge aided in decreasing the uncertainty and improving the nonlinear regression process that is prominently used later in this chapter.

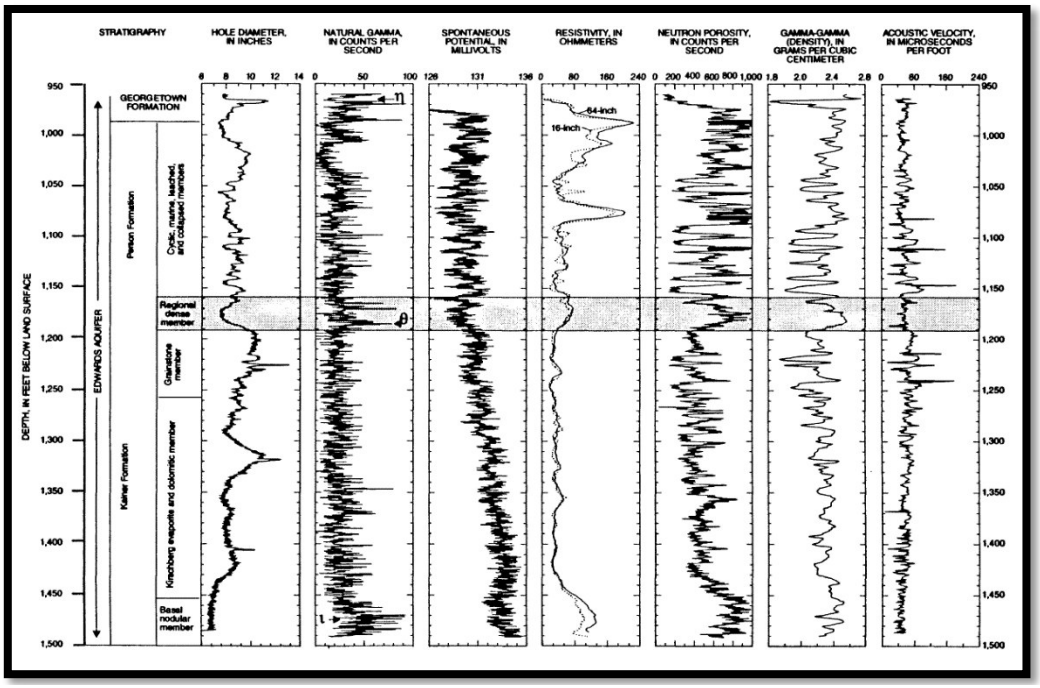

Figure 4.5: An example of 6 well logs measured from the same well in San Antonio area. (George, 1952)

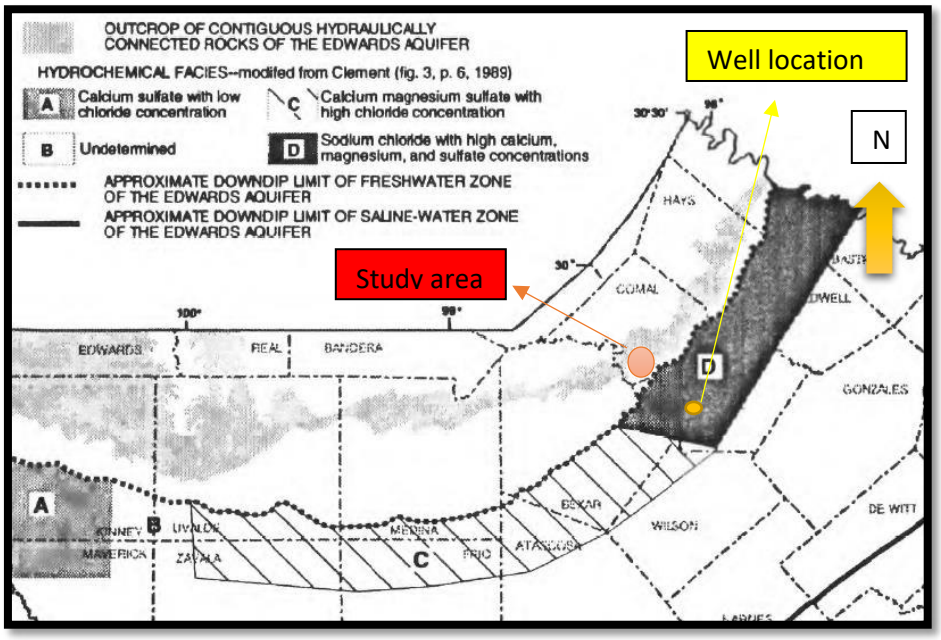

Figure 4.6: Geographic location of the well that used to measure well logs in Figure 4.5. Modified after George (1952)

4.2 Conceptual Model

Geophysicists generally base quantitative modelling on an underlying conceptual model. Conceptual models are useful in the planning and interpretation of near-surface geophysical site investigations. The development of conceptual and quantitative geologic and geophysical modelling is illustrated in Figure 4.7. The input is a geological description and the output is a geophysical response.

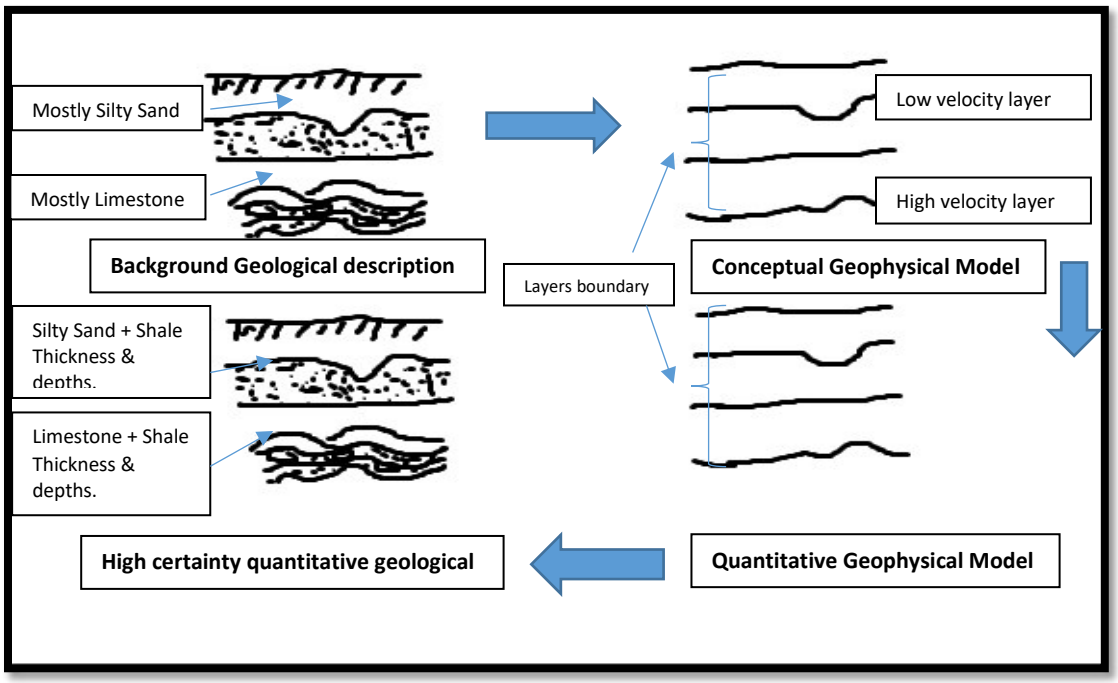

Figure 4.7: Schematic diagram shows the development of conceptual and quantitative geologic and geophysical modeling.

Building a conceptual model is an essential early stage in geophysical site investigation and it is vital for implementing quantitative modeling. The accuracy of the input data of a conceptual model is important. The process aims to achieve a consistency between the modeled responses and the observed data. In this study, a conceptual model has been constructed using the best available information from the literature and measured responses.

An accurate conceptual model is the primary step in developing relationships between the observed responses (PPV and dominant frequencies) and the geological structure. A main purpose of this study is to link these responses to the underlying geological structure. A simple framework for the conceptual model is set out in Figure 4.8. The available data that are used in building the conceptual model, can be divided into 3 categories summarized in Table 4.4

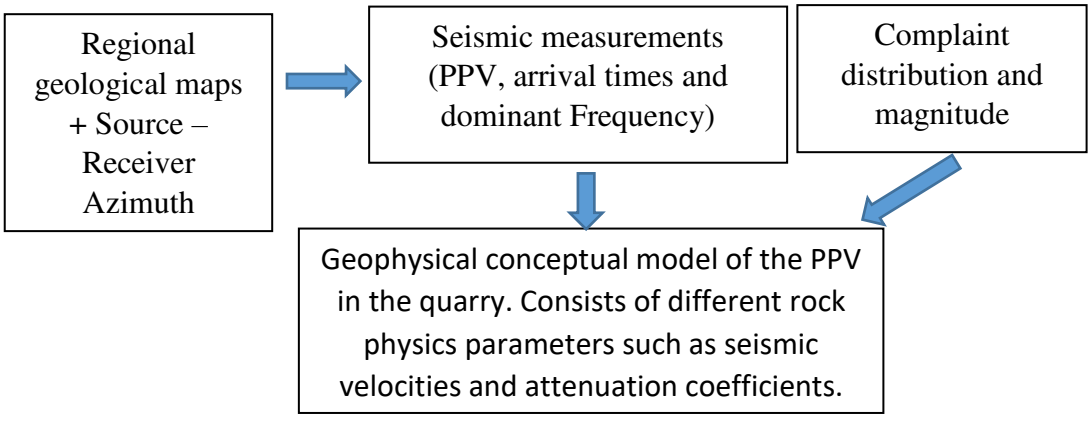

Figure 4.8: Simple framework for conceptual model building

Table 4.4: Elements of the conceptual description along with the sources and data types.

Elements of the Conceptual Model	Types of data
Conceptual Geological Model: Solid rock and fluid types.	(Literature) geological maps ; laboratory data
Conceptual Geophysical model: Elementary explanation of the effect of the geology on different geophysical responses : 1- Degree of attenuation and amplification 2- Dominant wave types (surface/ guided, and body waves)	(Previous geophysical survey results) Vibra-Tech event sheets, Aerial photos Propagation wave velocities, Satellite images, Well logs
Human responses	Blast impact reports

4.2.1 Geological Description for the Study Area

4.2.1.1 Regional Geology of Comal County

The location of the Servtex quarry lies inside the city limits of Garden Ridge city (Comal County) in south-central Texas as displayed in Figure 4.9. The regional geology includes the Southeastern Balcones Escarpment, Edwards plateau, and the northern Gulf Coastal Plain. Sedimentary rocks cover most of the county with minor outcrops of igneous rock existing as a basaltic extrusion. Metamorphic rocks in the form of schist have been observed in shallow well logging measurements. The study area lies primarily within the Balcones fault zone as shown in Figure 4.10 and comprises sedimentary rocks formed during the Cretaceous including the Person (Edwards group), Del Rio (clay), Buda (limestone), Austin group (chalk, marl, and limestone), and Pecan Gap (chalk).

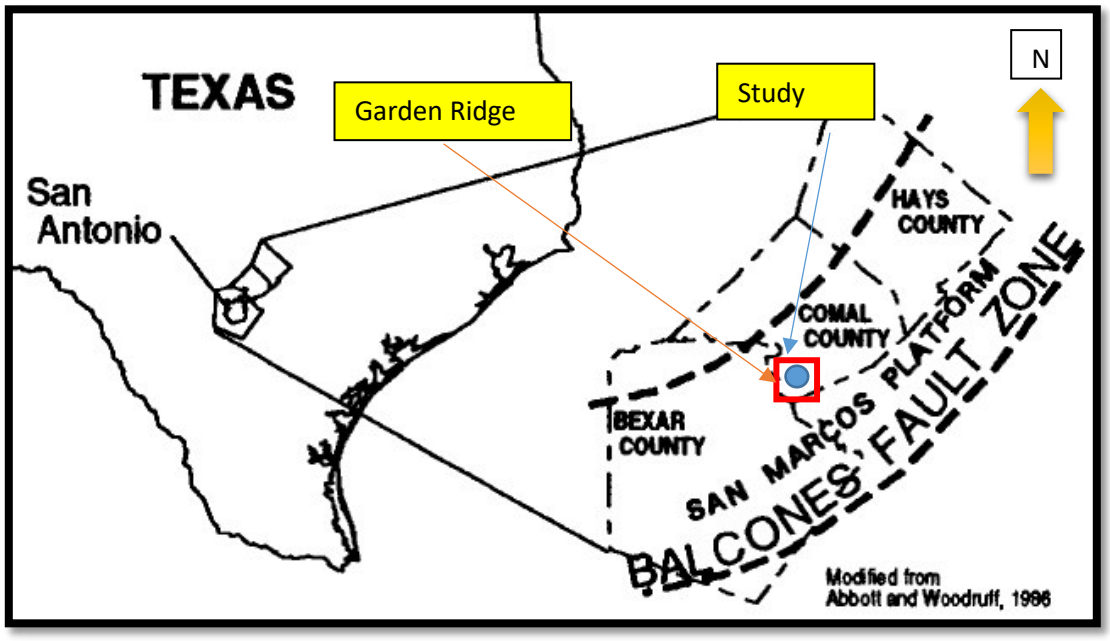

Figure 4.9: Geographic location of Comal County including the study area, with reference to the Balcones fault zone. Modified after George (1947).

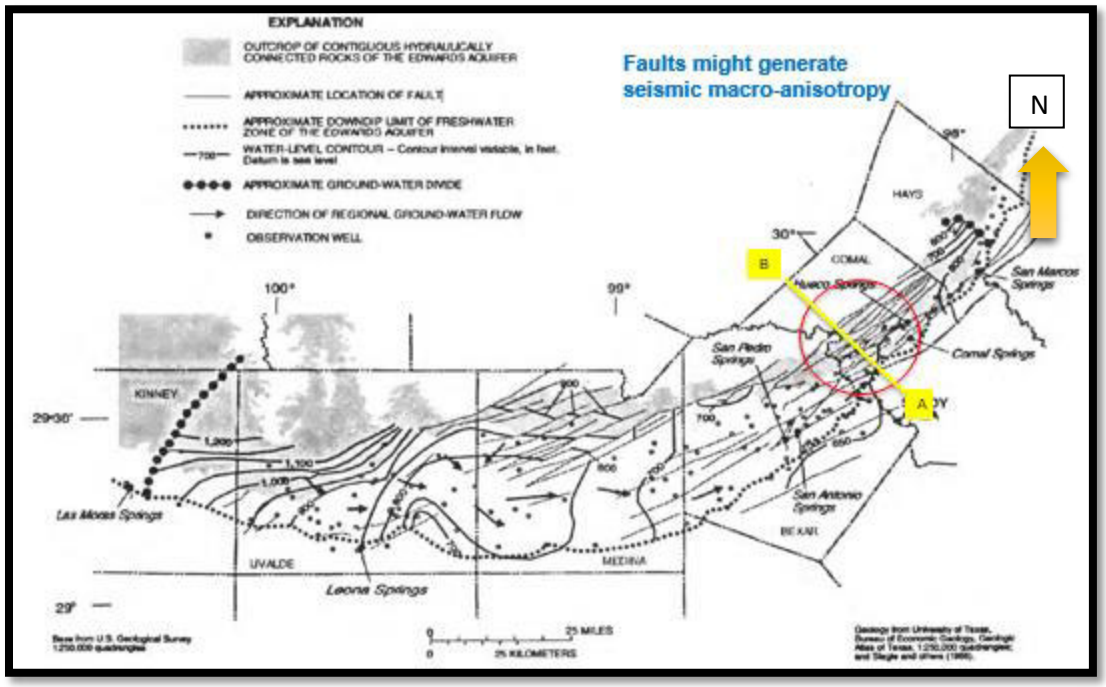

Figure 4.10: Regional geological structure of the Balcones fault zone. The yellow line indicates cross section across the study area in Comal County. (George, 1947)

4.2.1.2 Soil/Rock Characteristics and Depositional Environment

South-central Texas has three main depositional provinces including the Maverick basin, the Devils River trend, and the San Marcos platform which were formed in the Early Cretaceous period. The energy conditions, in general, were different within each province during the time of deposition. This caused a geographic variation in the depositional environments. San Marcos platform, where the study area is located, is dominated by sabkhas and tidal flats (Rose, 1972). Most of the sediments are in the form of dolomite, dolomitic limestone, mudstone, wackestones and micrites. Micrites in San Marcos platform contain burrowed mudstones and collapse breccias. Within the wackestone sediments, anhydrite appears as continuous beds and separated lenses.

Deposition at the top of the Edwards Group was interrupted by subaerial erosion and karstification due to uplifting tectonics in early cretaceous (Rose, 1972). During the Late Cretaceous, the Edwards Group was deeply buried by marine transgressive sediments. Edwards Group is located within San Marcos platform. The depositional environment of Edwards Group has been identified in many studies as shallow marine (Rose, 1972 and Abbott, 1975).Variations in the depositional conditions caused transformations in lithology and development of distinct petrophysical properties of each member of the Edwards Group (Rose, 1972 and. Abbott, 1975).

On average, the Edward Group has a thickness of 134 m in the region of Comal County and is comprised of limestone and a number of discontinuous beds (George, 1952). The Kainer and Person Formations are the building blocks of the Edwards Group. These formations are divided into seven members according to Rose (1972). Maclay and Small

(1976) modified the stratigraphy by including the Upper Georgetown Formation. Table 4.5 summarizes the lithological constituents of each formation along with a description of the petrophysical characteristics including porosity and permeability. Within Comal County, the Kainer Formation is reported to have an average thickness of 79 m. The lithology types range from mudstone to crystalline limestone. The lower most unit has a thickness of about 15m and is characterized by a massive, nodular limestone which lies conformably on the top of the lower confining unit of the Glen Rose Limestone. Drilled wells in Comal County show that the Person Formation is nearly 55 m thick and its strata range from burrowed mudstone and grainstone to crystalline limestone. Dense argillaceous mudstone composes the lowermost member of the Person Formation.

Overlying the Edwards Group is the Georgetown Formation, which was deposited on the eroded surface of the Person Formation (see Fig.4.11) in deeper water than was characteristic for the deposition of the majority of the Edwards Group (Rose, 1972). The Georgetown Formation largely consists of marly limestone. Exposures of the irregularly bedded Georgetown Formation are infrequent, and where observed, have a thickness of less than 3m.

The Upper Cretaceous Del Rio Clay, Buda Limestone, Eagle Ford Group, Austin Group, Navarro, and Taylor Groups superimpose the Georgetown Formation as shown in Figure 4.11. The Del Rio Clay (Table 4.5) is a dark blue-green to yellow-brown, variably gypsiferous clay. The Buda Limestone is a dense, unevenly nodular, light gray mudstone (Small, 1998).

Field investigations and geological maps from the study area reveal that the various members of the aforementioned formations outcrop within and near the Servtex quarry as shown in Figures 4.12 and 4.13. The existence of spatially heterogeneous geological formations is hypothesized to be one of reasons that causes a variation in the seismic radiation pattern resulting from the quarry blasts.

Table 4.5: Summary of the lithologic properties of Edwards aquifer (Small, 1994)

Hydrogeologic subdivision			Group, formation, or member			Hydro-logic function	Thickness (feet)	Lithology	Field identification
Upper Cretaceous	Upper confining units		Navarro and Taylor Groups, undivided			CU	600	Clay, chalky limestone	Gray-brown clay; marly limestone
			Austin Group			CU; rarely AQ	130 - 150	White to gray limestone	White-chalky limestone; *Gryphaea aucella*
			Eagle Ford Group			CU	30 - 50	Brown, flaggy shale and argillaceous limestone	Thin flagstones; petroliferous
			Buda Limestone			CU	40 - 50	Buff, light gray, dense mudstone	Porcelaneous limestone
			Del Rio Clay			CU	40 - 50	Blue-green to yellow-brown clay	Fossiliferous; *Ilymatogyra arietina*
Lower Cretaceous	I	Edwards aquifer	Georgetown Formation			CU	Less than 10	Gray to light tan marly limestone	Marker fossil: *Waconella wacoensis*
	II		Edwards Group	Person Formation	Cyclic and marine members, undivided	AQ	80 - 100	Mudstone to packstone; *miliolid* grainstone; chert	Light tan, massive; some *Toucasia*
	III				Leached and collapsed members, undivided	AQ	80 - 100	Crystalline limestone; mudstone to grainstone; chert; collapsed breccia	Bioturbated iron-stained beds separated by massive limestone beds; *Montastrea sp.*
	IV				Regional dense member	CU	20 - 24	Dense, argillaceous mudstone	Wispy iron-oxide stains
	V			Kainer Formation	Grainstone member	AQ	50 - 60	*Miliolid* grainstone; mudstone to wackestone; chert	White crossbedded grainstone; *Toucasia*
	VI				Kirschberg evaporite member	AQ	50 - 60	Highly altered crystalline limestone; chalky mudstone; chert	Boxwork voids, with neospar and travertine frame
	VII				Dolomitic member	AQ	110 - 130	Mudstone to grainstone; crystalline limestone; chert	Massively bedded light gray, *Toucasia* abundant

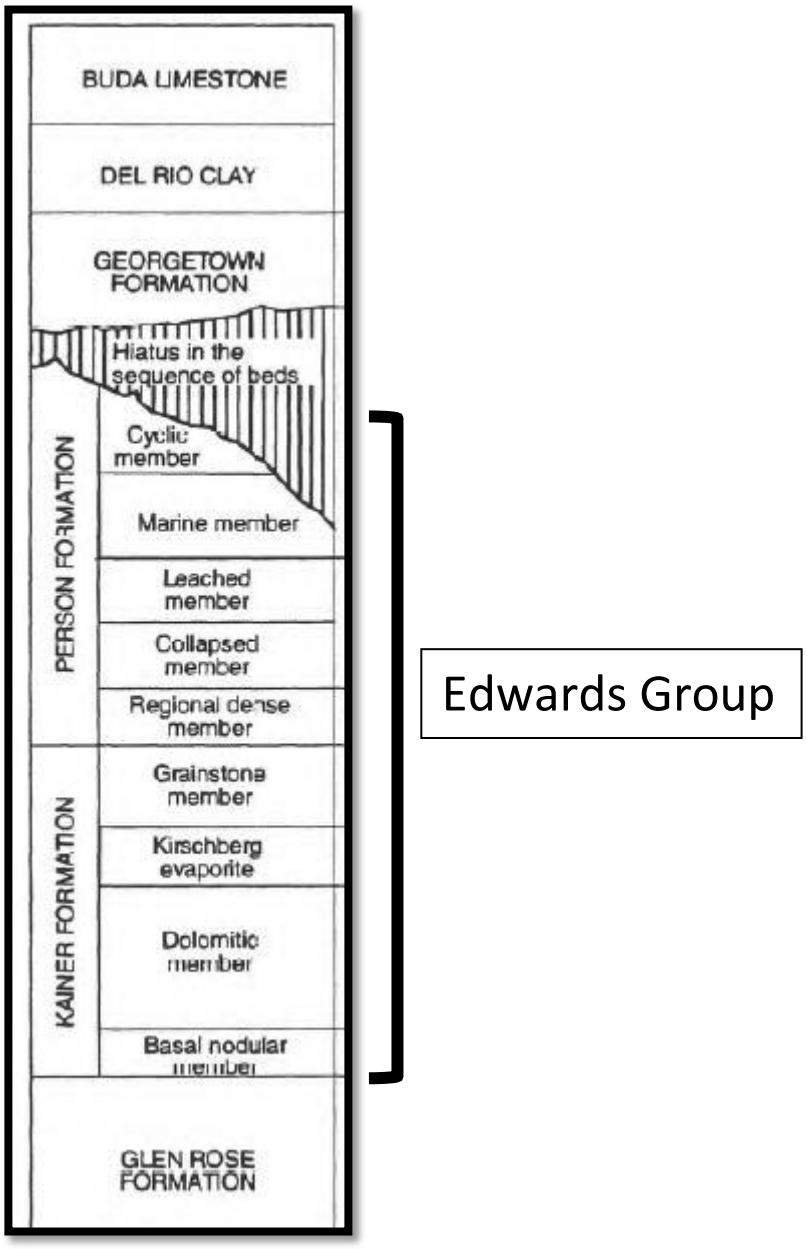

Figure 4.11: Simplified Stratigraphic column of Edwards aquifer (Small, 1994).

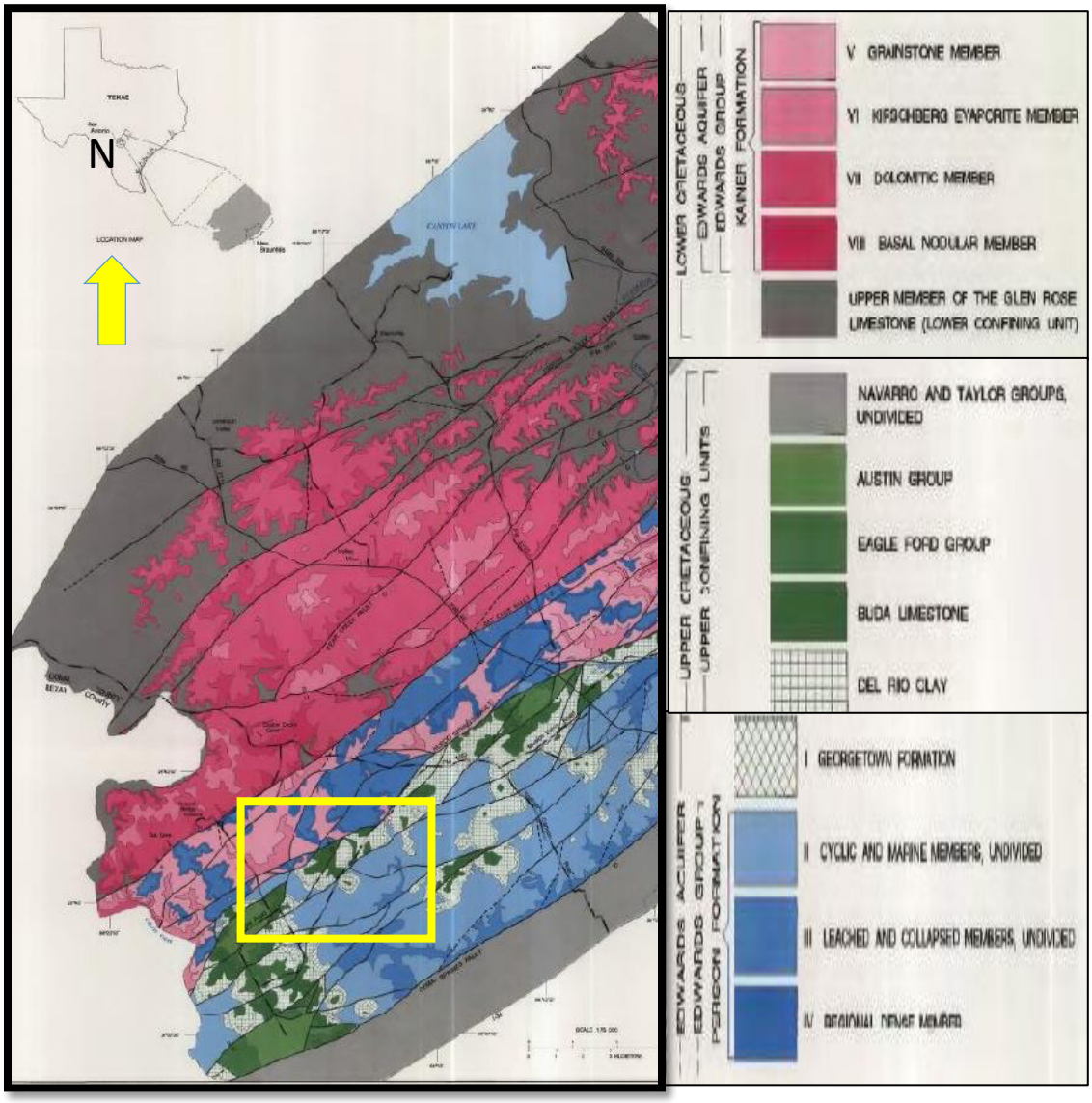

Figure 4.12: Map showing the regional surface geology of the Edwards aquifer in Comal County including the study area in yellow rectangle (Small, 1994).

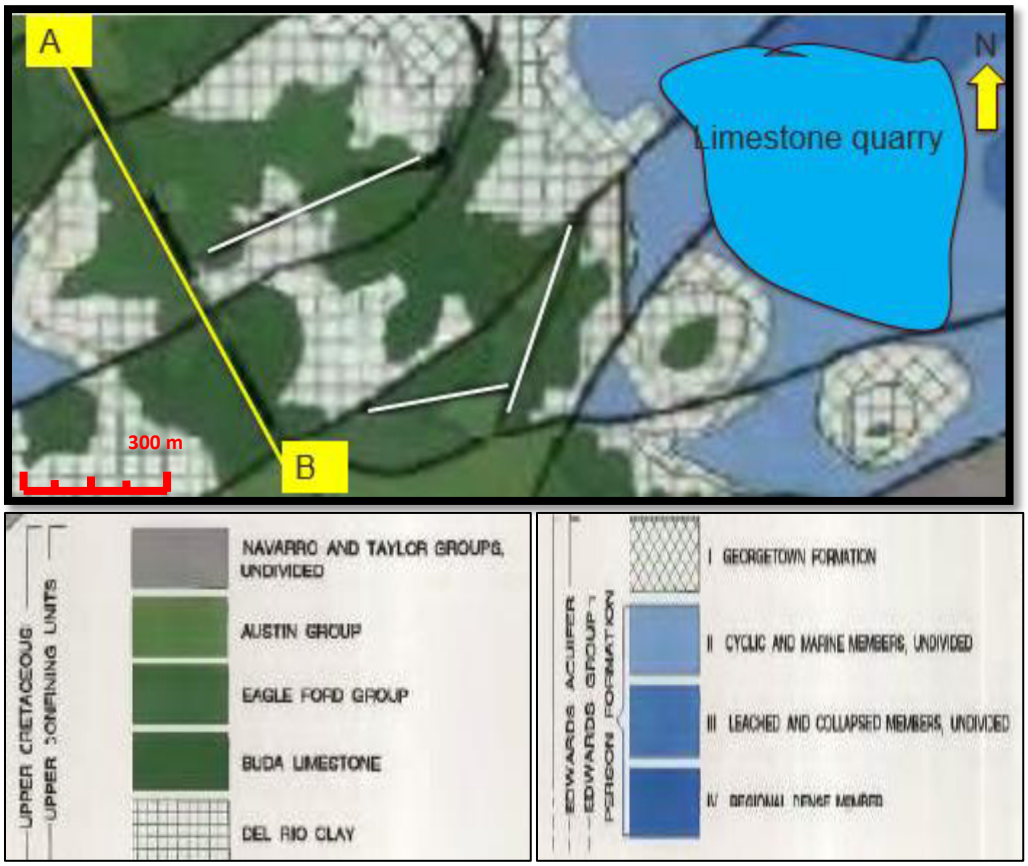

Figure 4.13: Map illustrating the surface geology of the study area (small, 1994). The location of the quarried Edwards limestone is roughly indicated. Black and white lines represent the major and minor faults, respectively).

4.2.1.3 Tectonic History and Regional Structure

The Balcones escarpment separates the Gulf Coastal Plain from the Edwards Plateau. The escarpment height ranges from 30 m to several hundreds of m above the adjacent lowland to the southeast. Large alluvial fans extend southward from some segments of the escarpment. The relief along the escarpment is controlled by en-echelon faults. The Balcones zone consists of primarily normal vertical faults as shown in Figures 4.14 A, D and 4.15 that are downthrown to the southeast by 4 m/km (George, 1952). This pattern of faults is intersected by numerous conjugate faults which are downthrown towards the north-east.

There are five primary faults in Comal County, namely, the Hueco, Comal Springs, Bat Cave, Bear Creek, and Hidden Valley faults (George, 1952). The first two faults offset the Edwards aquifer within the upper confining layers. This prevents surface water from recharging the aquifer. The Comal Springs fault is the most recognizable fault in the Balcones zone and serves to isolate the Gulf Coastal plain from the Edwards plateau.

Faulting, stratification, and karstification, displayed in Figure 4.15 (B and C), are amongst the factors that control hydrological properties such as permeability and porosity. According to studies made by Choquett and Pray (1970), two types of porosities characterize the carbonates in the study area: fabric-selective and non-fabric selective. Depositional and diagenetic processes that have acted on the strata during their formation are associated with fabric-selective porosities. Meanwhile, non-fabric porosity is linked to post-depositional factors. For example Cavities and sinkholes are predominant along the

escarpments. They were initiated by extensive dissolution of limestone. These cavities have increased the porosity and permeability of the drainage system significantly at some parts of the reservoir. This resulted in the interconnection of solution channels. Hence, the Edwards outcrops in this study area contains frequent and widespread burrowed and cavernous layers of limestone (Stein and Ozuna, 1995).

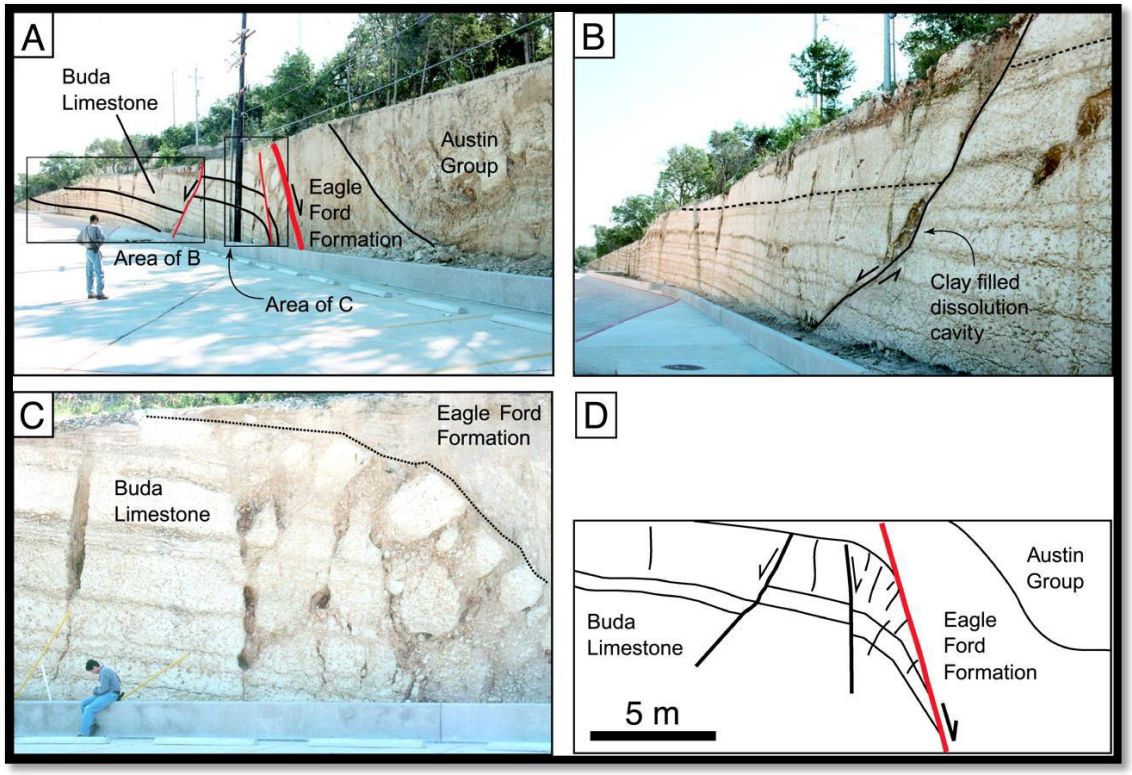

Figure 4.14: A-C: Photographs of an exposure of the Edwards's aquifer; D: Schematic diagram of the normal fault in the Balcones fault zone (Stein, 1995)

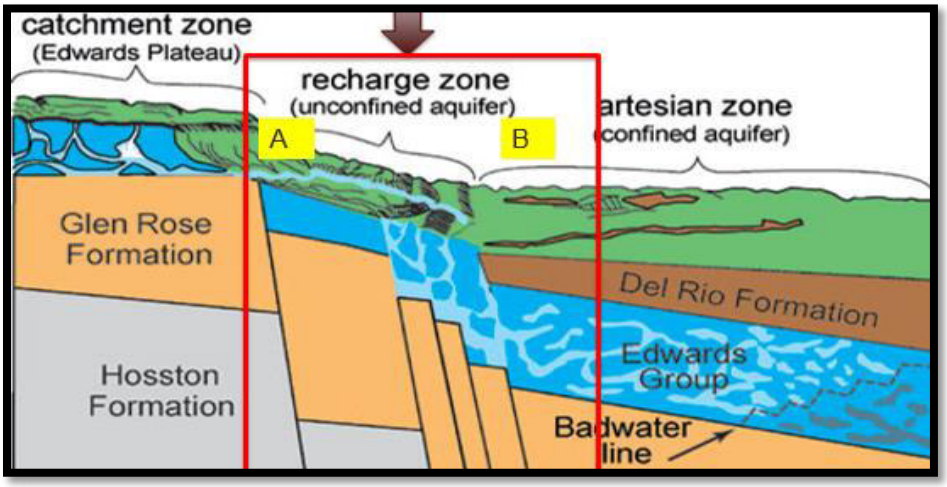

Figure 4.15: Cross section showing a simplified structure of the Balcones fault zone including the study area (marked by rectangular and arrow). (Stein, 1995)

4.2.2 Conceptual Geophysical Model

Based on the geological background, the complaint distribution, and the source-receiver azimuths (SRA) relative to the trend of the Balcones fault zone, the study area has been divided into 6 zones that are hypothesized to have different wave propagation characteristics. The source-receiver azimuth is the direction of the line joining a given source to a given receiver. The zones are shown in Figure 4.16. Generally, each zone is hypothesized to be either a fault zone or intact rock. The fault zones are commonly deformed and characterized by soft material (unconsolidated), while the host rock (hanging/foot wall) is characterized by undeformed material, i.e. hard soil (consolidated).

An important consideration is the source-receiver azimuth with regards to the assumed major faults. A Source-receiver azimuth can be parallel or oblique to the fault

strike, as displayed in Figure 4.17. For the zonation analysis, the seismic sources have been separated into northern and southern groups. The SRA of the northern group of shots is approximately parallel to the strike of the faults in zones 1, 2, and 3. Similarly, the source-receiver azimuths of the southern group of shots lie nearly parallel to the fault strike in zones 4, 5, and 6. Both groups also contain recorded seismic travel paths that intersect at oblique angles with the suggested major faults. The various paths between sources and receivers are sensitive to different seismic propagation mechanisms. For instance, fault zone trapped waves (FZTW) could be excited in some cases. FZTW propagate with low attenuation and thus result in high vibration levels at large ranges. This phenomenon may be one of the causes for high complaints in certain parts of the study area.

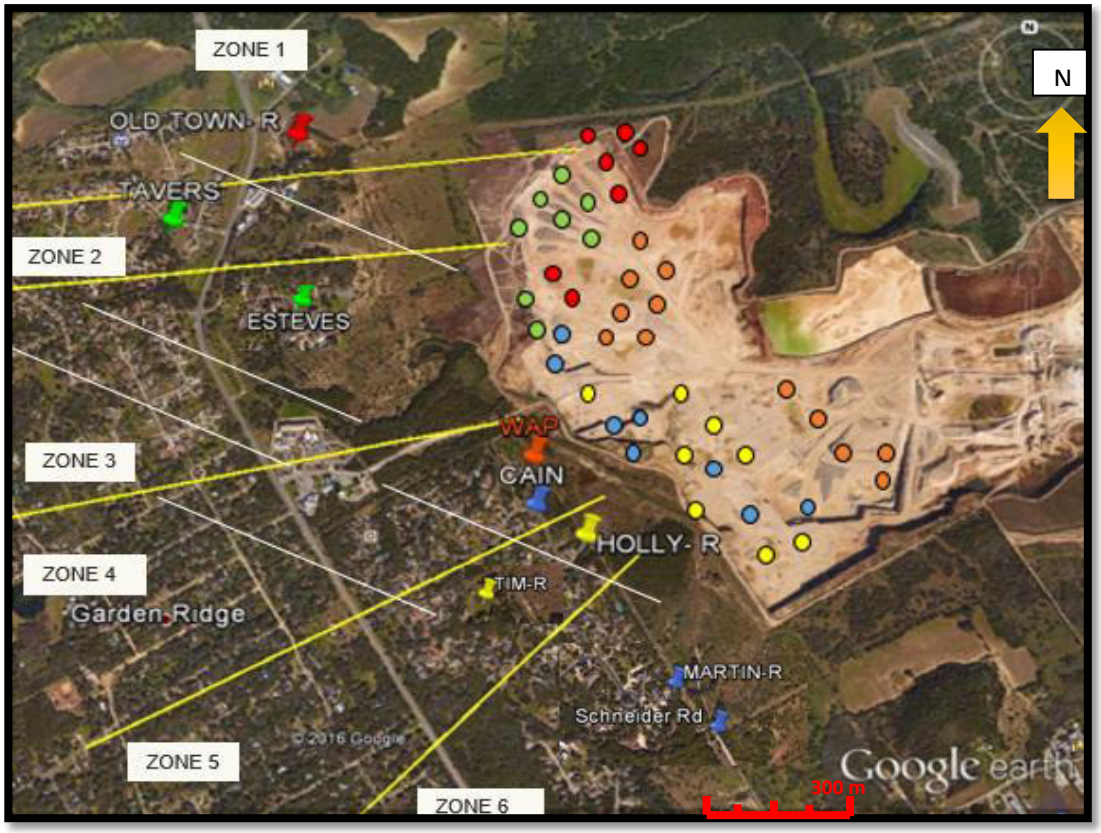

Figure 4.16: Satellite photo for study area divided into six zones of different hypothesized geological structure. The 5 major faults are indicated by the yellow lines. Note that the faults are not observed but are hypothesized to exist based on seismic and complaints. Minor faults are shown by the white lines. Small circles represent the blasting sources locations. Receivers have the same color of the active sources.

Figure 4.17: An example of six receivers which record the seismic waves that have source-receiver azimuth paralleled to the nearest major fault. Line between the source and the receiver represents the shortest travel path of the wave.

A preliminary investigation has been made in this study of the PPV and dominant frequency of blast events recorded by Vibra-Tech. Non-blast records caused by extraneous sources of vibrations or recording errors would have different PPV and dominant frequency. The histogram of the peak particle velocities in Figure 4.18 show that they fall into the range 0.020 - to 0.42 in. /sec. Furthermore, the dominant frequencies range from 3.20 to 40 Hz, as shown in Figure 4.19.

An initial analysis of the measured data was made by plotting the PPV and dominant frequencies versus the scaled distance as illustrated in Figures 4.20 and 4.21. The scaled distance used in these plots is defined by the USBM equation (Eq.4.1). PPV histogram shows Right-skewed distribution with mean PPV of 0.09 in/sec while the histogram of the dominant frequency shows Bimodal (double-peaked) distribution with mean frequency of 15 Hz. The the two peaks apparent on the dominant frequency histogram at 10.7 and 19.7 Hz can be attributed to the propagation of waves in two different geological structure. The measured data display a large scatter which is attributed in large part to the heterogeneity and structural variability of the geology surrounding the quarry area although we cannot exclude differences in the blast conditions due to variability at the quarry face.

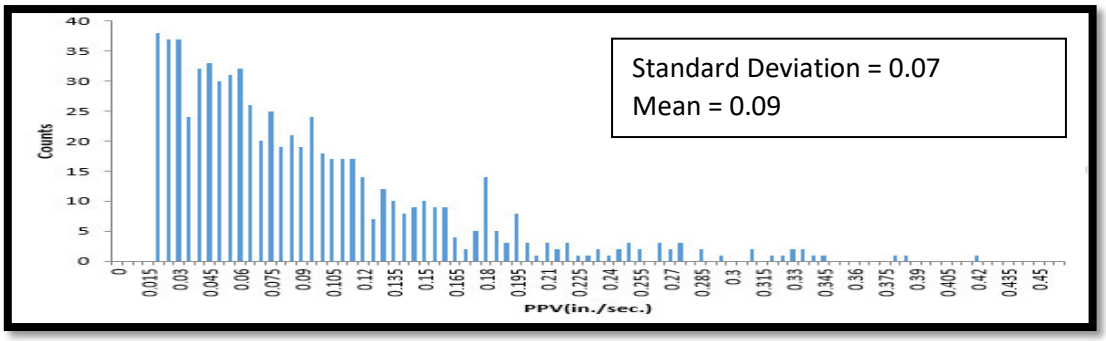

Figure 4.18: Histogram of the PPV values for the entire set of events measured in the study area.

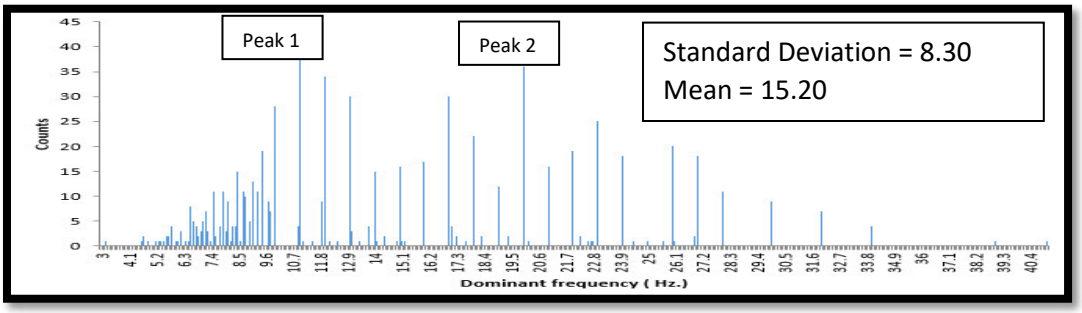

Figure 4.19: Histogram of the dominant frequency values for the entire set of events measured in the study area.

$$\text{Scaled distance} = \frac{R}{Q\ \max^{0.5}} \qquad \text{..... Equation 4.1}$$

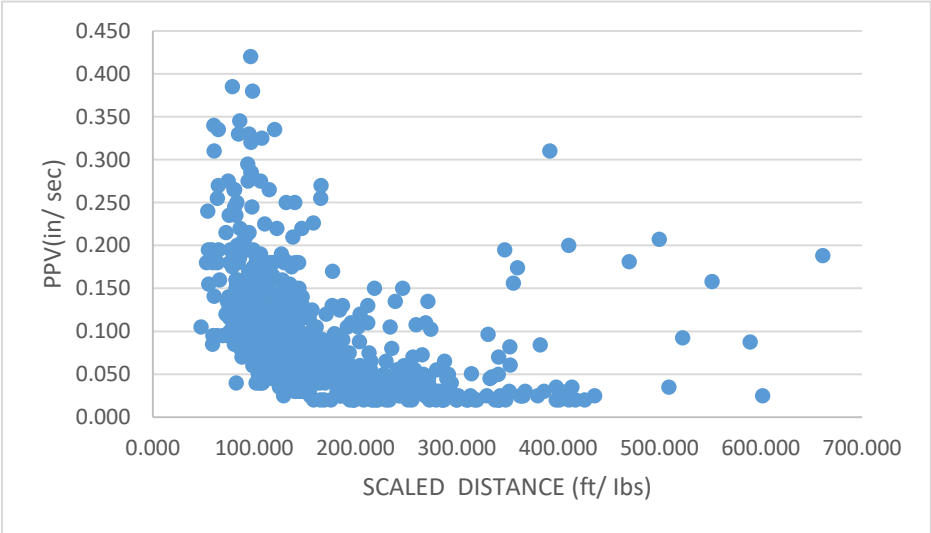

Figure 4.20: Peak particle velocities vs. the scaled distance of seismic arrivals.

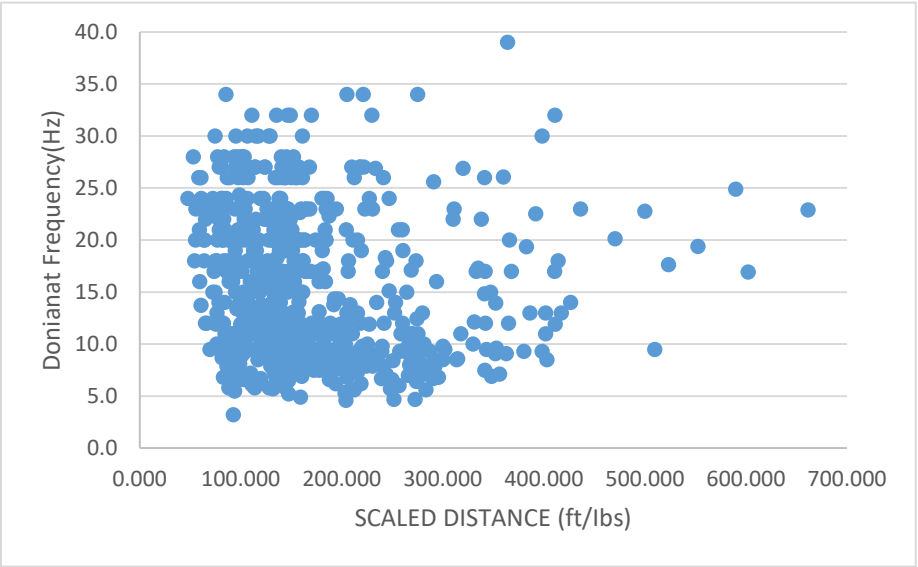

Figure 4.21: Dominant frequency vs. the scaled distance of seismic arrivals.

A comparison of PPV and dominant frequency recorded within individual zones has been made in support of the assumed seismic zonation model. In order to test the proposed zonation, an attempt was made to explore the unparalleled SRA with respect to the major faults separating the zones For instance, based on PPV and propagation velocities zones 1 and 2 are interpreted as an unconsolidated fault zone and consolidated host rock, respectively, (Figure 4.22). Figure 4.23 shows the two hypothesized major faults that bound the two zones, the receiver locations, and the corresponding blasting locations. Although the measurements in the two zones have almost the same scaled distance at the receiver location, the effect of the geological structure can be discerned by the differences in the PPV/dominant-frequency histograms.

The histograms in figures 4.24 and 4.25 represent the PPV and the dominant frequencies recorded from the upper region of the quarry (northern shot group), which contain SRA's that are parallel to the Balcones fault trend. A partitioning in the histograms (Figures 4.24 and 4.25) of the measured PPVs and dominant frequencies has been found. The histograms show a clear distinction in the vibration response parameters between the two zones 1 and 2 indicating different geological and geophysical characteristics. Zone 2 is characterized by lower values of PPV and higher dominant frequencies, whereas zone 1 is characterized by relatively high PPV with lower dominant frequencies. In accordance with Dowding (1996) who concluded that soft soils generate high PPV and hard rocks produce relatively lower PPV, the two zones are interpreted as such.

It is worth mentioning that the entire data set has been evaluated at the same scaled distance range of 4.5-5.5 ft /lb to compensate for the different source weights and source-receiver distances. An assumption is made that the wave energy does not significantly vary within each range of scaled distance. In other words, it is assumed that the intrinsic attenuation of the rocks and faults have the foremost control over the vibration parameters This also aids in decreasing the effect of geometrical spreading and the variations in the blast design.

Figure 4.26 displays two sample seismic traces from the same blast events, one for zone 1 and the other for zone 2. The plots show the recorded particle velocities of the longitudinal component at receivers OLD and TAVERS over a time interval of 100-390ms after the blast. The seismic trace on the left side represents propagation through the putative fault zone, which as described earlier is hypothesized to be filled with

unconsolidated materials. The trace displays late-arriving low-frequency signals with strong amplitudes. The seismic trace on the right side is from the relatively consolidated rocks assumed to be a horst block. It displays a different character, namely a lower amplitude with a relatively lower propagation velocity and higher frequency. The lower propagation velocity can be attributed to the presence of perpendicular minor faults that attenuate seismic waves in zone 2.

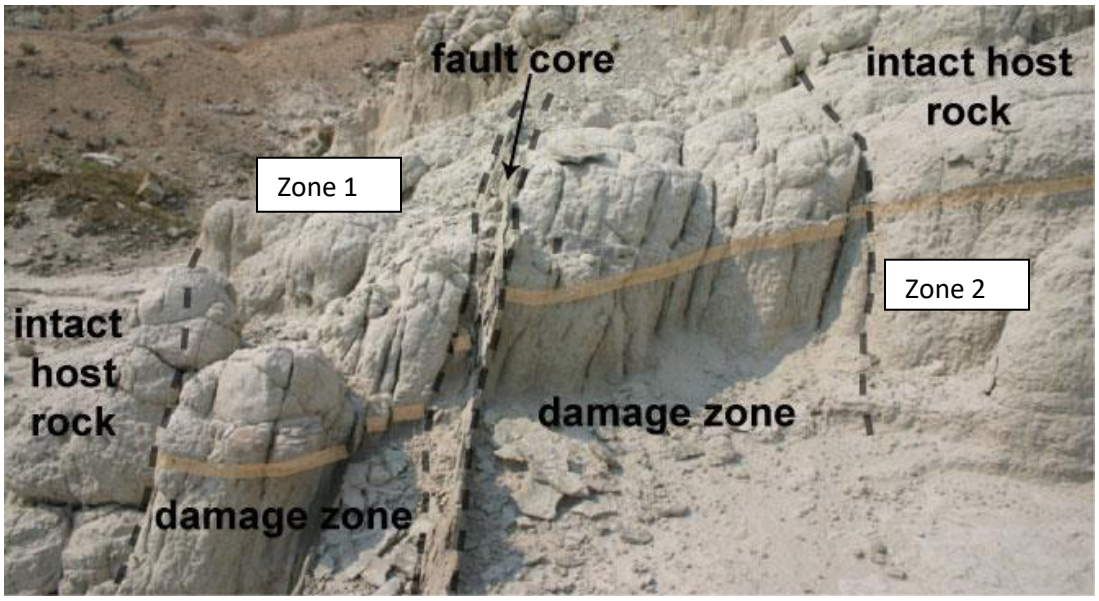

Figure 4.22: Photographic photo of the fault zone illustrate the definition of intact host rock and unconsolidated damage zone (Ferrill, 2014).

Figure 4.23 Satellite photo of the study area showing the locations of the blast sources and their corresponding receivers in zones 1 and 2.

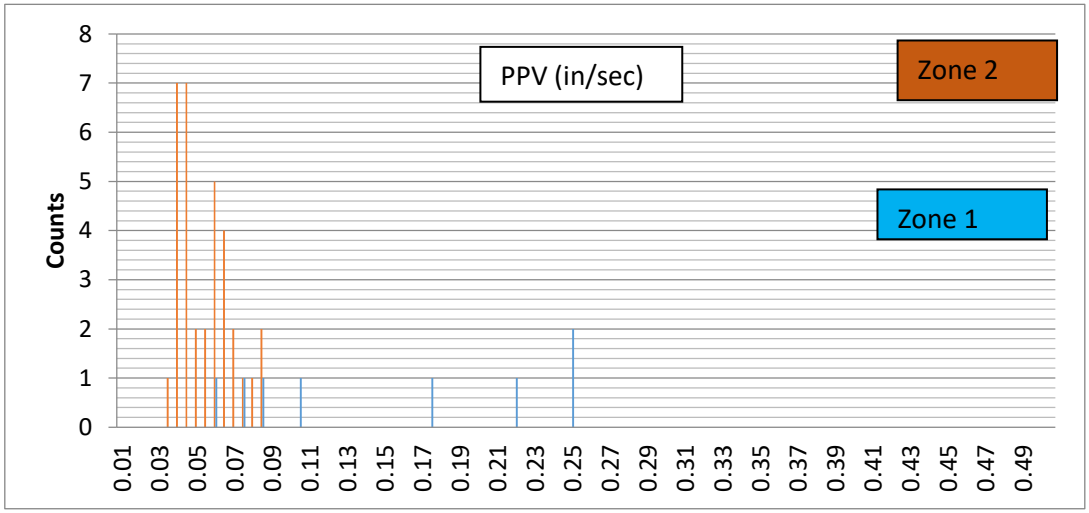

Figure 4.24: Histograms of the PPV measured in zone 1 and 2 at scaled distance of 5.5ft /lbs. The data Show a distinctive differences in the PPV values between the two zones

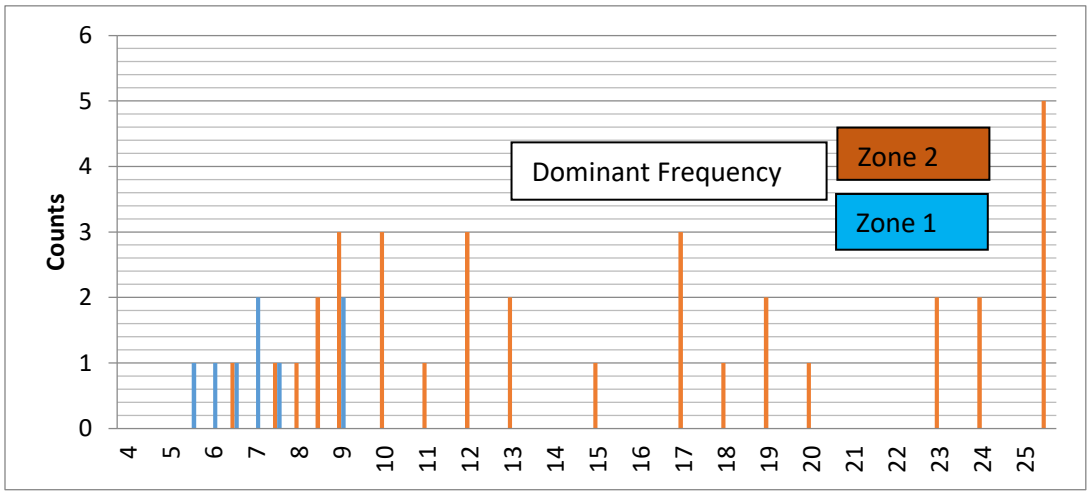

Figure 4.25: Histograms of the dominant frequency measured in zone 1 and 2 at scaled distance of 5.5 ft /lbs. The data Show a distinctive differences in the dominant frequency values between the two zones

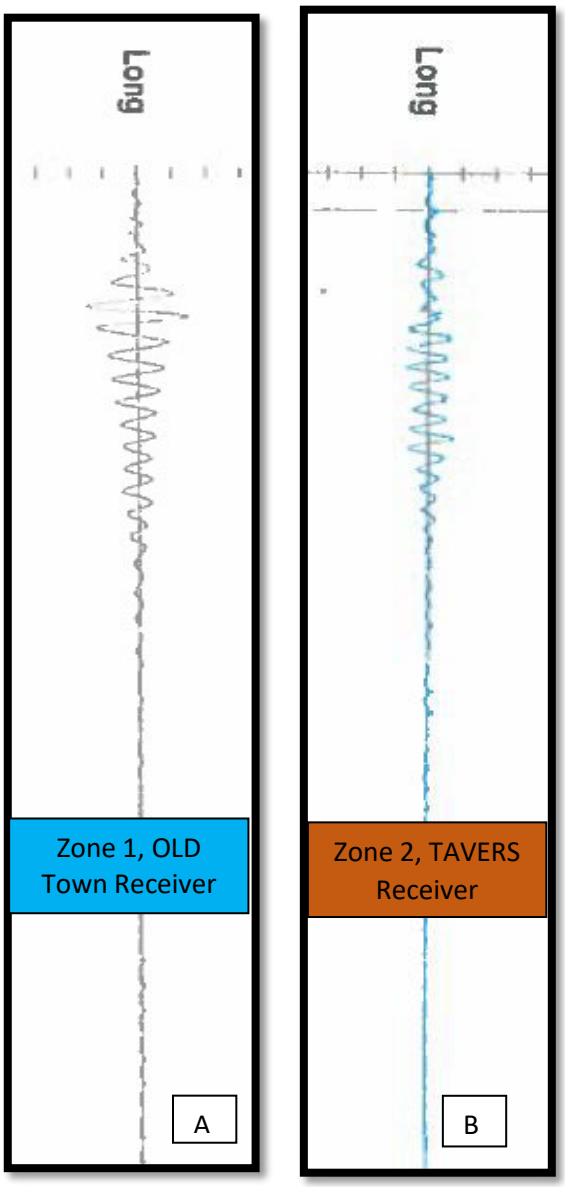

Figure 4.26: Two seismic traces (longitudinal component) measured in zone 1(A) and 2 (B). Amplitude differences between the measurements possibly due to the effect of the trapped waves in the fault zones, are observed

In comparison with the other zones, zones 4 and 5(shown in Figure 4.28), appear to possess more complex geology which increased the scattering of the data. This is based on an interpretation of the differences in the histograms of these two zones. The Histograms of the PPV shown in Figure 4.28, enable a resolution between the two zones. However, the frequency plots illustrated in Figure 4.29 do not indicate any clear difference between the two zones. Relatively low PPV is observed in zone 5, while zone 4 shows a higher range with larger PPV values. Once more, zone 4 could be interpreted as unconsolidated fault rock/soil and zone 5 as consolidated host rock. However, the PPV values in zone 5 are considerably higher compared to those in zone 1. This can be attributed to a more detailed geological structure such as minor faults oriented along the Balcones trend. The minor faults could increase the generation of trapped waves which would raise the PPV values. However, the frequency content in these zones is still difficult to interpret.

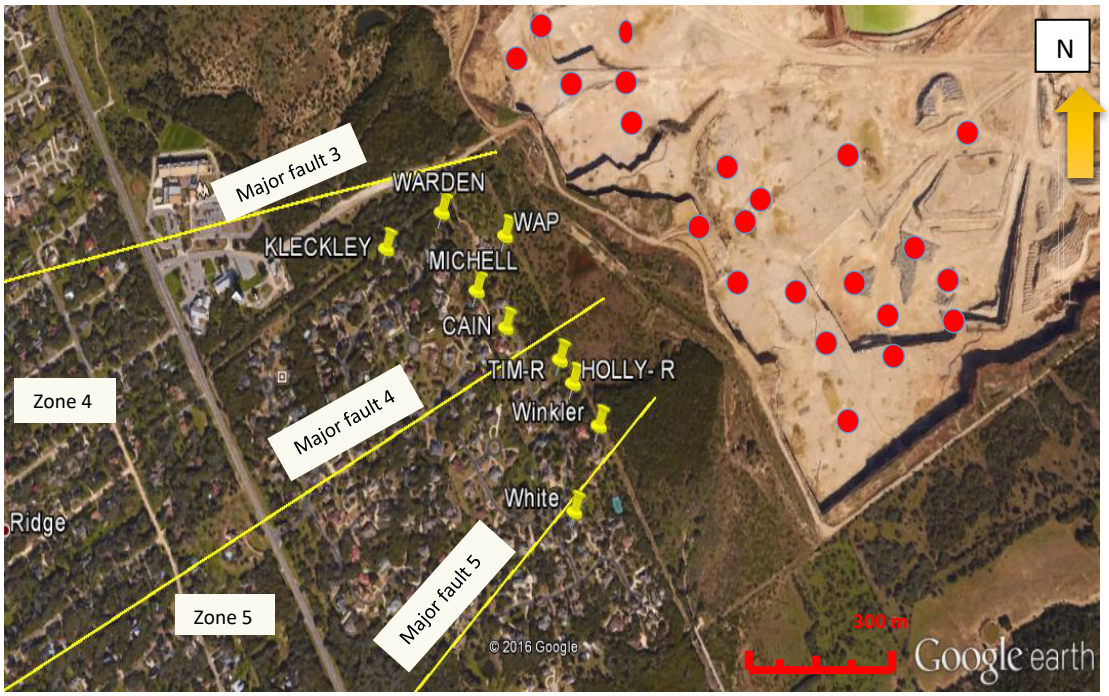

Figure 4.27: Satellite photo of the study area showing the locations of the blasting sources with respect to zones 3, 4 and 5

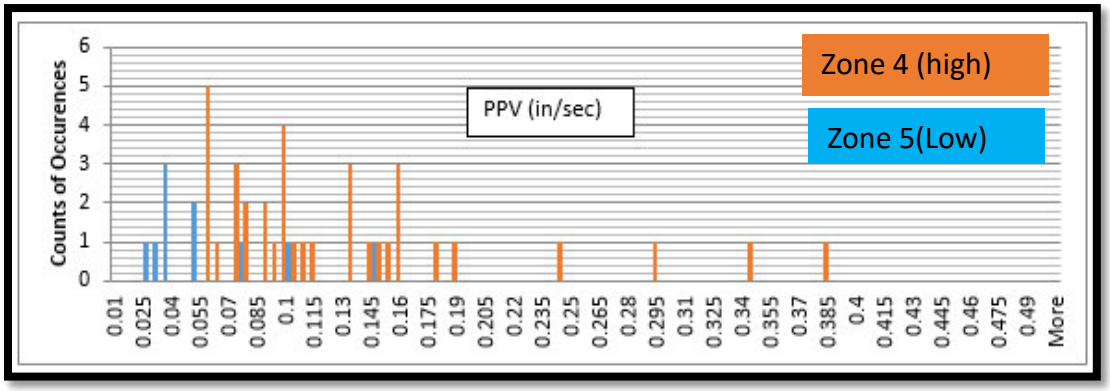

Figure 4.28: Histograms of the PPV at zone 4 and 5. The differences in the PPV values between the two zones are apparent.

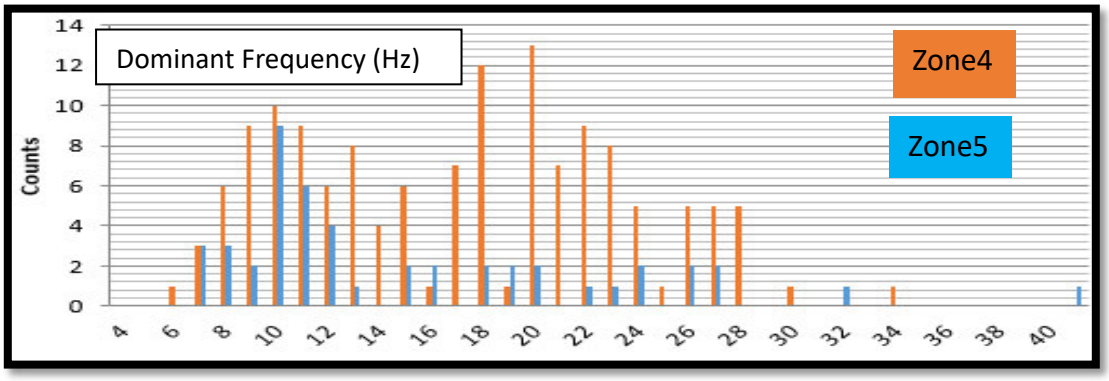

Figure 4.29: Histograms of the dominant frequency at zone 4 and 5. The differences in the frequency values between the two zones iare apparent.

4.2.3 Summary of the Conceptual Model

As indicated in Figure 4.7, the quantitative analysis of vibrations in the Garden Ridge neighborhoods is based on geological and geophysical conceptual models. Giving the PPV histograms, geological background, and the SRA, the conceptual model has been developed as follows. The study is located within the Balcones fault zone with predominant northeastern strike faults and downthrown blocks towards the south-east. Most of the sedimentary rocks in the quarry such as the Edwards limestone comprise an efficient aquifer in the San Antonio area due to high fresh water saturation and continuous recharge. The effect of partially and fully water-saturated soils on seismic propagation has been studied by many authors including Zhao (2005).

Generally, the changes in the PPV values are controlled by the degree of rock consolidation, water saturation, and the intensity and/or orientations of the discontinuities (minor and major faults). There is a weak dependence of PPV on lithology type. The analysis of the PPV and dominant frequency is linked to the effects of the controlling factors on wave propagation. Due to the fact that the regional tectonics controlled the development of the normal faults in the study area, two types of rocks are assumed to exist. Namely, these include the undeformed rock in the host rock and the unconsolidated soft rock in the fault zone, as illustrated in Figures 4. 32 and 4.33.

Consequently, five hypotheses are proposed to explain the observed PPV values around the quarry. The claim is that the PPV is controlled by one or more of the following scenarios related to the propagation of seismic waves : (1) a continuous (with no faults) consolidated or unconsolidated medium; (2) a discontinuous medium including minor

faults that are semi-parallel or conjugate to the source-receiver azimuth; (3) a discontinuous medium with 5 major faults; (4) propagation occurs across a contact between two different lithology types; (5) topographic irregularities causing diffraction and focusing of seismic waves. The five hypotheses mentioned above are evaluated using the process of forward modelling.

The generation of trapped guided waves in the semi-parallel faults is suggested to be the main propagation mechanism contributing to increased PPV values within the faulted zones. Constructive interference and multiple reflections at the zone boundaries produce high amplitudes. This is evident in the PPV histograms and the sample seismic traces from zones 1 and 4. Fault-trapped waves are identified by their higher amplitudes relative to the other zones. Consequently, the considerable high complaints' values (3 to 5) for the residents living in these zones can be attributed to the existence of their homes close to surface fault traces. This proximity allowed the homes to be affected by the guided Rayleigh waves which possess high amplitudes near the surface. Meanwhile, the foot and/or hanging walls in zones 2 and 5, comprised of relatively consolidated material, provide an efficient pathway for wave propagation. Consequently, the effects of surface blasting vibrations are minimized in these zones. This decrease was detected in the sample seismic traces possessing a relatively lower amplitude.

Moreover, the placement of the Edwards limestone adjacent to Delrio clay, could be responsible for the amplification observed in all of the zones. For example, different locations in zone 3 such as Esteve show an amplifications in the PPV values, even though they were measured at the standard scaled distance (equal blasting energy and same

distance). This can be attributed to the transmission of the wave across the interface (sedimentary contact or fracture) between two different acoustic impedance.

PPV values can are also sensitive to the degree of fluid saturation. Fluid phase alterations can largely affect the soil elastic properties which in turn affects the vibration response. The behavior of elastic waves Propagation and attenuation through porous medium a containing fluids has been a subject of great importance because of its various applications. Fluid inclusions include air which has a small mass and high compressibility with a P-wave velocity of only 343 m/s. The existence of water causes an increase in the density and bulk modulus relative to fully air-filled soils .This effect increases the compressional wave velocity while decreasing the S-wave velocity. Biot (1956) proposed the theory of poroelasticity which provided a dynamic mechanical model that account for the solid-fluid interactions and body wave propagation. Despite of the significant development in the application of Biot theory on Rayleigh wave propagation in a single fluid system, the behavior of the Rayleigh wave motions in systems with two immiscible fluids (ex. Water and air) is still deficient (Lo, 2008).

Fault zones in the study area are typically characterized by a high porosity in the form of void spaces in loose materials, small fractures, and cavities. These voids could be saturated with fresh water and small air pockets. The compressional velocity of water has a value of 1480 m/s while the velocity range in water-bearing soils are between 1450 m/s to 1900 m/s (Butler, 2005). However, factors such as salinity, total dissolved solids (TDS), and the internal rock structure can also affect the propagation velocity.

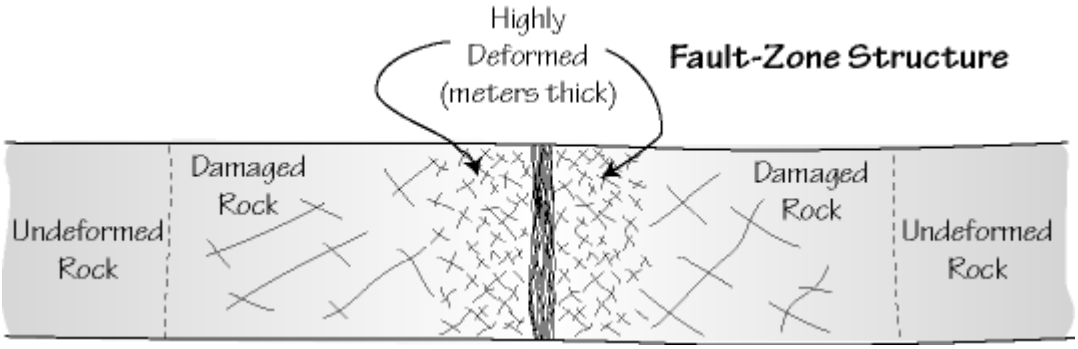

Figure 4.32: Theoretical cross-section showing the type of tectonics existing in the study area (Zhao, 2005).

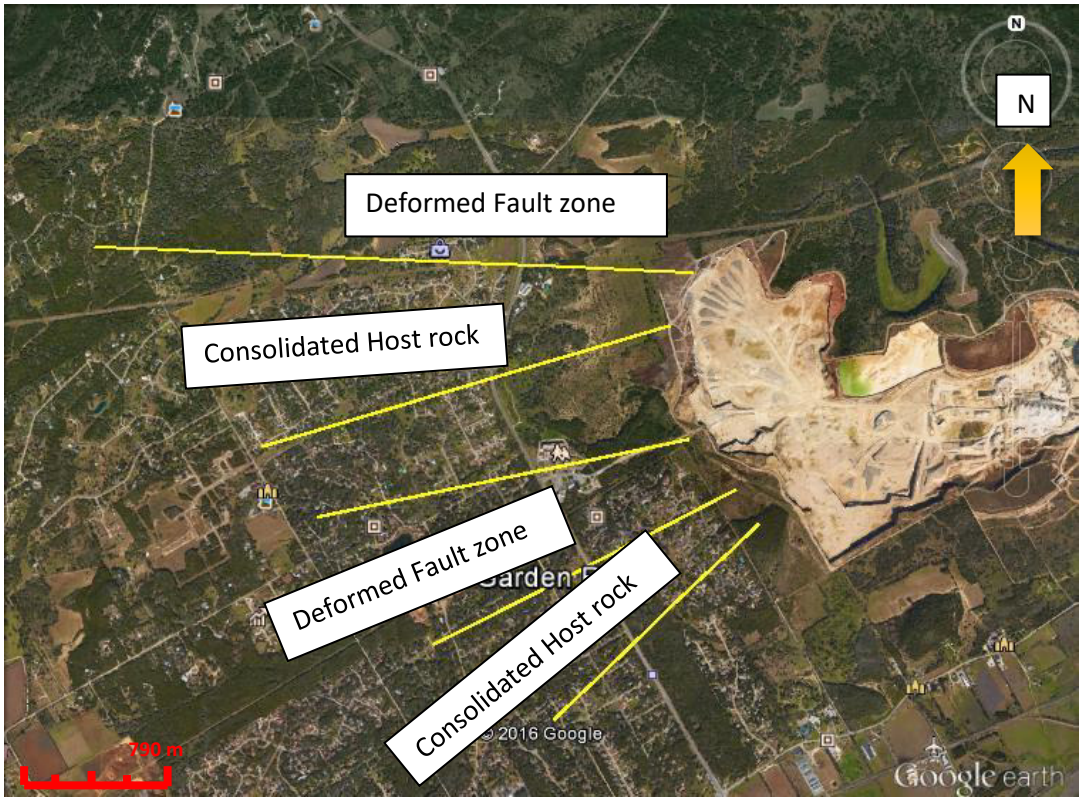

Figure 4.33: Satellite photo of the study area showing the proposed 6 geological zones

The dominant frequency of several blasts fell in the range 4-18 Hz which is a critical frequency for many types of structure. Energy in this frequency range can increase the amplification of the ground vibrations due to its proximity with the natural frequency of the ground and infrastructure. Based on the characteristics of wave propagation in fault zones and the effect of water saturation, the distribution pattern of the PPV in the study area can be interpreted accordingly.

The data have suggested a general qualitative agreement with the conceptual model that has been proposed. However, a detailed quantitative based analysis is still needed to achieve an accurate geological structure. The next section provides an overview of the development of three types of modelling approaches and their efficiency. Such approaches include the empirical, artificial intelligent neural network, and finite element methods. The evaluation of the proposed 5 hypotheses using these approaches is discussed in chapter 5.

4.3 Forward Modelling Approaches

4.3.1 Semi-Empirical Approaches

In this study, eight empirical formulas, shown in Table 4.6 (Amneieh et al., 2013) and drawn from the literature, for the PPV prediction around the Hanson quarry in Garden Ridge city have been tested and compared for efficiency against the vibration Vibra-Tech dataset. Nonlinear regression analysis has been applied using SPSS and MATLAB software in order to determine optimum values for the different parameters found in the empirical formulas. In addition, a new empirical formula has been proposed and tested using the same procedure. This new formula shows a good match against field measurements at the majority of the receiver locations. The testing procedure has been divided into two phases based on measurement locations. The process of data zonation was executed according to the conceptual model described earlier and the assumed characteristics of wave prorogation in the study area. The zonation was done in order to decrease the scatter found in the PPV values and to minimize the associated uncertainty. As previously mentioned in the discussion of conceptual models, the data scattering can be attributed in large part to the heterogeneity and anisotropic characteristics of the geological structure surrounding the quarry area. The zone boundaries have been altered multiple times through the validation processes in order to reach the best distribution. The proposed empirical equation has also been modified to match the measured data at most of the receiver locations.

In addition, the PPV values in the three mutual orthogonal directions for each zone, namely the transverse, vertical, and longitudinal, have been modelled separately at a

number of receiver locations. The optimum parameters in the empirical formula for each receiver location was determined and they are summarized in the following tables. The next section describes the procedures used to determine these optimal model parameters.

Table 4.6: Most common empirical equations used for the prediction of the PPV (Amneieh et al., 2013)

1	USBM(1959)	$PPV = k\left[R/\sqrt{Q_{\max}}\right]^{-\beta}$
2	Langefors-Kihlstrom(1963)	$PPV = k\left[\sqrt{Q_{\max}/R^{3/2}}\right]^{\beta}$
3	Davies et al.(1964)	$PPV = kR^{-\alpha}\left(Q_{\max}\right)^{\beta}$
4	Ambraseys-Hendron(1968)	$PPV = k\left[R/\left(Q_{\max}\right)^{1/3}\right]^{-\beta}$
5	Bureau of Indian Standard(1973)	$PPV = k\left[Q_{\max}/R^{2/3}\right]^{\beta}$
6	Just-Free(1980)	$PPV = k\left[R/\left(Q_{\max}\right)^{1/3}\right]^{\beta} e^{-aR/(Q_{\max})^{1/3}}$
7	Ghosh-Daemen(1983)	$PPV = k\left[R/\sqrt{Q_{\max}}\right]^{-\beta} e^{-aR}$
8	CMRI (1993)	$PPV = n + k\left[R/\sqrt{Q_{\max}}\right]^{-1}$

4.3.1.1 Model Development

Peak Particle Velocity (PPV) and dominant frequency values of ground motion from quarry blasting are usually estimated from empirical equations derived from field experiments. Numerous empirical equations for PPV have been developed by authors who used different types of formulas. The development of the empirical equations is usually based on simplifying the behavior of energy propagated through the ground. This is done in order to find simple equations which can predict PPV values empirically via the estimation of a small number of constants or parameters. As previously mentioned, there are eight commonly used empirical formulae for PPV, which differ according to the basic assumptions involved in modelling seismic wave propagation. These formulae are non-linear but they can be rewritten in a linear form using the logarithmic transformation (Draper and Smith, 1966).

Scaling the distance is required in the process of PPV predictions to account for the fact that the source strength is variable. The quantities shown in Table 4.5 are considered by Ambrasays (1968) to be the most important governing parameters of blasting vibrations. As stated by the Buckingham pi theorem of Langhaar (1951), six dimensionless parameters can be related to the blasting vibrations. These parameters include U/R, PV/C, AR/C^2 , FT, TC/R, and $Q/rC^2 R^3$ (see Table 4.7 for definitions of the symbols).The theorem also mentioned that the above-mentioned combination of variables can be raised to any power and multiplied together in order to form an accurate PPV prediction model.

Most of the empirical equations have neglected the spatial variations in the and rock density (ρ) propagation velocity (V). Accordingly, in this study, a new equation, as shown in Equation 4.9, has been proposed which incorporates these parameters into the predictive model. Investigating the effects of the abovementioned parameters, numerous trials were performed giving a new power exponent to the weight of charge. For the sake of simplicity, some assumptions have been retained such as the purely elastic behavior of the soil at the location of measurement and constant blasting conditions at all of the blasting sites.

Table 4.7: Summary of the independent and dependent variables that constitute the prediction formulae. After Ambraseys (1968).

Independent Parameters	
Maximum weight of charge	Q
Source receiver distance	R
Propagation velocity	C
Time	T
Density of soil/rock	ρ
Geometrical spreading Coefficient	B
Dependent Parameters	
Max. Displacement	U
Max. particle velocity	PV
Max. Acceleration	A
Frequency	F
Attenuation coefficient	$\boldsymbol{\alpha}$

$$PPV = (R * \rho * V^2/Q_{max}{}^{(\frac{1}{7})})^{-B} * Exp^{(\alpha * R)} \quad \ldots\ldots\ldots\ldots\ldots \text{ Equation 4.9}$$

4.3.1.2 Model Validation

First Phase

Data Preparation

According to the conceptual geological model, the evaluation of the various semi-empirical formulas starts by dividing the area into six zones, separated by 5 major faults. Consequently, each receiver has recorded a PPV value with an SRA that is either parallel or intersects with the assumed fault strike. The first phase is devoted to find the optimum empirical equation that is able to best predict the PPV values recorded at the 22 receivers from all SRA. The all-SRA data represent those PPV values measured from both the parallel and the azimuths that intersect the nearest assumed major fault. Each zone is characterized by different geological and geophysical properties that affect the attenuation coefficient.

The PPV prediction at each receiver location has been individually tested by all equations. However, in some cases the receivers belonging to the same zone are tested together to give a single attenuation relation that is valid for the entire zone, for instance this has been done for zones four and six. Figure 4.34 below shows an example of four selected receivers that record the vibrations from blasting sources located at different azimuths relative to the strike of the assumed faults.

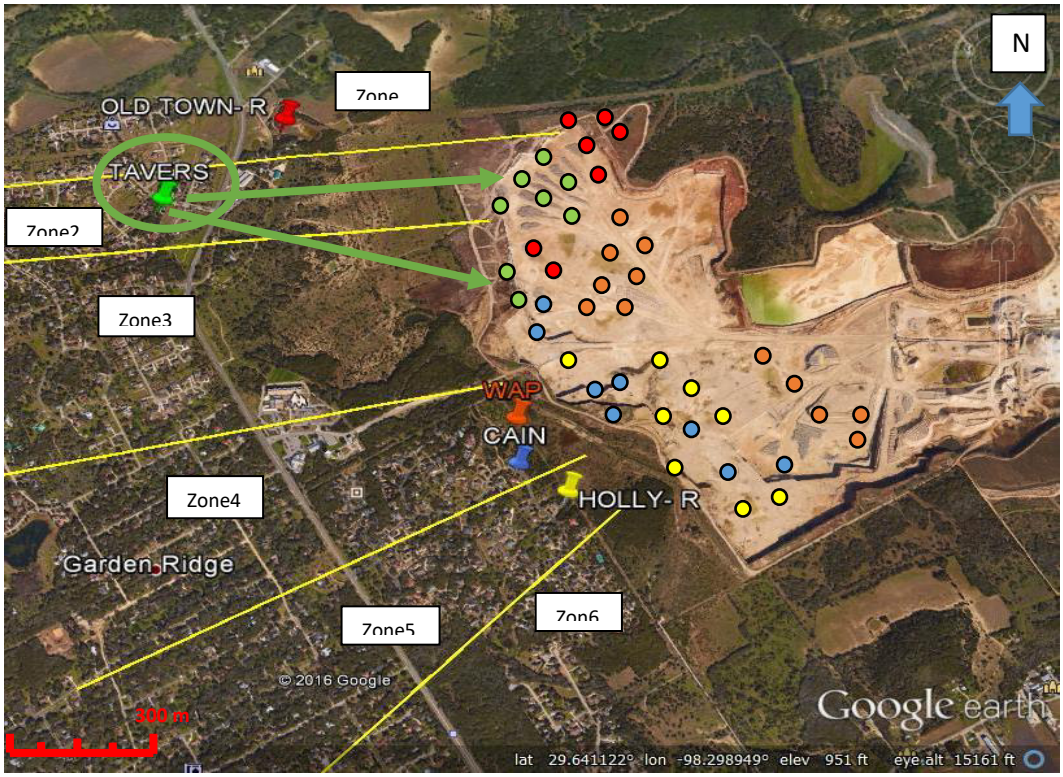

Figure 4.34: Locations of four receivers and their corresponding blasting sources. For each receiver the blasting sources are indicated with the same colors. Green arrows show the difference in measurement azimuth at TAVERS location.

Regression Results

An individual regression analysis has been performed on the PPV values measured by each receiver. The results of the non-linear regression process for the nine empirical equations using the PPV at each receiver location are tabulated. Tables 4.8 to 4.18 display such tables for selected locations in the six zones. Specifically, eight tables illustrate the test parameters using one receiver at a time, namely the OLD, TAVERS, ESTEVE, WAP, CAIN, WARDEN, HOLLY and SCHNEIDER locations. While, the remaining three tables (Table 4.16 to 4.18) comprise the best-optimized parameters using more than one receiver from zones 3, 4 and 6. Various parameters such as K, B, N, A, ρ and the attenuation coefficient (α) are provided. The table headings show the geographical position of each receiver and its best empirical equation.

Table 4.8: The best-fit parameters for all the empirical equations used in the prediction of OLD receiver data. OLD Receiver (Zone 1) - Non- Linear Regression. Best equation is the Proposed Equation 4.9						
Empirical Model	**K**	**B**	**C**	**Average α**	**N**	**R^2**
USBM	1.04	------	------	------	0.44	0.09
AMB-HEND	4.56	------	------	------	0.60	0.1
DAVIES	9.78	2.23		------	------	**0.37**
GH-DAE1	3.26	------	------	0.01	-2.57	0.37
GH-DAE2	3.26	------	------	0.01	-7.71	0.38
CMRI P.	7.36	------	0.06	------	1.00	0.07
LANG-KIHL	0.10	------	------	------	0.22	0.01
INDIAN	0.10	------	------	------	0.11	**0.43**
PROPOSED	5.10	1.33	------	0.03	0.13	**0.52**

Table 4.9: The best-fit parameters for all the empirical equations used in the prediction of POST receiver data. POST Receiver (Zone 2) - Non- Linear Regression. Best equation is the Indian Equation 4.5						
Empirical Model	**K**	**B**	**C**	**Average α**	**N**	**R^2**
USBM	0.16	------	------	------	0.21	**0.01**
AMB-HEND	0.21	------	------	------	0.21	0.01
DAVIES		2.11				
GH-DAE1		------	No correlation is found. Correlation factor is extremely low			
GH-DAE2		------				
CMRI P.	2.45	------	0.04	------	1	0.01
LANG-KIHL	0.04	------	------	------	0.39	0.01
INDAIN	0.04	------	------	------	0.19	**0.79**
PROPOSED	3.78	1.45	------	0.02	0.22	**0.55**

Table 4.10: The best-fit parameters for all the empirical equations used in the prediction of WARDEN receiver. Warden Receiver (Zone 4) - Non- Linear Regression. Best equation: Proposed Equation 4.9						
Empirical Model	**K**	**B**	**C**	**Average α**	**N**	**R^2**
USBM	1.09	------	------	------	0.44	0.08
AMB-HEND	4.71	------	------	------	0.60	0.20
DAVIES	9.98	2.29		------	------	**0.35**
GH-DAE1	3.37	------	------	0.02	-2.57	0.34
GH-DAE2	3.19	------	------	0.01	-7.71	0.28
CMRI P.	7.57	------	0.09	------	1.00	0.05
LANG-KIHL	0.15	------	------	------	0.22	0.01
INDIAN	3.27	------	------	------	0.19	**0.41**
PROPOSED	7.89	2.11	------	0.01	0.32	**0.57**

Table 4.11: The best-fit parameters for all the empirical equations used in the prediction of WAP receiver. WAP (Zone 4)- Non- Linear Regression. Best equation: Proposed Equation 4.9						
Empirical Model	K	B	C	Average α	N	R^2
USBM	1.08	------	------	------	0.41	0.07
AMB-HEND	4.73	------	------	------	0.61	0.22
DAVIES	9.97	2.23		------	------	0.26
GH-DAE1	3.36	------	------	0.02	-2.51	0.31
GH-DAE2	3.12	------	------	0.01	-7.71	0.21
CMRI P.	7.59	------	0.08	------	1.00	0.08
LANG-KIHL	0.14	------	------	------	0.23	0.03
INDIAN	3.11	------	------	------	0.40	0.50
PROPOSED	6.45	2.13	------	0.00	0.30	0.56

Table 4.12: The best-fit parameters for all the empirical equations used in the prediction of CAIN receiver. CAIN (Zone 4) - Non- Linear Regression. Best equation: Proposed Equation 4.9						
Empirical Model	K	B	C	Average α	N	R^2
USBM	1.07	------	------	------	0.43	0.06
AMB-HEND	4.61	------	------	------	0.81	0.13
DAVIES	9.65	2.23		------	------	0.25
GH-DAE1	3.36	------	------	0.02	-2.42	0.21
GH-DAE2	3.13	------	------	0.01	-7.71	0.21
CMRI P.	7.59	------	0.08	------	1.00	0.07
LANG-KIHL	0.13	------	------	------	0.24	0.03
INDIAN	5.67	------	------	------	0.10	0.42
PROPOSED	4.12	1.95	------	0.01	1.10	0.43

Table 4.13: The best-fit parameters for all the empirical equations used in the prediction of HOLLY receiver. HOLLY (Zone 5) - Non- Linear Regression. Best equation: Proposed Equation 4.9						
Empirical Model	K	B	C	Average α	N	R^2
USBM	1.04	------	------	------	0.44	0.09
AMB-HEND	4.56	------	------	------	0.60	0.1
DAVIES	9.78	2.23		------	------	0.37
GH-DAE1	3.26	------	------	0.01	-2.57	0.37
GH-DAE2	3.26	------	------	0.01	-7.71	0.38
CMRI P.	7.36	------	0.06	------	1.00	0.07
LANG-KIHL	0.10	------	------	------	0.22	0.01
INDIAN	4.15	------	------	------	0.31	0.50
PROPOSED	3.26	2.00	------	0.00	1.20	0.79

Table 4.14: The best-fit parameters for all the empirical equations used in the prediction of TIM receiver. TIM (Zone 5) - Non- Linear Regression. Best equation: Indian Equation 4.5						
Empirical Model	K	B	C	Average α	N	R^2
USBM	3.13	------	------	0.01	-7.61	0.21
AMB-HEND	7.69	------	0.08	------	1.10	0.08
DAVIES	0.14	------	------		0.34	0.03
GH-DAE1	3.23	------	------	0.01	-7.81	0.22
GH-DAE2	7.39	------	0.08	------	1.00	0.06
CMRI P.	7.59	------	0.08	------	1.00	0.08
LANG-KIHL	0.14	------	------	------	0.23	0.03
INDIAN	1.99	------	------	0.005	1.20	0.46
PROPOSED	5.47	1.50	------	0.001	0.01	0.40

Table 4.15: The best-fit parameters for all the empirical equations used in the prediction of MARTIN receiver. MARTIN (Zone 6)- Non- Linear Regression. Best equation: Indian Equation 4.5						
Empirical Model	K	B	C	Average α	N	R^2
USBM	11.39	------	0.08	------	1.02	0.06
AMB-HEND	7.31	------	0.06	------	0.02	0.30
DAVIES	0.20	------	------		0.23	0.03
GH-DAE1	2.13	------	------	0.03	-7.61	0.01
GH-DAE2	7.59	------	0.03	------	1.10	0.07
CMRI P.	0.32	------	------	------	0.34	0.03
LANG-KIHL	3.02	------	------	0.02	-7.81	0.21
INDIAN	7.69	0.32	------	0.002	-7.61	0.89
PROPOSED	0.14	0.90	------	0.003	1.10	0.53

Table 4.16: The best-fit parameters for all the empirical equations used in the prediction of ESTEVE & SIDES receiver. ESTEVE, SIDES (Zone 3) - Non- Linear Regression. Best equation: Proposed Equation 4.9						
Empirical Model	K	B	C	Average α	N	R^2
USBM	1.08	------	------	------	0.41	0.07
AMB-HEND	4.81	------	------	------	0.61	0.13
DAVIES	8.68	2.21		------	------	0.29
GH-DAE1	4.13	------	------	0.02	-2.41	0.31
GH-DAE2	3.12	------	------	0.01	-7.71	0.32
CMRI P.	7.91	------	0.06	------	1.00	0.06
LANG-KIHL	0.12	------	------	------	0.32	0.05
INDIAN	10.00	------	------	------	2.00	0.125
PROPSED	7.15	1.19	------	0.02	0.89	0.2230

Table 4.17: The best-fit parameters for all the empirical equations used in the prediction of WAP, WARDEN, and CAIN. WAP, WARDEN, CAIN (Zone 4) - Non- Linear Regression. Best equation: Proposed Equation 4.9						
Empirical Model	K	B	C	Average α	N	R^2
USBM	1.02	------	------	------	0.54	0.04
AMB-HEND	4.71	------	------	------	0.60	0.20
DAVIES	9.97	2.23		------	------	0.35
GH-DAE1	3.37	------	------	0.03	-2.57	0.34
GH-DAE2	3.18	------	------	0.02	-7.61	0.25
CMRI P.	7.57	------	0.07	------	1.01	0.04
LANG-KIHL	0.16	------	------	------	0.32	0.01
INDIAN	8.89	1.23	------	------	1.79	0.40
PROPOSED	7.17	3.23	------	0.03	2.15	0.41

Table 4.18: The best-fit parameters for all the empirical equations used in the prediction of SCHNEIDER, WHITE and MARTIN receivers. SCHNEIDER ,WHITE and MARTIN(Zone 6) - Non- Linear Regression. Best equation: Proposed Equation 4.9						
Empirical Model	K	B	C	Average α	N	R^2
USBM	1.04	------	------	------	0.46	0.09
AMB-HEND	4.42	------	------	------	0.60	0.10
DAVIES	9.97	2.43		------	------	0.37
GH-DAE1	3.26	------	------	0.03	-2.57	0.51
GH-DAE2	3.26	------	------	0.01	-7.71	0.38
CMRI P.	7.40	------	0.02	------	1.00	0.07
LANG-KIHL	0.12	------	------	------	0.28	0.01
INDIAN	3.26	------	------	------	5.20	0.42
PROPOSED	5.72	1.75	------	0.03	1.54	0.53

Model Comparisons

To demonstrate the performance of the semi-empirical equations coefficient of determination (R^2) is taken as the performance measure. R^2 is the fundamental output of the regression analysis that shows how well the dependent variable is predicted or to what extent the assumed model is able to reproduce the data. Mathematically R^2 is the square of the coefficient of correlation (r) between the actual and predicted values. It ranges from

0 to 1. R^2 of 1 indicate that the dependent variable can be reproduced without any error. R^2 of 0.5 indicates that only 50% percent of the variance in the actual data can be predicted by the model. In this thesis, coefficient of determination will be referred by correlation factor.

Based on several studies in the literature and considering the geological complexity of the study area a correlation factor of "0.4" is found to be a reasonable threshold limit of a successful semi-empirical formula. Consequently, after attempting several trials at each of the above-mentioned 22 receiver locations, the results of the non-linear regression showed particular success for two of the empirical equations, namely the proposed and the Indian. These equations were capable of predicting the PPV values for 8 different receivers (Figure 4.35) located in zones 1,2, 4, 5, and 6 with correlation factor higher than 0.4. However, data scattering is still present which decreases the correlation at most of the other receivers and limited the average R^2 to 0.5. In some cases, no empirical model successfully matched the field data (i.e. the correlation factors were found to be less than 0.4). Among all of the empirical methods, the best equation was the proposed Eq.4.9 which produced the best fit of the PPV values with the highest correlation factors for five receiver locations. The Indian standard Equation 4.5 was not a reasonable choice for PPV prediction. However, it is considered a good predictor when compared to the other empirical equations, as it fitted the measured PPV with highest correlation factors at three of the receivers (Figure 4.36). Figures 4.37 to 4.46 show 10 examples of prediction attenuation plots of PPV versus scaled distance, using either the Indian Equation 4.5 or

the proposed formulae (4.9). Each figure represents a single main receiver/location (i.e. a receiver with large number of Vibra-Tech reports) from each of the six zones.

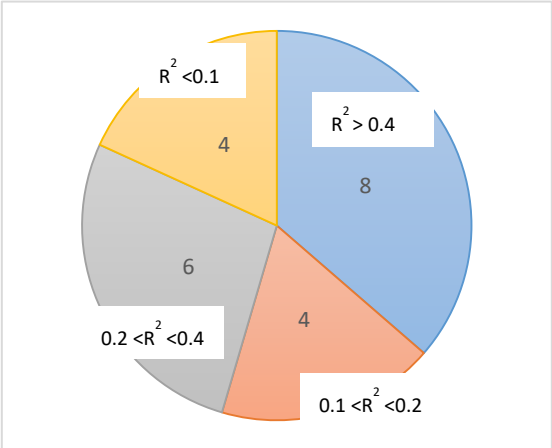

Figure 4.35 Total successful predictions by all the semi-empirical equations tested in the first phase.

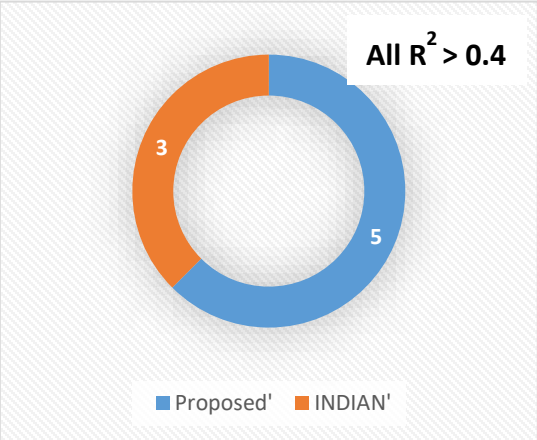

Figure 4.36: Successful predictions according to the best semi-empirical equations tested in the first phase.

Figures 4.38 and 4.40 show example of unsuccessful predictions at the Traverse and MILDA receivers with correlation factors of 0.225 and 0.3, respectively. The other eight plots successfully predict PPV with correlation factors higher than 0.4. In addition, figures 4.48 to 4.50 show the multiple-receiver prediction plots of PPV measured within zones 3, 4 and 6.

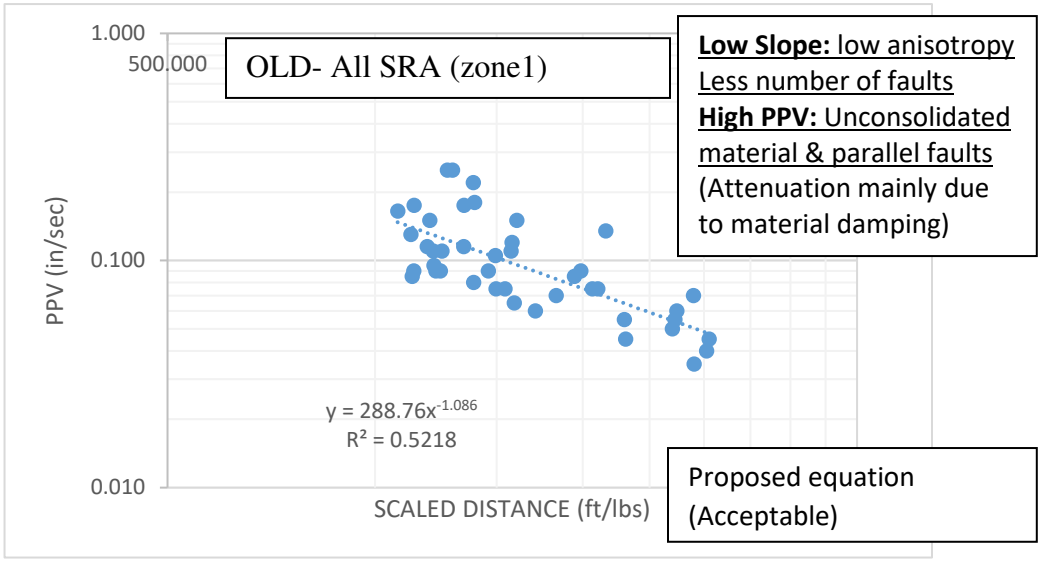

Figure 4.37: PPV vs. the scaled distance at OLD receiver location (Zone-1). Blue dots represent the measured PPV from all SRA. Blue dashed line represent the best-fit line.

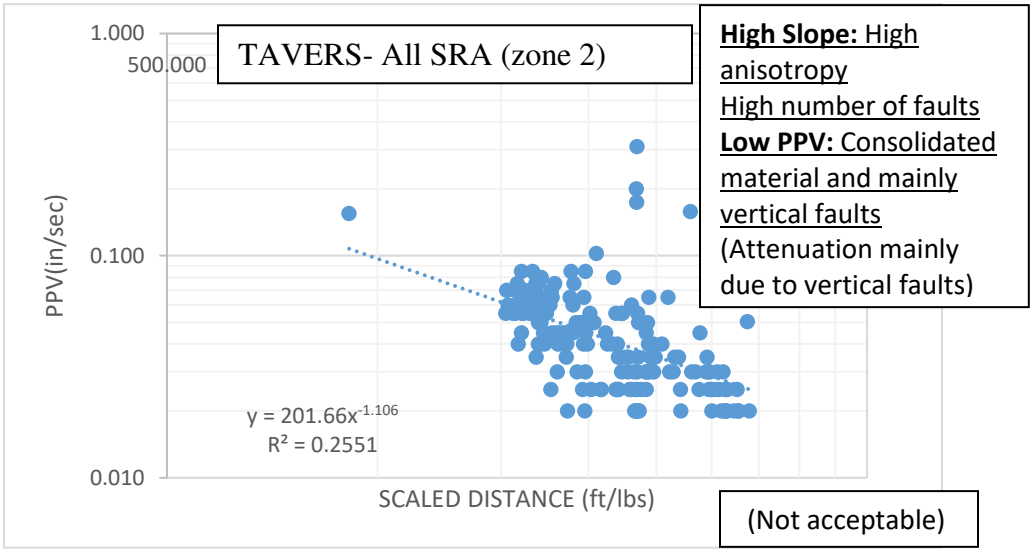

Figure 4.38: PPV vs. the scaled distance at TAVERS location (Zone-2). Blue dots represent the measured PPV from all SRA. Blue dashed line represent the best fit.

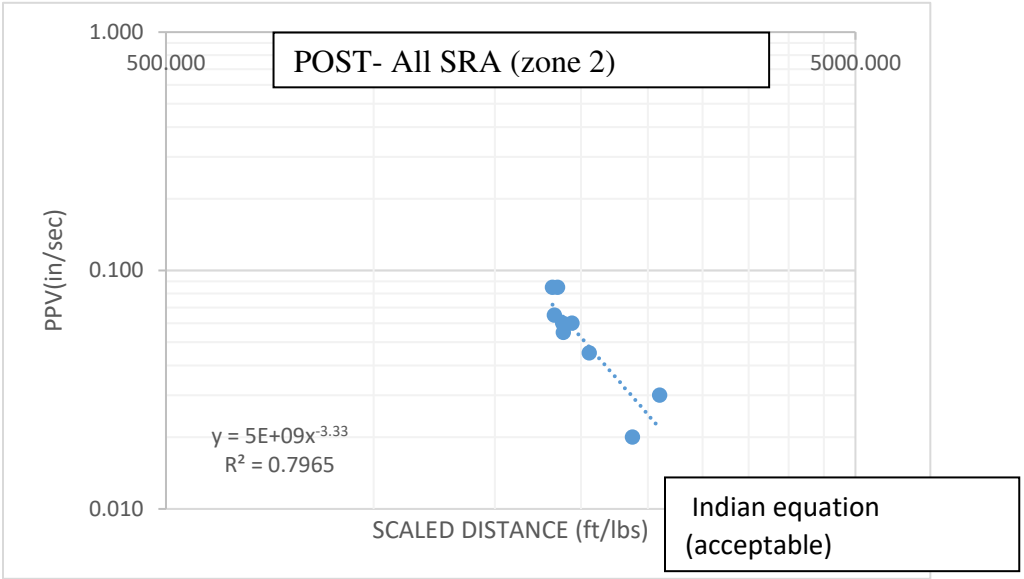

Figure 4.39: PPV vs. the scaled distance at POST location (Zone-2). Blue dots represent the measured PPV from all SRA. Blue dashed line represent the best fit.

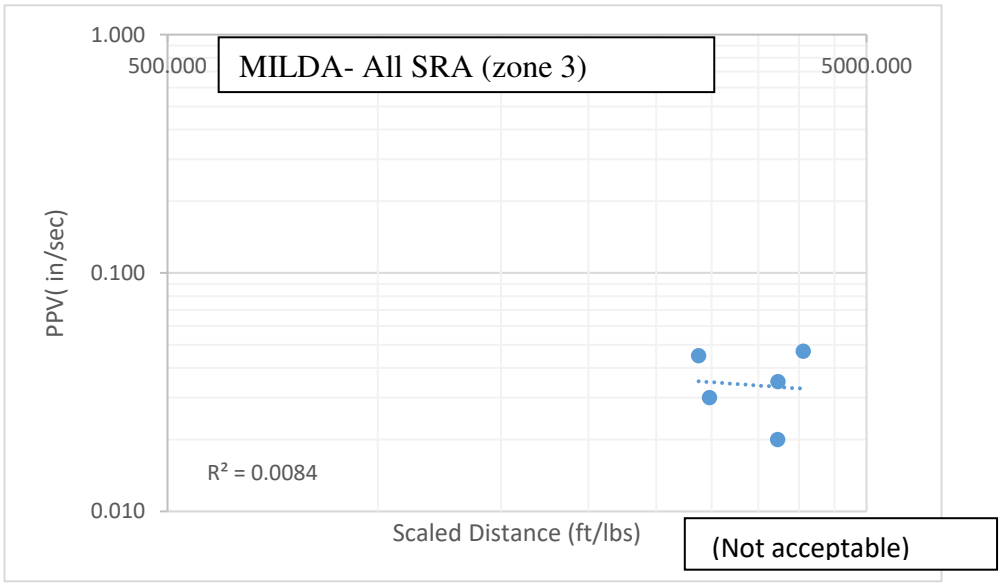

Figure 4.40: PPV vs. the scaled distance at MILDA location (Zone-3). Blue dots represent the measured PPV from all SRA. Blue dashed line represents the best fit.

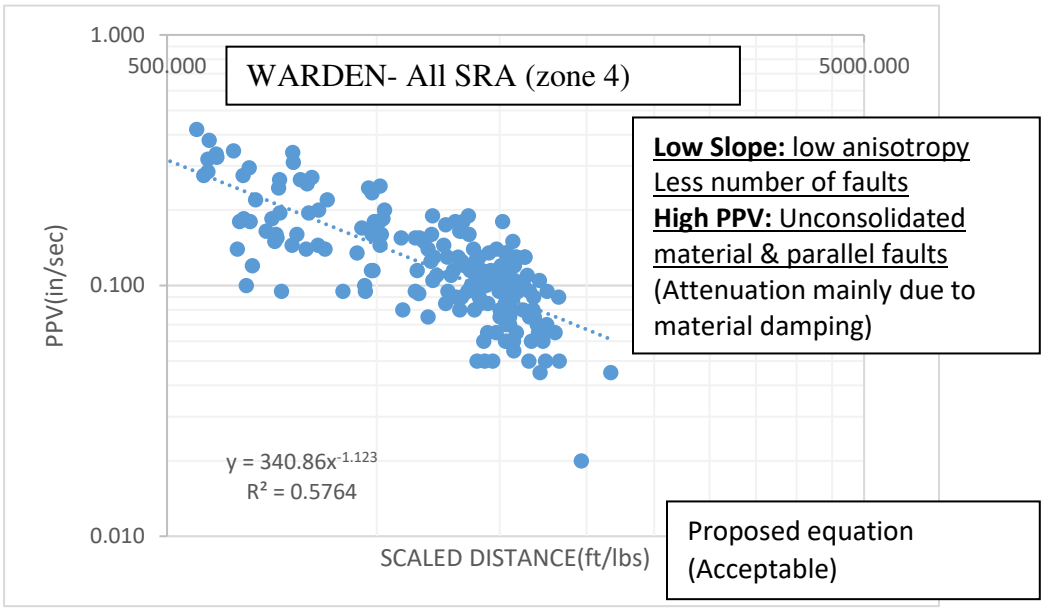

Figure 4.41: PPV vs. the scaled distance at WARDEN location (Zone-4). Blue dots represent the measured PPV from all SRA. Blue dashed line represents the best fit.

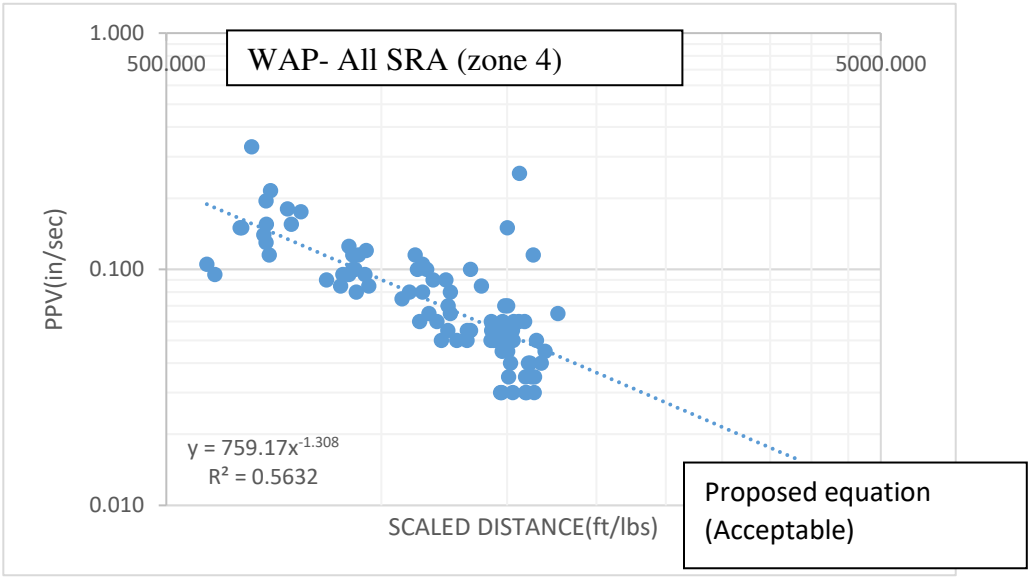

Figure 4.42: PPV vs. the scaled distance at WAP location (Zone-4). Blue dots represent the measured PPV from all SRA Blue dashed line represents the best fit.

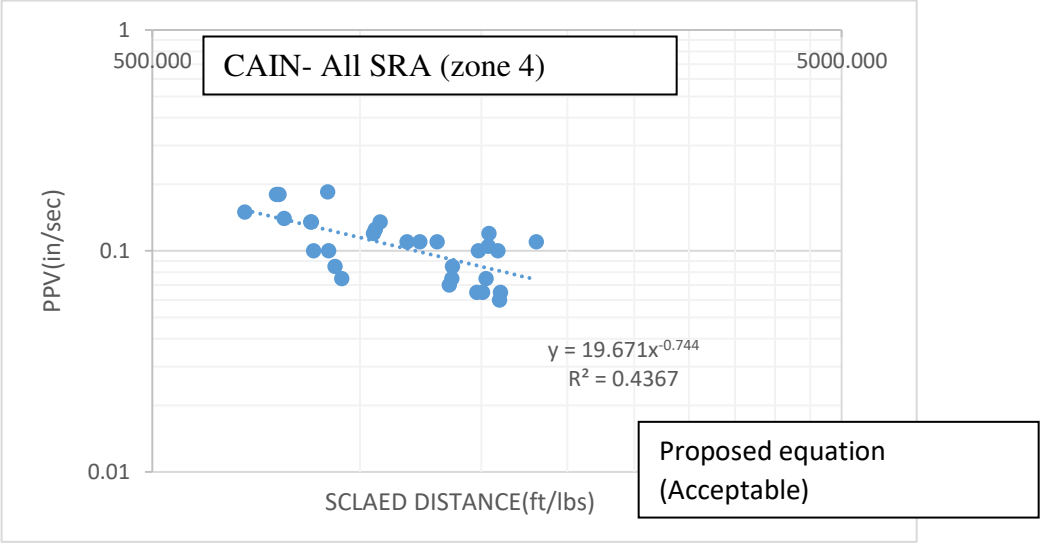

Figure 4.43: PPV vs. the scaled distance at CAIN location (Zone-4). Blue dots represent the measured PPV from all SRA. Blue dashed line represents the best fit.

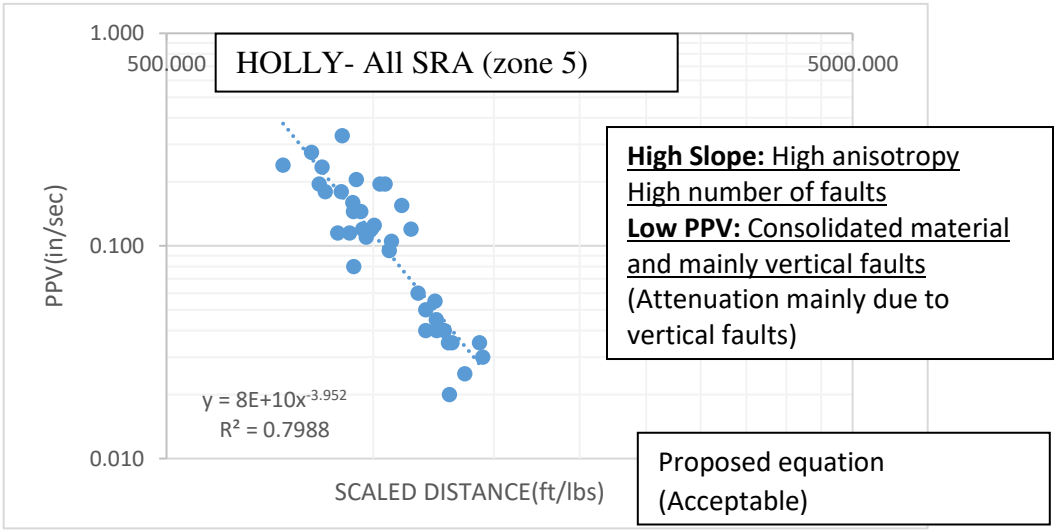

Figure 4.44: PPV vs. the scaled distance at HOLLY location (Zone-5). Blue dots represent the measured PPV from all SRA. Blue dashed line represents the best fit.

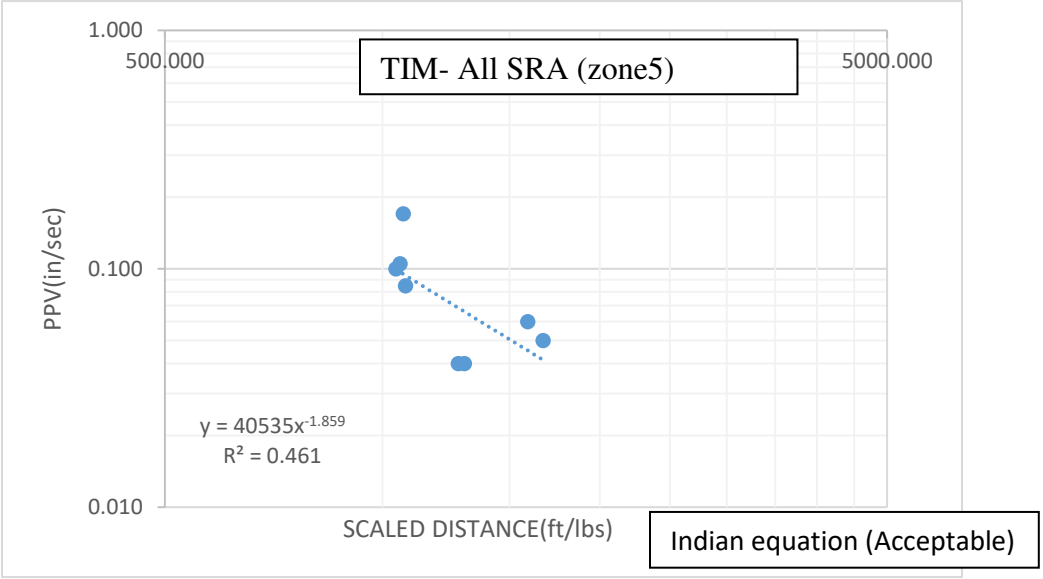

Figure 4.45: PPV vs. the scaled distance at TIM location (Zone-5). Blue dots represent the measured PPV from all SRA. Blue dashed line represents the best fit.

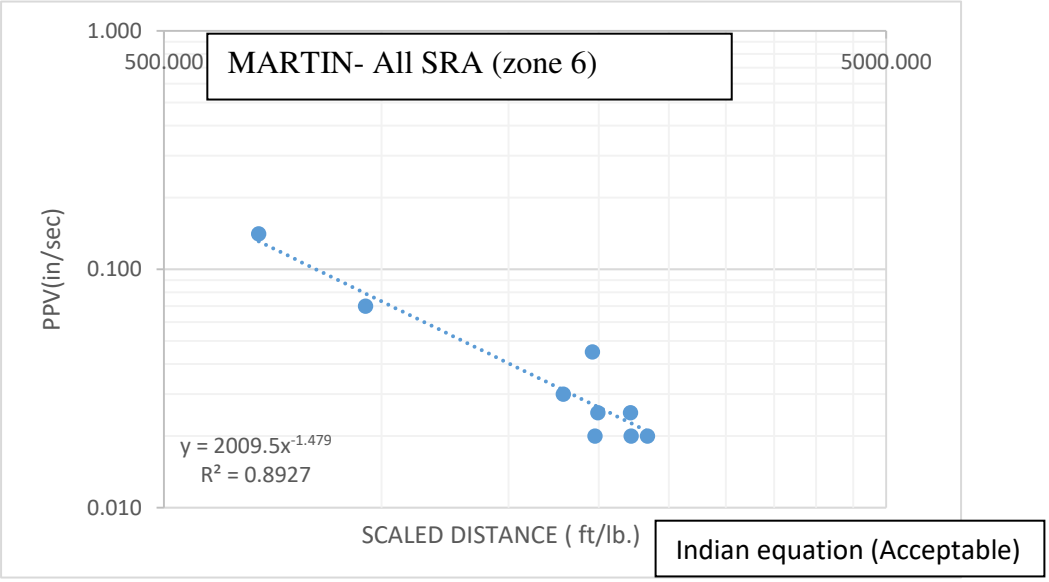

Figure 4.46: PPV vs. the scaled distance at MARTIN location (Zone-6). Blue dots represent the measured PPV from all SRA. Blue dashed line represents the best fit.

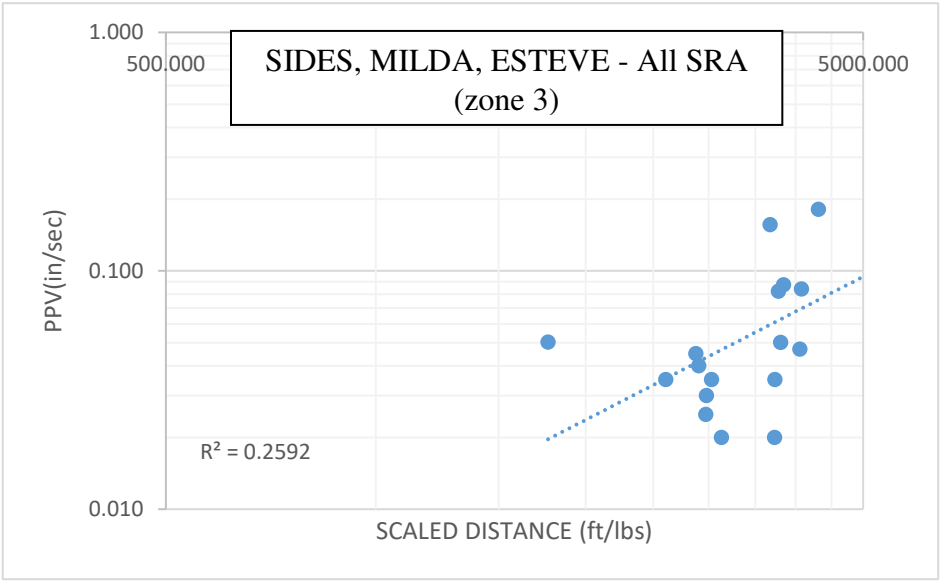

Figure 4.48: PPV vs. the scaled distance at SIDES, MILDA, and ESTEVE location (Zone-3). Blue dots represent the measured PPV from all SRA. Blue dashed line represents the best fit.

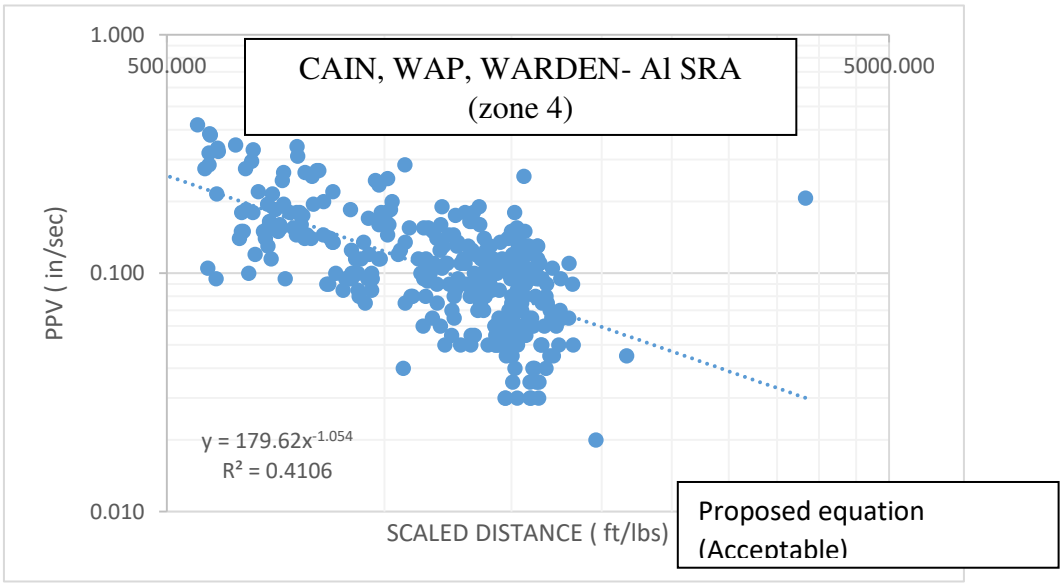

Figure 4.49: PPV vs. the scaled distance at CAIN, WAP and WARDEN location (Zone-4). Blue dots represent the measured PPV from all SRA. Blue dashed line represents the best fit.

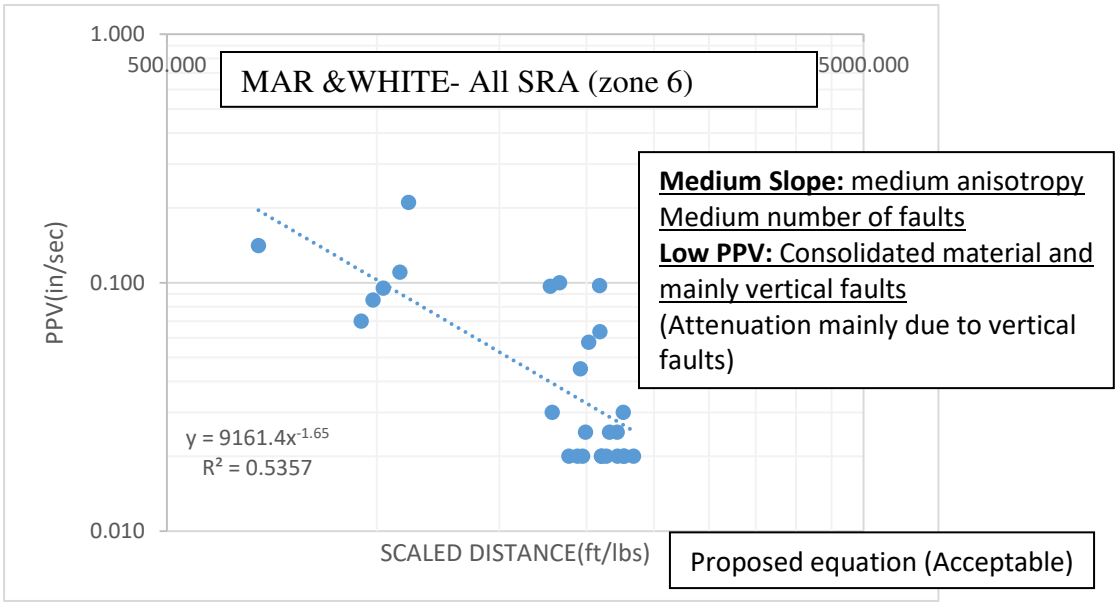

Figure 4.50: PPV vs. the scaled distance at MAR & WHITE location (Zone-6). Blue dots represent the measured PPV from all SRA. Blue dashed line represents the best fit.

Second Phase

Data Preparation

Although the zonation of the data according to the receiver locations is helpful to predict the PPV at some receiver locations, the correlation factors remain quite low for most of the data. This is an indication of the presence of complex geological structure, which can cause the empirical equation to fail to predict PPV. In this phase of the research, the scatter in the data is primarily attributed to variations in the angle between the Balcones fault trace and the travel path of the propagated wave. This supports the necessity for a second stage of analysis.

The workflow started by categorizing the PPV values measured by the 22 receivers into two groups, those with SRA parallel to fault strike and those who SRA intersects the fault strike. These groups are supposed to have the most homogenous and isotropic characteristics. In this phase the regression has been done solely on the data measured from parallel SRA. The reasoning behind this approach is to restrict the incident angle to "zero" degrees. This can be further justified as removing any interaction with the assumed faults. Consequently, using this assumption, a decrease in the data-set scattering and an acceleration in the convergence of the regression process is observed. It is worth to mention that the orientation of the major fault zones have been adjusted multiple times in order to reach higher correlation factors. The calculated correlation factors in each zone and for each receiver have been used as an indicator of the degree of geological complexity (higher correlation with semi-empirical suggests low geological heterogeneity since semi-empirical applies strictly to a homogenous medium).

Regression Results

Attenuation plots of PPV versus the scaled distance (Figures 4.53 - 4.60) demonstrate the final non-linear regression results and the best fitting-parameters. These plots can be used to determine the expected vibrations and required safety precautions. The best-fit formulae solely represent predicted PPV values of data with parallel SRA with regard to the major fault strike. The proposed, Indian Equations 4.9, and 4.5 again are the best empirical equations. They were able to predict PPV values at 12 receiver locations with a correlation factor greater than 0.4. Optimized parameters of the best-fitted equations are demonstrated for each individual receiver location. The correlation factors have been provided in order to compare the effects of the data zonation as well as to show the best empirical equation at each receiver location (Table 4.19).

Table 4.19: Summary of the correlation factor (R^2) for the modeled PPV in the second phase (after zonation).

Empirical equation/ receiver's name	Eq.1	Eq.2	Eq.3	Eq.4	Eq.5	Eq.6	Eq.7	Eq.8	Eq.9
CAIN	0.10	0.39	0.17	0.34	0.20	0.31	0.04	0.01	0.50
ESTEVE	0.21	0.04	0.01	0.19	0.01	0.25	0.27	0.25	0.24
HOLLY	0.19	0.07	0.10	0.14	0.05	0.34	0.02	0.29	0.80
KLE	0.31	0.38	0.39	0.03	0.31	0.05	0.11	0.31	0.31
LEE	0.09	0.13	0.01	0.27	0.29	0.13	0.16	0.09	0.10
MAR	0.08	0.09	0.17	0.23	0.12	0.34	0.25	0.9001	0.39
MICHELL	0.13	0.27	0.04	0.15	0.17	0.31	0.07	0.19	0.16
MILDA	0.21	0.31	0.39	0.09	0.04	0.05	0.01	0.02	0.07
MILLS	0.17	0.29	0.15	0.19	0.10	0.03	0.33	0.24	0.32
OLD	0.38	0.03	0.06	0.18	0.20	0.09	0.02	0.01	0.62
WOOD	0.28	0.01	0.34	0.15	0.13	0.13	0.33	0.09	0.45
POST	0.37	0.20	0.30	0.17	0.20	0.20	0.27	0.8321	0.25
SCHNIDER	0.18	0.01	0.29	0.13	0.03	0.03	0.08	0.15	0.13
SIDES	0.18	0.10	0.08	0.02	0.12	0.12	0.14	0.04	0.02
SMALL	0.32	0.10	0.35	0.20	0.31	0.31	0.32	0.20	0.33
TAVERS	0.33	0.31	0.31	0.38	0.06	0.22	0.23	0.23	0.50
THOMAS	0.15	0.21	0.16	0.24	0.22	0.01	0.06	0.16	0.56
TIM	0.14	0.23	0.12	0.14	0.16	0.17	0.15	0.73	0.34
WAP	0.36	0.14	0.32	0.15	0.11	0.35	0.34	0.21	0.51
WARDEN	0.27	0.25	0.22	0.34	0.06	0.16	0.11	0.22	0.63
WHITE	0.23	0.31	0.21	0.07	0.17	0.01	0.02	0.15	0.62
WINK	0.18	0.15	0.29	0.13	0.12	0.11	0.13	0.16	0.11

Model Comparisons

After removing the fault-intersecting azimuths from all the data, a widespread increase in the correlation factors was observed. The number of successful predictions (correlation factors above 0.4) is raised to 12 receiver locations in comparison to the eight receivers found in the previous section when all SRA were considered (Figure 4.51). The proposed Equation 4.9 remains the most successful in explaining PPV at most of the locations (Figure 4.52). In addition, the results verified that the non-linear regression method was capable of optimizing the parameters and providing acceptable correlations. Figures 4.53 to 4.60 show examples of the improved attenuation plots of the PPV using either the Indian (4.5) or proposed Equation 4.9. Likewise, in some zones (see Fig 4.60) multiple receivers were collectively tested. The figures shown below also demonstrated possible geological interpretations based on the estimated parameters.

Moreover, the effect on the PPV of different SRA with respect to the major faults is illustrated by plotting PPV values versus incident angle. An example of these plots is provided below in Figure 4.61 for the data measured by CAIN receiver. Seismic waves Measured by CAIN receiver have SRA intersected the fourth major fault, as shown in Figure 4.62. It should finally be mentioned that the empirical constants are specific for each receiver location and are not applicable to one another.

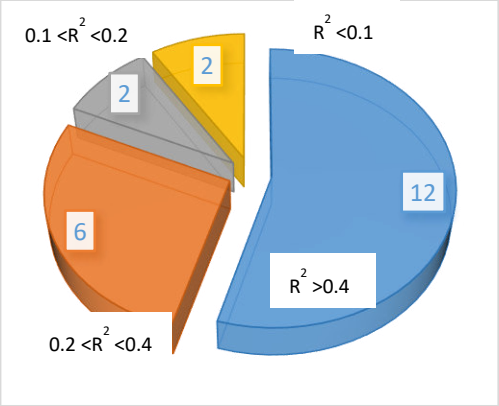

Figure 4.51: Total successful predictions by all the semi-empirical equations tested in the second phase.

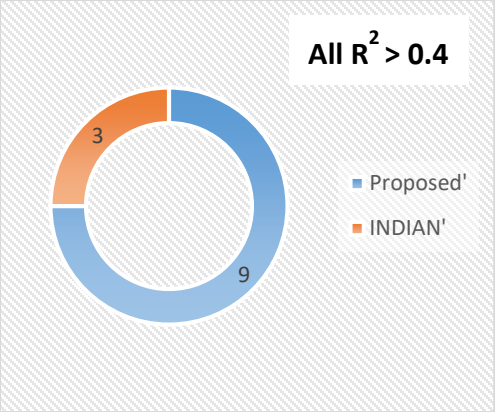

Figure 4.52: Successful predictions according to the best semi-empirical equations tested in the second phase.

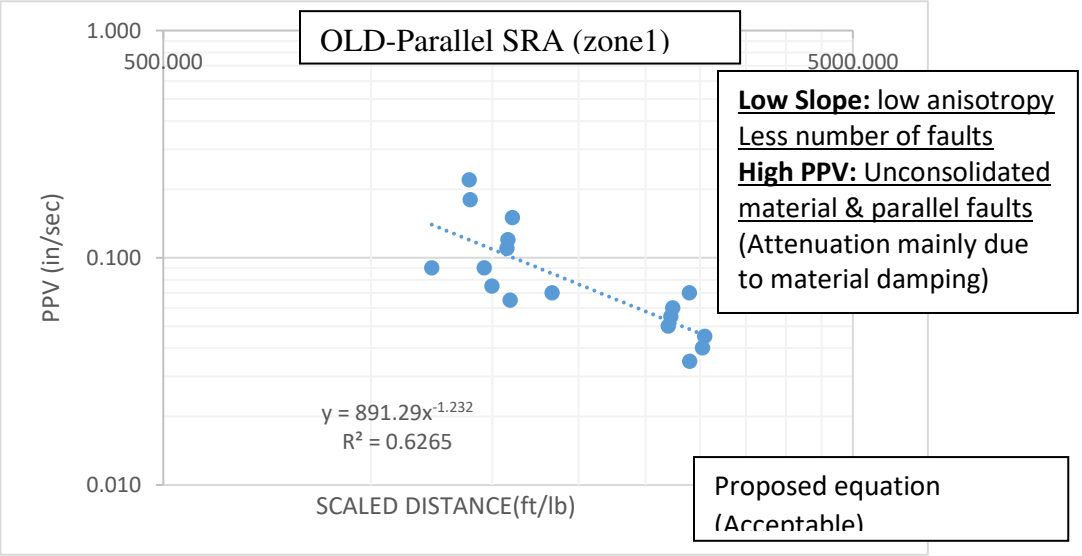

Figure 4.53: PPV vs. the scaled distance at OLD location (Zone-1)-Parallel travel paths.

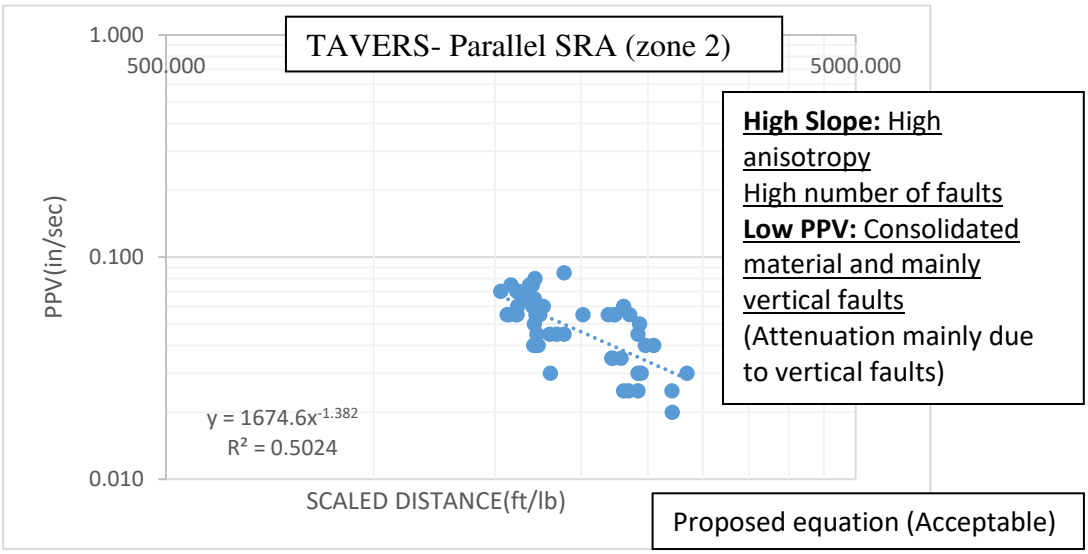

Figure 4.54: PPV vs. the scaled distance at TRAVERS location (Zone-2)-Parallel travel paths.

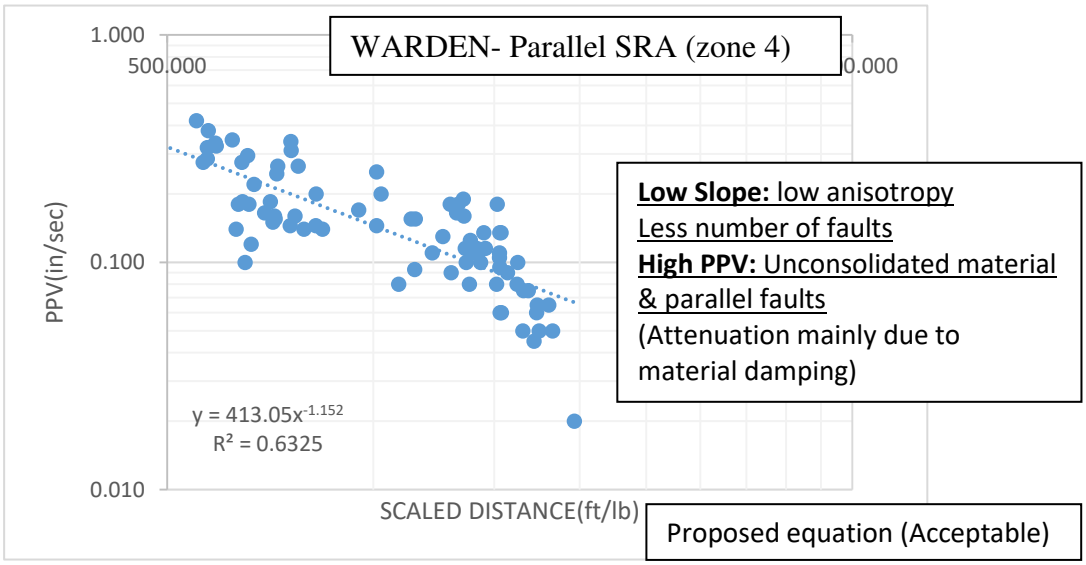

Figure 4.55: PPV vs. the scaled distance at WARDEN location (Zone-4)-Parallel travel paths.

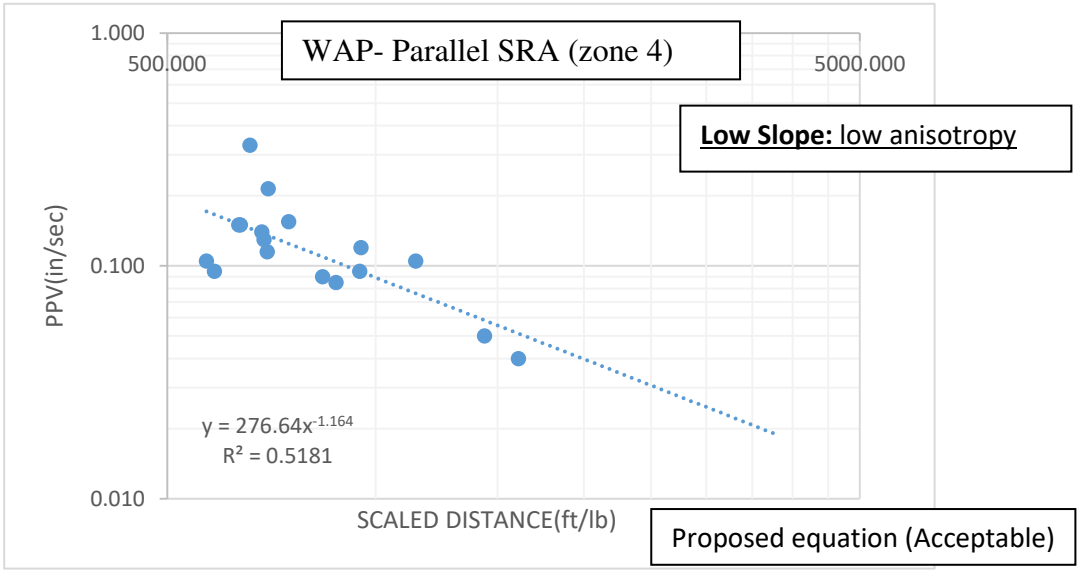

Figure 4.56: PPV vs. the scaled distance at WAP location (Zone-4)-Parallel travel paths.

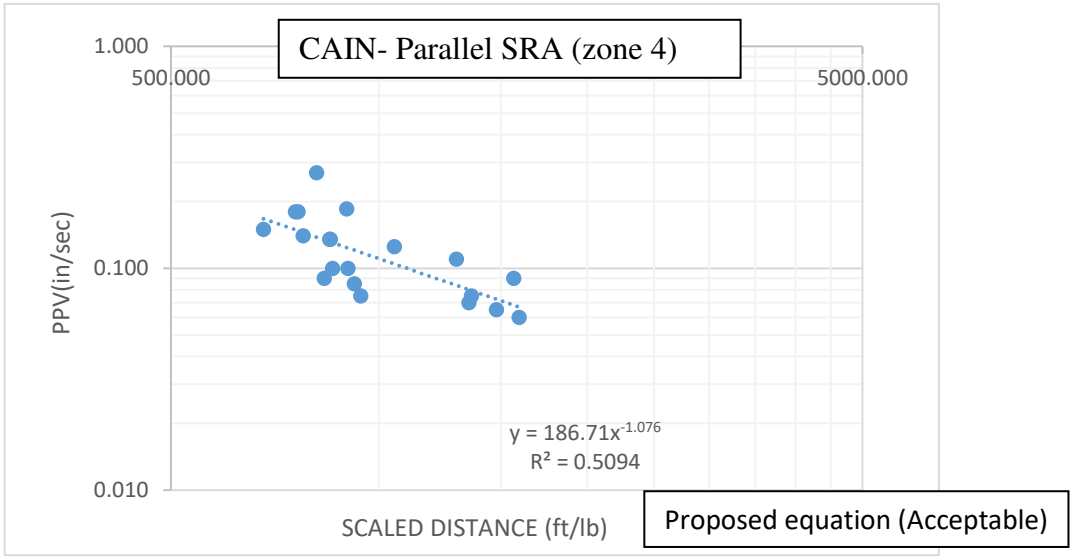

Figure 4.57: PPV vs. the scaled distance at CAIN location (Zone-4)-Parallel travel paths.

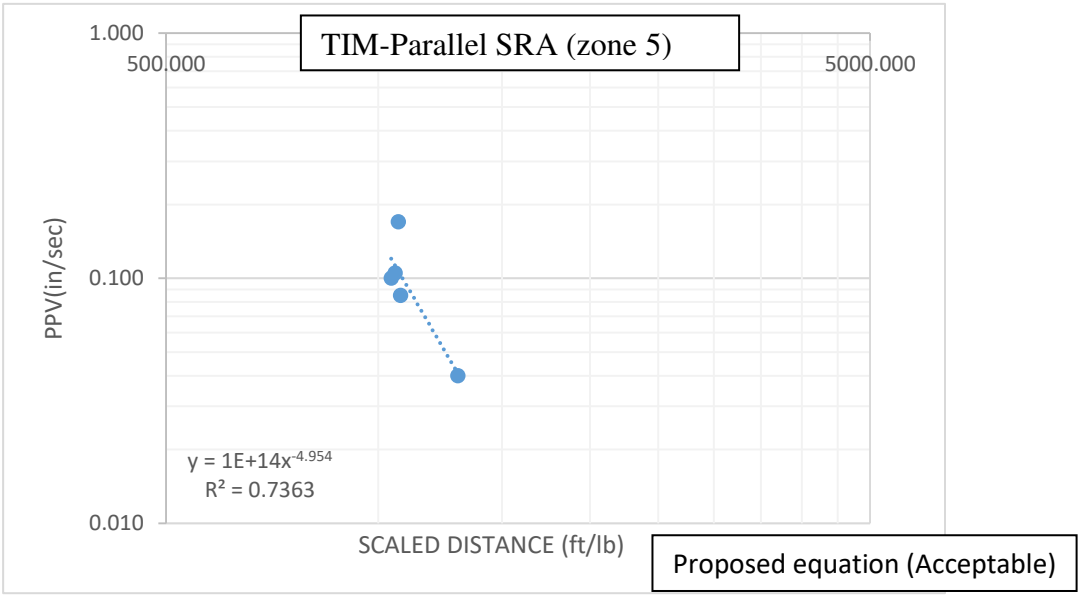

Figure 4.58: PPV vs. the scaled distance at TIM location (Zone-5)-Parallel travel paths.

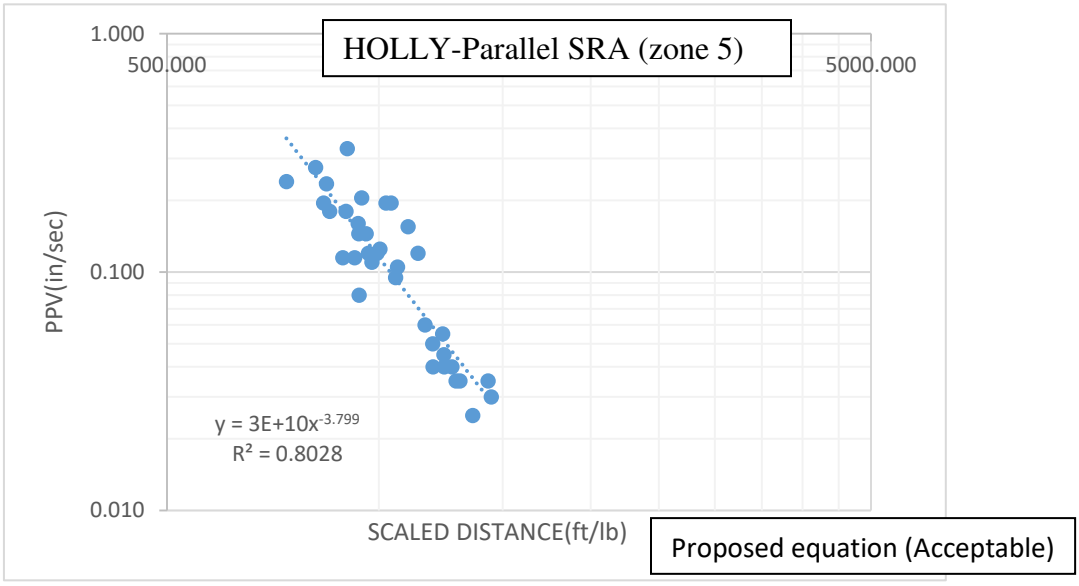

Figure 4.59: PPV vs. the scaled distance at HOLLY location (Zone-5)-Parallel travel paths.

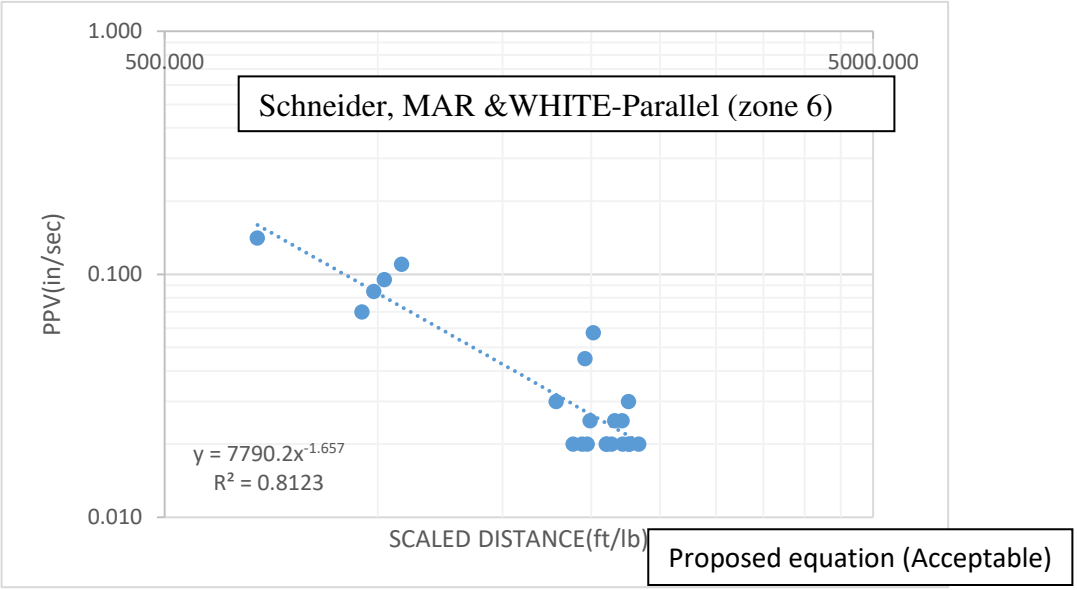

Figure 4.60: PPV vs. the scaled distance at Schneider, MAR & WHITE location (Zone-6)-Parallel travel paths.

Although the proposed Equation 4.9 succeeded in predicting PPV values at a large number of receivers, low correlation factor is found at most of the receiver locations. Consequently, the proposed Equation 4.9 cannot be considered accurate enough for always predicting PPV values. This finding supports the necessity to develop efficient predictive methods such as the neural networks and numerical wave-propagation simulations. These approaches are supposed to give models that are more reliable by incorporating more geological parameters and the physics of wave propagation. The numerical simulations, in particular can capture the wave propagation more effectively in complex geology. The next two sections discuss the process of predictive model

development using neural networks and numerical simulation along with validation exercises.

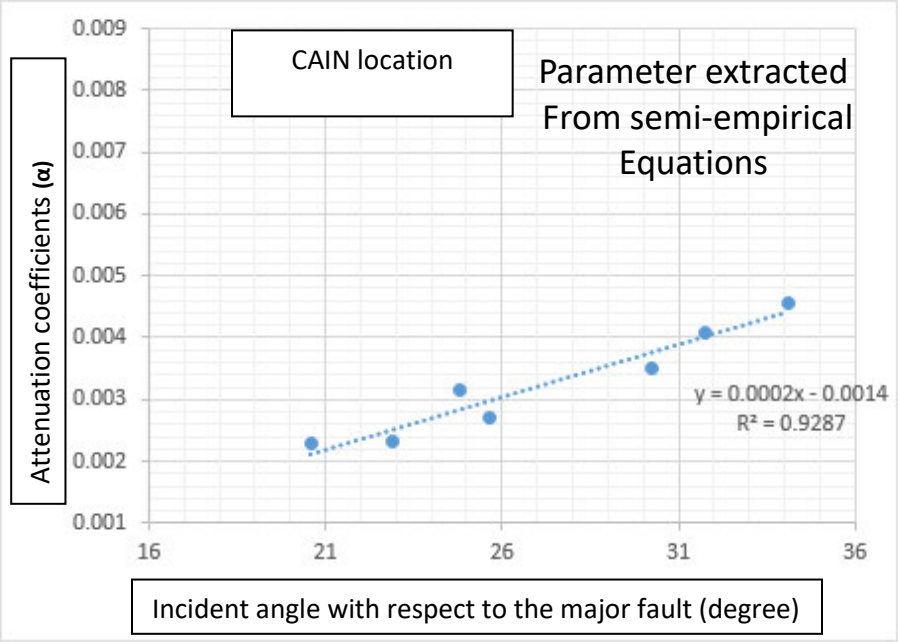

Figure 4.61: Plot of the attenuation coefficients and incident angle for CAIN receiver.

Figure 4.62: Satellite photo of the study area shows the location of measured by CAIN and the wave paths that is intersected the fourth major fault.

4.3.2 Artificial Intelligent Neural Networks

Neural networks have been utilized in many mining and environmental related problems such as prediction, pattern classification and optimization. The literature provides a number of analysis tools, which can process a large amount of information that is not easily handled by the human (Meireles et al. 2003).

In this thesis, an attempt has been made to predict PPV and dominant frequencies in the study area using Artificial Neural Networks (ANNs). The next section will discuss the process of ANN development and validation. The significance of these results for geological interpretation will also be provided.

An ANN method has been applied to the measured data at the 22 locations of the study area. Based on the results of the empirical modeling, several attempts have been made to separate the parallel ray paths from the ones that intersect with the hypothesized major faults. In this study, of many studied, two types of neural networks demonstrated the most reliable outcomes, feedforward back propagation (FFBP) and Cascade-forward back propagation (CFBP). The prediction process used significant parameters such as distance, weight of charge per delay, and likely rock properties. For each receiver location, the measured values have been divided into three categories to achieve the following ANN-related tasks: training, validation, and testing. The validation group was responsible for optimizing the weights obtained during the training, while, the testing category did not participate in the training and only used to test the capability of the networks to generalize to new data sets.

As before, the correlation factor of '0.4' is considered as the threshold for successful predictions and neural network performance. ANN succeed in predicting the PPV values of 14 receivers with correlation factor higher than 0.4.

4.3.2.1 Model Development and Data Preparation

The design and application of the ANN method is composed of the following steps:

1- Determine the input and output parameters.
2- Scale the parameters between zero and one.
3- Divide the parameters into the three categories of training, validation, and testing
4- Construct the network (i.e. specify the topology, activation function , and ranges of the parameters)
5- Run the training phase.
6- Repeat steps one to five until a higher correlation achieved.
7- Run the testing phase on a new data set.
8- Repeat steps 1 to 7 until a satisfactory model with a high correlation is reached.
9- Use the ANN model to predict the parameters using a new dataset.

The ANN topology design started by performing trials using eight network architectures. The Neural network tool in Matlab software (Demuth et al. 1993) has been used for all the tests. In each test, a different number of hidden layers and neurons are used in order to find the optimum topology. The feed forward back propagation (FFBP) and the

Cascade-forward back propagation (CFBP) architectures were successful in predicting the PPV at 14 receiver locations with correlation factor of more than 0.6. The feed forward back propagation ANN is recommended to be used, as it produced more reliable models with higher correlation. In addition to this work, the ANN method has been reported as an appropriate approach in many previous studies (Khandelwal et al. 2006) for blast vibrations prediction.

The performance of the ANN is critically affected by the data used to train the network. The input and output parameters have been scaled between zero and one before using them in the networks. The scaling was performed in order to utilize the most sensitive portion of the neuron activation function. Since the output neuron has a sigmoid activation function, it can only give output between zero and one, hence the scaling of output parameters was essential.

It worth to mention that 75% of the entire Vibra-Tech data set was used in the training and validation steps while the other 25% of data was used to test the resulting networks. Ranges of the input and output parameters have been determined by the statistical analysis of the measured data, as well as, from geological background in literature by several notable authors (Rose, 1972). The estimated rock properties represent the average values along each SRA assuming homogenous rock. Figure 4.63 shows and example of estimated rock properties along one SRA of a single blast event at TAVERS receiver. Based on the SRA and the geological map estimated value for different rock properties is determined. These rock properties include Bulk modulus, Shear modulus, Young's modulus, rock density and Passion's ratio.

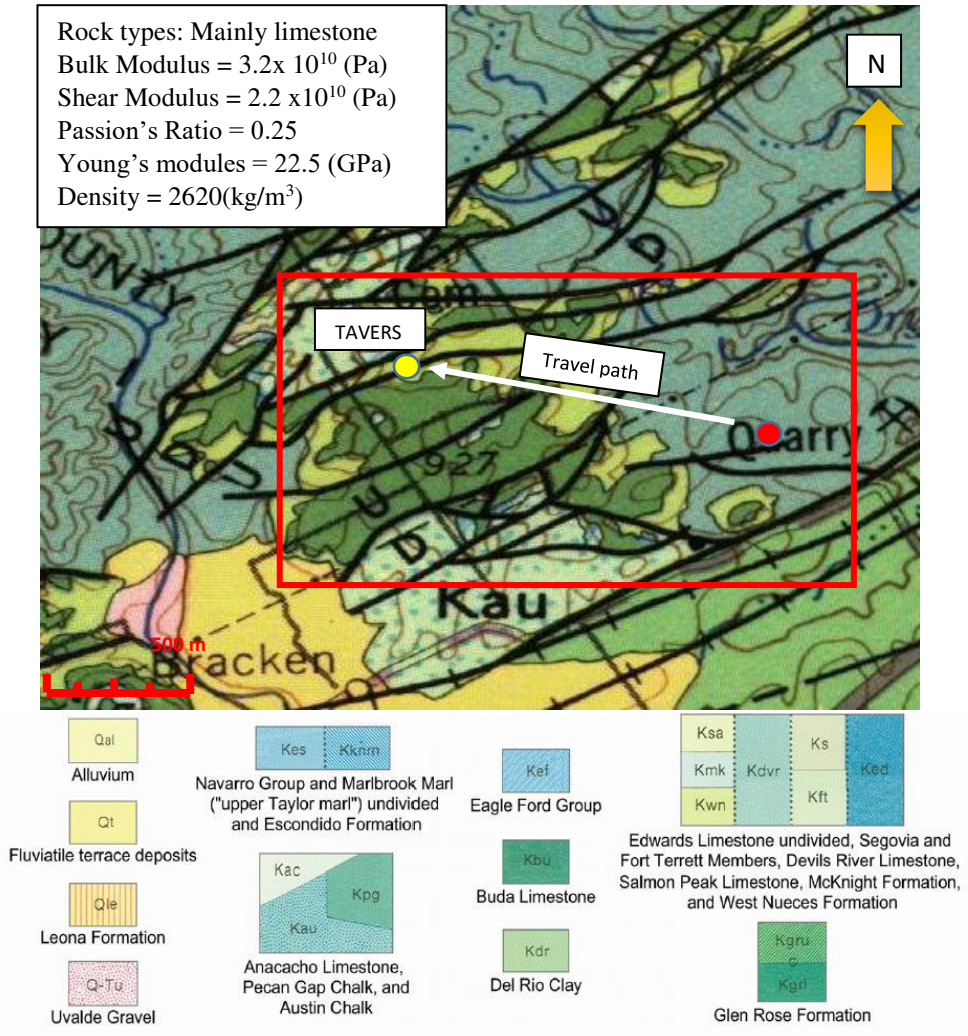

Figure 4.63: Map shows the surface distribution of different rock types in the study area (outlined by red square). Values shown represent estimated rock properties along the SRA of a single blast event measured at TAVERS receiver. Map modified from Geologic Atlas of Texas (1983).

Table 4.20: Summary of all the input and output parameters that are used in the prediction process by ANN.

Input Parameters Related to the Wave Propagation Path	Source of the input data	Output Response Parameters
Distance	Field measurement	PPV
Weight charge per delay	Field measurement	Dominant Frequency
Rock density	Estimated from Literature & geologic maps	P, S and R wave velocity
Shear Modulus	Estimated from Literature & geologic maps	Attenuation coefficients
Young's modulus	Estimated from Literature & geologic maps	
Poisson's ratio	Estimated from Literature & geologic maps	
Bulks Modulus	Estimated from Literature & geologic maps	

In this study, two types of approaches have been implemented to provide the networks with the input parameters; (1) 'two parameters' approach, (2) the 'total parameters' approach .Using the 'two parameters' approach, the ANN comprises of only two inputs, the source receiver distance and the maximum charge per delay. In the "total parameters" approach, all of the 7 parameters are used as input for the network. The target/output parameters in both cases are the PPV, dominant frequency, attenuation coefficients and propagation velocity. As indicated in Table 4.20, the scaled distance and maximum charge are taken from the Vibra-Tech event records and the rest of the parameters are taken from either literature or geological maps.

4.3.2.2 Results and Comparisons

A group of well-trained neural networks was achieved after a sequence of training applied to the input data from the 22 receiver locations. The ANN architectures (FFBP and CFBP) were able to map the relations and predict the PPV and dominant frequencies with high correlation factors above 0.4 (Figures 4.64 and 4.65). The correlation factors of the networks using the two high-certainty input parameters (distance and charge weight), are generally higher compared to the networks that utilized all of the parameters as an input. Data from 12 receiver locations have been predicted using the 'two parameters 'approach, while the 'total parameters 'approach was able to predict the PPV at only 2 receiver location (Figure 4.66). In summary, the feedforward backpropagation (FFBP) was more effective in predicting the PPV values compared to the cascade forward networks (CFBP) or any other architecture.

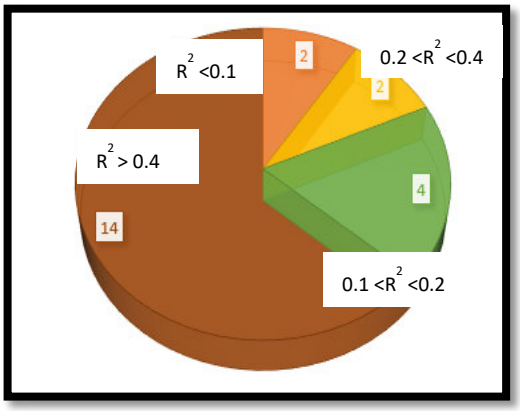

Figure 4.64: Total Successful predictions by the neural networks.

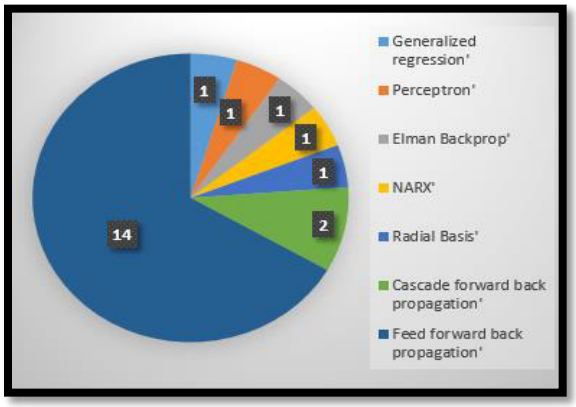

Figure 4.65: Successful predictions according to the type of neural network.

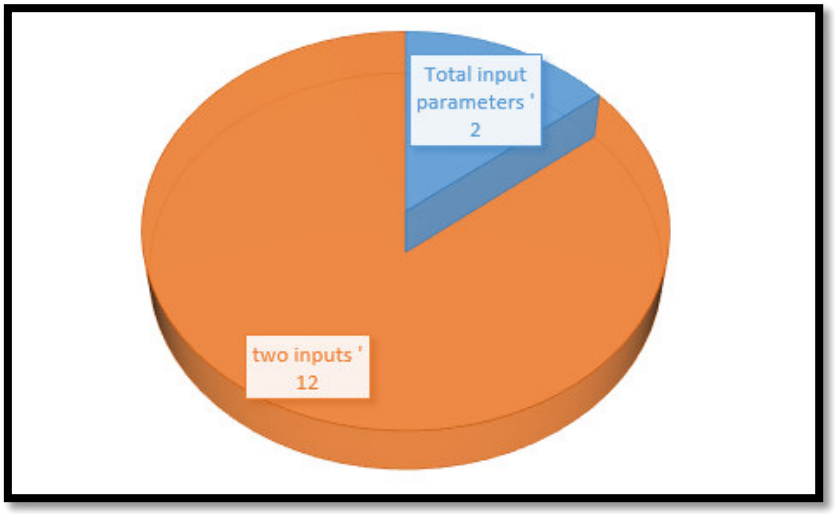

Figure 4.66: Successful predictions by neural networks according to type of input.

Table 4.21 provides examples of the architecture of the best neural networks for four receivers. A good agreement between the measured and the modelled PPV for four selected receivers is shown in Figures 4.67 to 4.70.These figures show the validity of the ANN for perdition of PPV and dominant frequencies in the study area. In the event of unsuccessful trials (R2 <0.4), the ANN approach cannot be used reliably to predict PPV. Table 4.22 shows the best network designs and their performance for all 22 receivers in the six zones.

Table 4.21: Summary of the final network design and their performance for four receivers in zones 1, 2, 4, and 5.

Parameters/ Designs	HOLLY- R.	WARDEN-R	OLD- R.	TAVERS-R
Network type	Feedforward Back Propagation (FFBP)	Cascade-forward Back Propagation (CFBP)	Feedforward Back Propagation (FFBP)	Feedforward Back Propagation (FFBP)
Training algorithm	Levenberg-Marquardt	Levenberg-Marquardt	Levenberg-Marquardt	Levenberg-Marquardt
No. of layers	2	2	2	3
Two Input Parameters	Weight per delay Distance	Weight per delay Distance	Weight per delay Distance	Weight per delay Distance
Target parameters	PPV	PPV	PPV	PPV Dominant frequency
No. of neurons at the hidden layer 1	7	7	5	5
Best Epoch	2	10	20	5
Activation function	LOGSIG	TRANSIG	TRANSIG	LOGSIG
Total Time	8 Epochs 0:00:01	40 Epochs 0:00:01	11 Epochs 0.:00:05	17 0:00:05
R^2 Correlation factor	0.86	0.74	0.84	0.74
Data Division	Random	Random	Random	Random

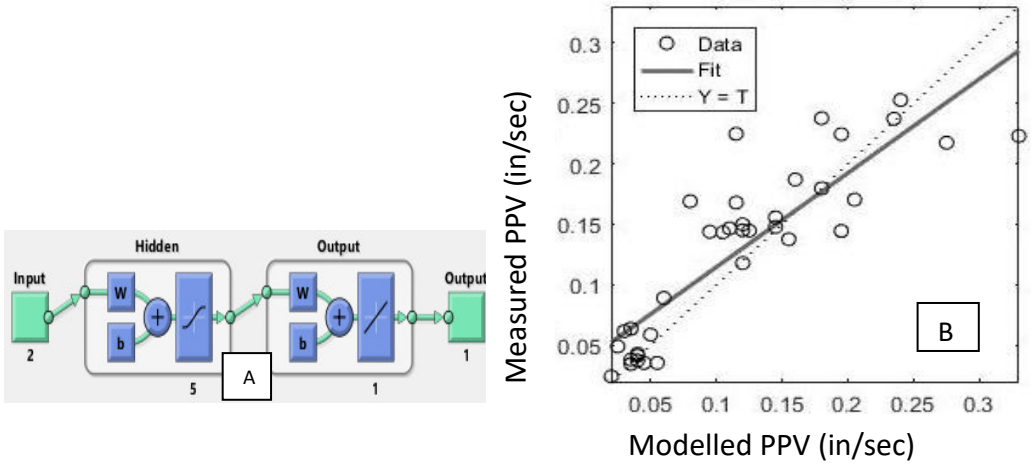

Figure 4.67: A) Topology of the Feedforward back propagation neural network used for HOLLY location. B) Correlation plot of the measured and predicted PPV.

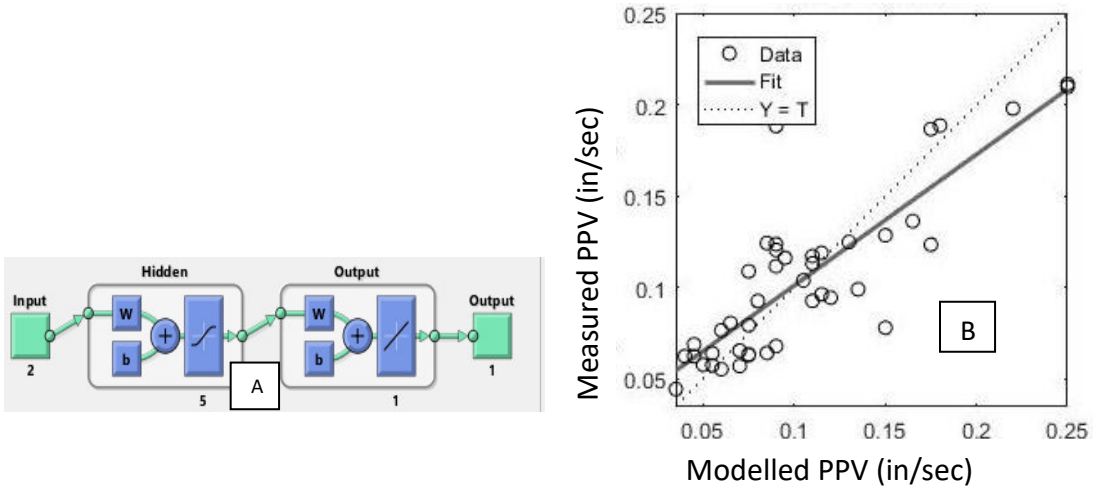

Figure 4.68: A) Topology of the Feedforward back propagation neural network used for OLD location. B) Correlation plot of the measured and predicted PPV.

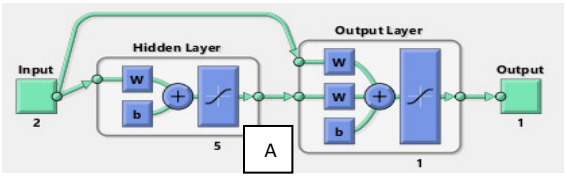

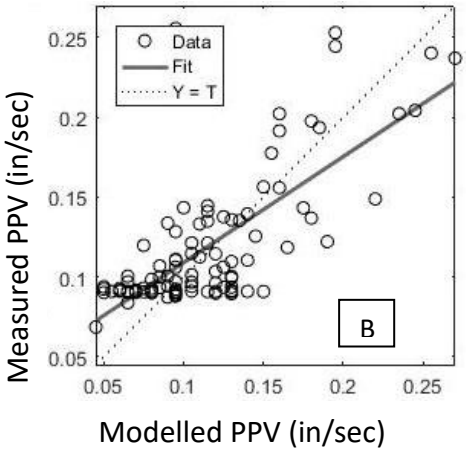

Figure 4.69: A) Topology of the Cascade forward back propagation neural network used for WARDEN location. B) Correlation plot of the measured and predicted PPV.

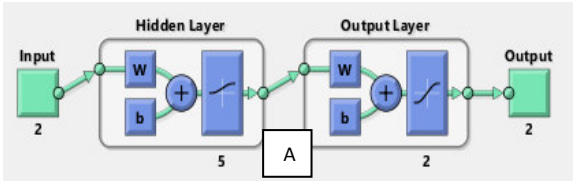

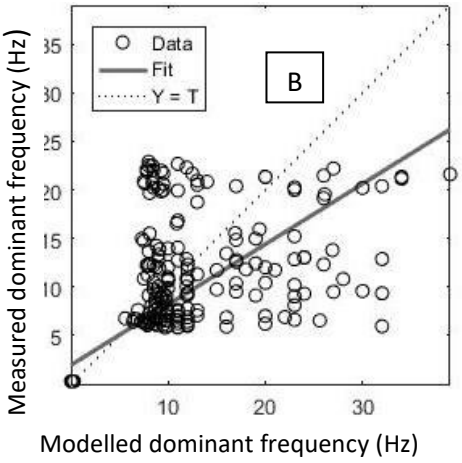

Figure 4.70: A) Topology of the Feedforward back propagation neural network used for TAVERS location. B) Correlation plot of the measured and predicted dominant frequencies.

Table 4.22: Final artificial neural network design for all the 22 receivers.

Empirical equation/ receiver's name	Network type	No. of neurons at the hidden layer 1	No. of layers
CAIN	FFBP	5	3
ESTEVE	CFBP	5	3
HOLLY	FFBP	5	3
KLE	FFBP	7	4
LEE	FFBP	5	2
MAR	FFBP	5	3
MICHELL	CFBP	7	4
MILDA	CFBP	5	3
MILLS	FFBP	5	4
OLD	FFBP	7	2
WOOD	CFBP	7	2
POST	FFBP	5	2
SCHNIEDER	FFBP	5	2
SIDES	CFBP	7	2
SMALL	FFBP	5	2
TAVERS	CFBP	5	3
THOMAS	FFBP	5	4
TIM	FFBP	7	2
WAP	CFBP	7	2
WARDEN	FFBP	5	2
WHITE	CFBP	5	2
WINK	FFBP	7	3

The results obtained from the ANN were compared to that of the empirical equations (Figure 4.71). In general, the neural network approach shows an improvement in the correlation factor and a better ability to predict the PPV and dominant frequency. However, a low correlation factors below 0.4 have been obtained from eight receivers, which could be caused by either geological heterogeneity of the study rea or lower accuracy of input data.

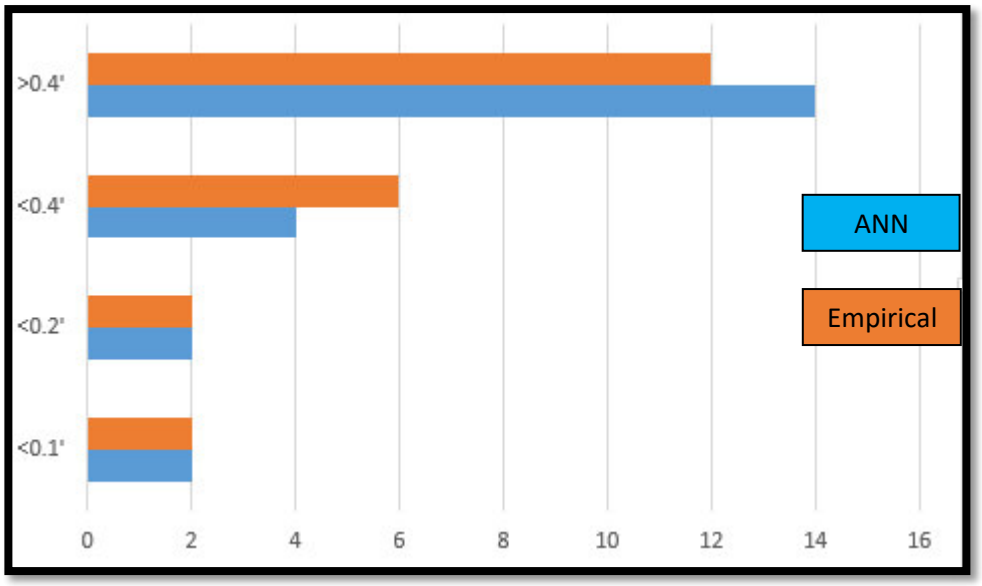

Figure 4.71: Comparison between the empirical and the ANN Results.

4.3.3 Finite Element Analysis

The next level of complexity in the analysis of PPV and dominant frequency from the Garden Ridge quarry blast investigation is to create a numerical model that can evaluate wave propagation through different geological structures within the study area. In this thesis, it is argued that the PPV values are controlled by five wave propagation mechanisms, as earlier mentioned in the conceptual model. The objective here is to analyze the application of these mechanisms within the study area geometries and to demonstrate them utilizing a 3D numerical simulation.

Various numerical methods have been used in the geophysical literature to simulate seismic wave propagation. Examples of these approaches are the spectral element, the boundary element, the finite difference, the finite element and the finite volume methods (Semblat and Pecker, 2009). In this thesis, to describe the propagation of seismic waves due to underground blasting, a finite element method has been employed. The wave propagation modelling process has been simulated using two commercial software packages, COMSOL and GTS-NX.

The current study assumes that the rock mass and soil around the quarry have an elastic behavior. In addition, the cracked and flying rocks due to blasting are considered to be very small volumes, so that they can be omitted. The simulations are energy conserving, thus the energy generated by the blasting source can be decomposed into a fracturing energy of the rock mass near the source, and radiating energy propagated in the elastic medium. It is the latter that responsible for the annoyance to residents in the surroundings.

Parameters of the numerical models have been adjusted iteratively in order to reach a good agreement between the predicted PPV values and the available field data. Elastic and visco-elastic properties have been used for materials models in order to predict their behavior under stress. The numerical approach succeeded to predict the PPV at four receiver locations with an acceptable correlation. In the event of the unsuccessful predictions of 18 receiver locations, the geology is considered more complex that require additional sophisticated data.

4.3.3.1 Model Development

Domain Geometry

An attempt has been made to construct a modeling domain, which has the same dimensions as the study site. The geometry of the finite element domain adopted for all simulations is shown in Figure 4.72. This figure illustrates the model specification of one blasting event recorded by one receiver with no faults intersecting the wave propagation. Figure 4.73 shows an example of a domain that includes several internal faults. Moreover, for each of the different simulations, the width has been adjusted to a range of 50- 100 m with a shallow domain depth ranging between 10-20 m. Length of the domains is determined based on the source-receiver distance. The points of measurements i.e. the receivers have been arranged on the domain surface at the same distance. As shown in Figure 4.74 the blasting chamber is assumed to have a cubic shape with dimensions of 2x2x2 m and located at depth 2 m beneath the domain surface. All the blasting chambers were assigned to the same positions as the actual sources being modeled.

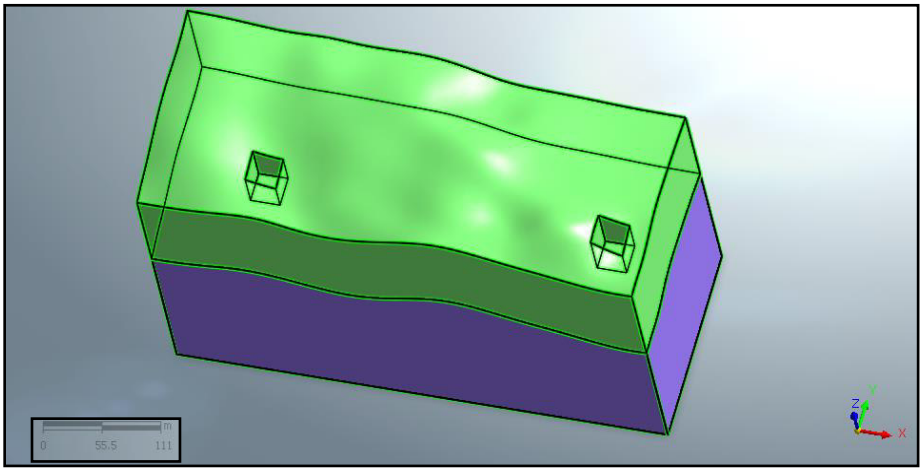

Figure 4.72: An example for the geometry that is applied in the numerical modelling of the first conceptual model. In this model, internal faults are not included.

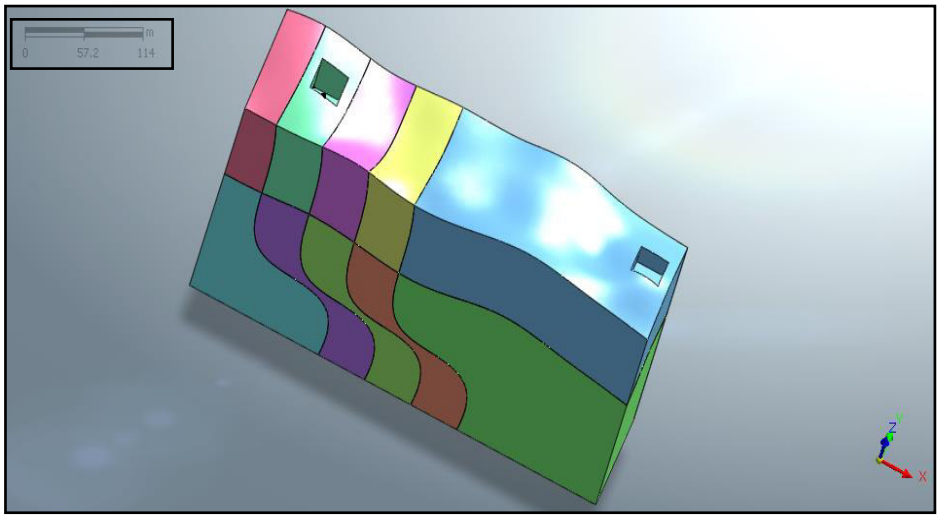

Figure 4.73: An example for the geometry that is applied in the numerical modelling of the second conceptual model. In this model, internal faults are included.

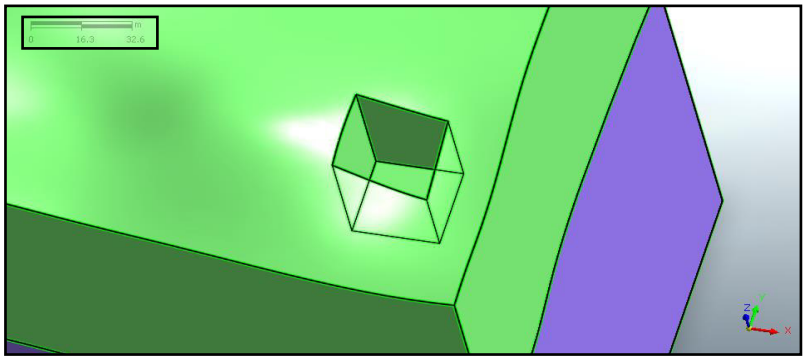

Figure 4.74: An example of the blasting box geometry that is applied in the numerical modelling of all conceptual models.

Meshing

An example of the computational meshes that are adopted in this thesis are shown in Figure 4.75. The numerical mesh shown is built with 13024 tetrahedral elements and 19585 nodes. The mesh has been refined close to the blast hole and typical size of the elements is increased outward from the blasting chamber.

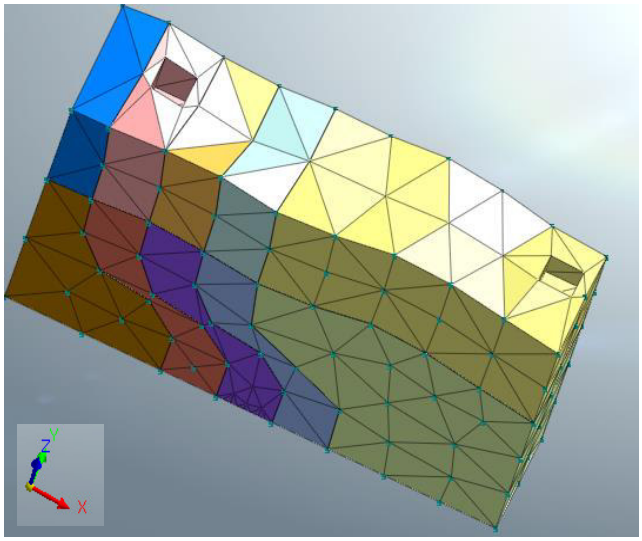

Figure 4.75: An example for the meshing that is applied in numerical modelling of the second conceptual model. In this model, colors are an indication of different mesh size.

Blast Load Function

All the charge weights specified in the Vibra-Tech even reports have been tested in this thesis. Table 4.23 summarizes the blast design parameters that are used to model wave propagation in zones 2 and 5 including blasting velocity, intensity, etc. It is worth mentioning that the blast designs described here represent typical specifications for the open pit mining industry. A pressure load function (Figure 4.76) is applied on all six inner sides of the charge chamber. The blast wave uses the standard blast-design formula (ISEE, 2000) designed by the international society of explosives engineers (ISEE).

Table 4.23: Typical blast design parameters used in the modeling stages.

Parameters	Values	Unit
Blasting Velocity(V)	9842.2	ft./sec
Explosive Density (S)	1.2	g/cm3
Charge Diameter (dc)	30	mm
Borehole Diameter (dh)	50	
Maximum Charge Amount (W or Q)	2	kg
Load Factor(B)	1633	

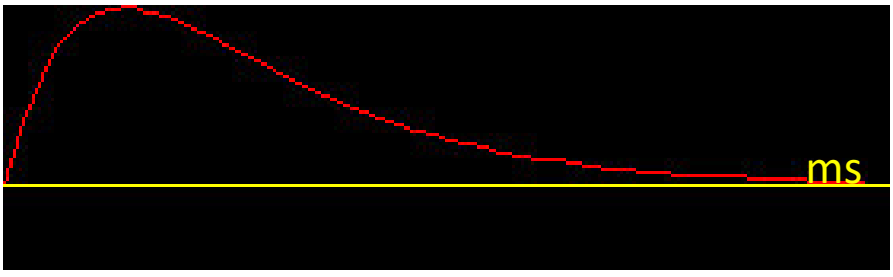

Figure 4.76: The pressure load function.

Boundary Conditions

Two types of boundaries have been used in this thesis, absorbing and non-absorbing conditions. Both transmitting and reflecting boundaries have been used during the modelling, which helps to simulate different types of discontinuities. Boundary conditions are used to reduce the artificial reflection of the elastic wave from the boundaries, which allows the outward traveling waves to pass through without returning energy back into the computational grid. Only the normal component of velocity of the wave is considered, while the velocity component parallel to the boundary is assumed to be unaffected by the boundary. In addition, the boundary conditions are used to simulate the effect of the juxtaposition of materials due to faults, which causes a high velocity contrast between the fault zone and its surroundings.

Material Model

The estimated rock mass parameters were determined based on background geology and literature data and these are summarized in Table 4.24. In order to study the effect of different geological structure on predicted PPV values, material parameters such as Poison's ratio, bulk modulus and density are adjusted during the simulation.

Table 4.24: Initial rock Parameters adopted in the numerical analysis.

Initial models	Young's modulus (GPa)	Poisson's Ratio	Density(Kg/m^3)	Uni-Axial Compressive Strength (KN/m^2)
Rock model 1	51	0.26	2720	157
Rock model 2	74	0.16	2610	186
Rock model 3	1.5	0.3	2000	160

4.3.3.2 Validation and Cumulative Results

Results of four numerical simulations of the resultant PPV measured at OLD, TAVERS, WARDEN and HOLLY locations are shown in Figures 4.77- 4.80. As defined earlier Resultant PPV is the vector sum of the measured PPV in the three directions (longitudinal, horizontal, and vertical) at the same measuring point. In these models, wave propagation along the surface of the rock, generated from blasting holes at very shallow depths, has been simulated. Stress waves propagate from the blast hole through the fractured zone into the various zones where the receivers are located. The time histories of particle velocity on the ground surface at the measuring points have been calculated. Moreover, because not all the receivers are located on the same source-receiver azimuth (SRA), the simulation has been performed as a function of scaled distance in order to detect the effect of the anisotropy and heterogeneity on seismic wave attenuation.

As mentioned previously, simulations have been done using the same amount of explosive weights as used in the field according to each blast location. In addition, the models were interchanged in its design based on the four proposed mechanisms of

propagation in the conceptual model. This variation of design was done in order to find the best matching between the modelled and the actual PPV values. As a result, the number of discontinuities, model parameters and material distributions have been adjusted several times during the modelling stages.

It is generally accepted that geological effects on wave propagation can be understood by visualizing the attenuation of stress waves with distance from the blast center. Similar to the findings related to the empirical modeling, the most relevant parameter to infer potential damage to structures is the peak particle velocity (PPV), i.e., the maximum value of the particle velocity at a given location. The PPV can be plotted versus scaled distance to accommodate the variation in distance and charge for each event.

Figures 4.77-4.80 compare the measured PPV on the Vibra-Tech event reports at four receiver locations with the results of the numerical simulation. On the horizontal axis is the scaled distance, defined as the ratio between the actual distance from the blast center, D in ft, and the 1/7 power of the equivalent TNT weight, W in lbs. The scaled distance is described in the proposed equation (Eq.4.9). By comparing the four figures, it can be concluded that the blast-induced vibrations are substantially different at the four locations.

In general, the modelling results show that the intensities of the stress wave components in the three directions (vertical ,longitudinal and horizontal) at the same measuring point differ from the actual measured values at most of the receiver locations. Occasionally the same locations that were modelled successfully by the empirical equation (Eq.4.9), also gave a good results with the numerical simulations. The successful locations are OLD, TAVERS, WARDEN and HOLLY receivers that have a correlation factor of

0.5, 0.6, 0.5 and 0.7, respectively, for the resultant PPV (Figures 4.77- 4.80). The radial component has the lowest correlation factor while relatively higher correlations were found for the horizontal and vertical components.

It is worth mentioning that the homogenous elastic-wave numerical modeling was unsuccessful in reproducing the actual seismic wave propagation for most of the receiver locations in the study area. This is illustrated by the small amount of scattering that appears in the PPV-scaled distance plots. The modelling procedures have been divided into two phases. The first modeling phase is conducted without any faults or discontinuities included in the modeling domain. The second phase incorporates the discontinuities into the model domain. In the second phase of modelling, the individual model domains have been modified by imposing a number of parallel and intersecting faults. As well, the material model type have been changed into Gen Hoek Brown model. Hoek and Brown (1980) and Hoek (1983) described a criterion for brittle rock failure. This criterion is commonly used to estimate the strength of jointed rock mass. In this phase, non-absorbing reflective boundary condition has been exploited in order to simulate the effect of the lateral lithology changes and juxtapositions of materials due to the faults.

Imposing more discontinuities positively affected the correlation factor between the modelled and the actual data. Figure 4.81 shows the actual data for OLD receiver compared to the modeling results in the first phase (i.e. no discontinuities are included). Correlation factor for the modeled PPV at OLD receiver in the first phase is 0.3 while in the second phase it has a value of 0.5. Another example of the modeled PPV in the first phase is shown in Figure 4.82 for HOLLY receiver with a correlation factor of 0.1. As

well, the three-velocity components of the four numerical models showed relatively higher correlation factors compared to the first phase.

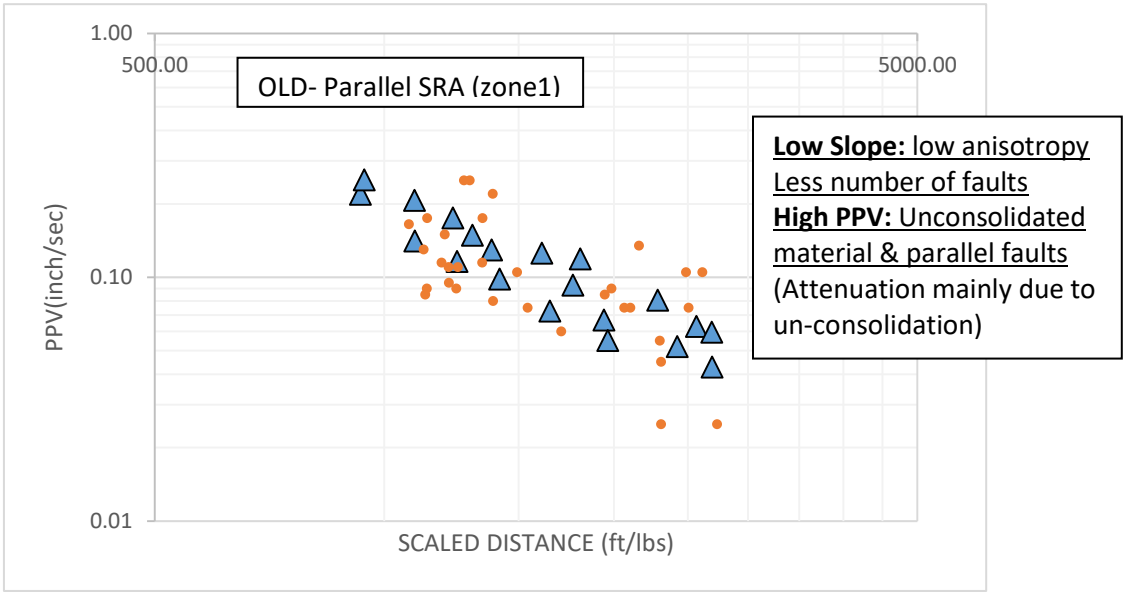

Figure 4.77: PPV vs. scaled distance at OLD location (Zone-1). Blue triangles represent modeled PPV (second phase) and orange dots represent measured PPV.

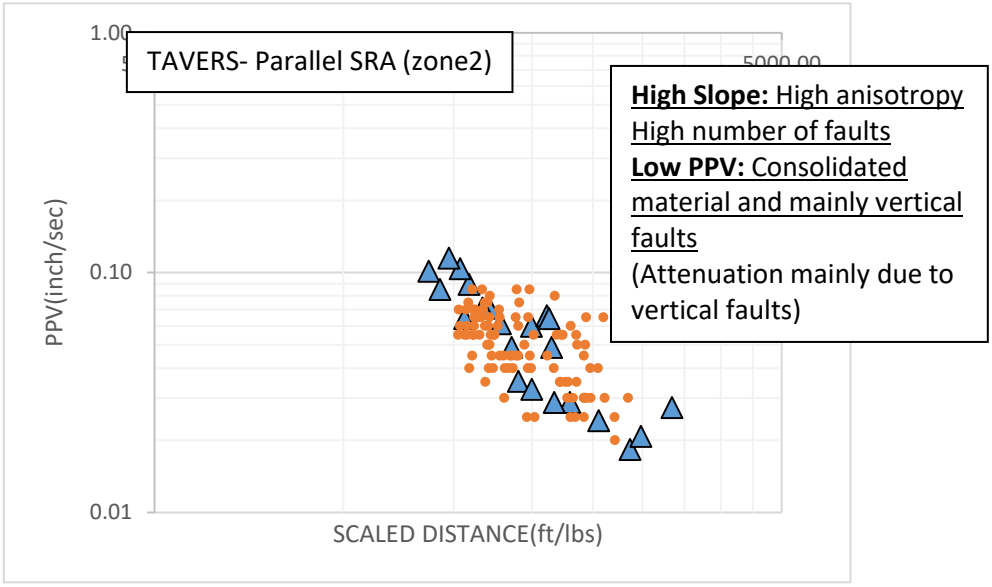

Figure 4.78: PPV vs. scaled distance at TAVERS location (Zone-2). Blue triangles represent modeled PPV (second phase) and orange dots represent measured PPV.

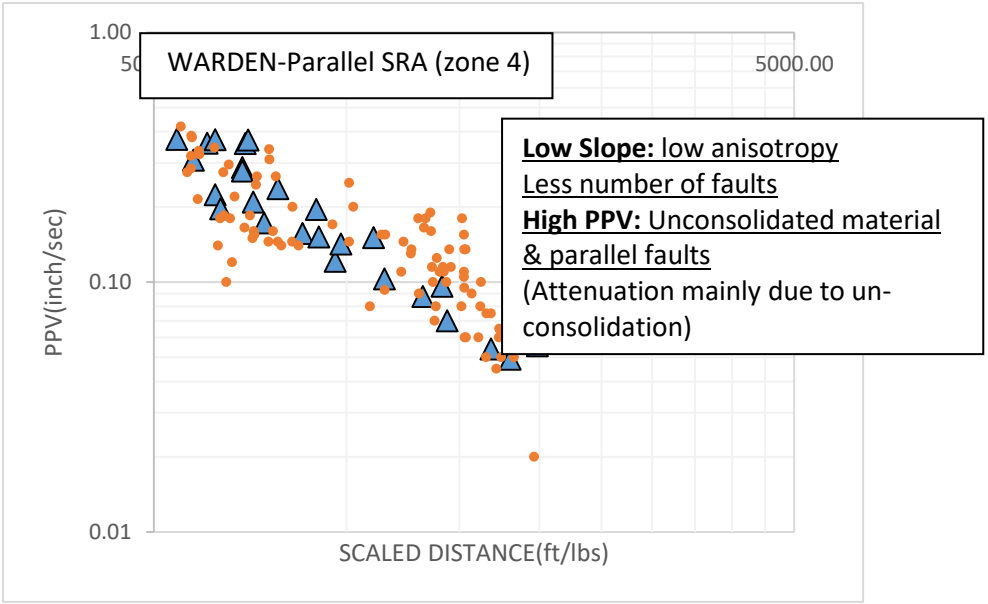

Figure 4.79: PPV vs. scaled distance at WARDEN location (Zone-4). Blue triangles represent modeled PPV (second phase) and orange dots represent measured PPV.

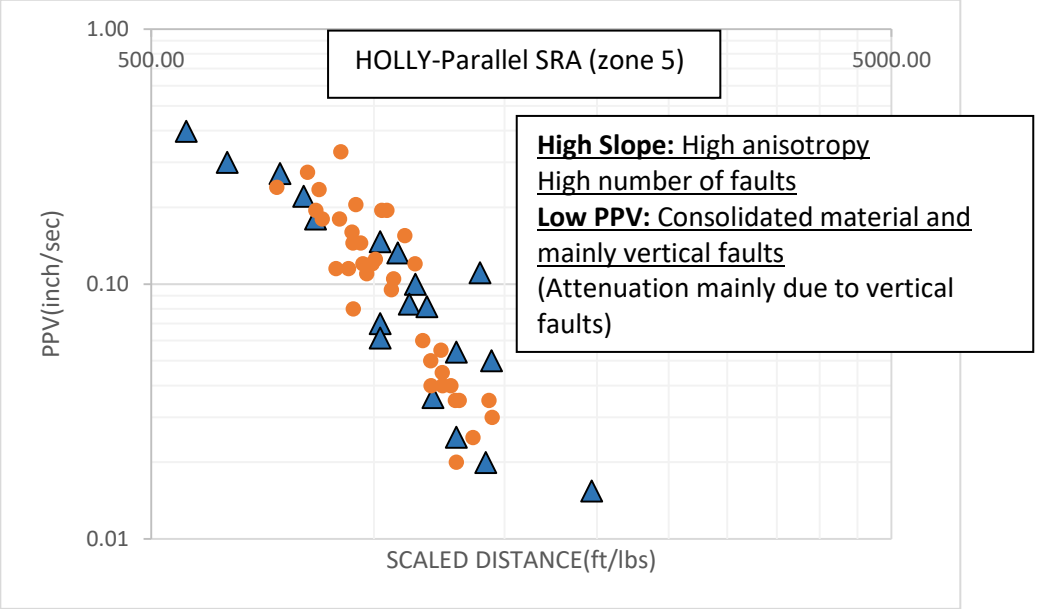

Figure 4.80: PPV vs. scaled distance at HOLLY location (Zone-5). Blue triangles represent modeled PPV (second phase) and orange dots represent measured PPV.

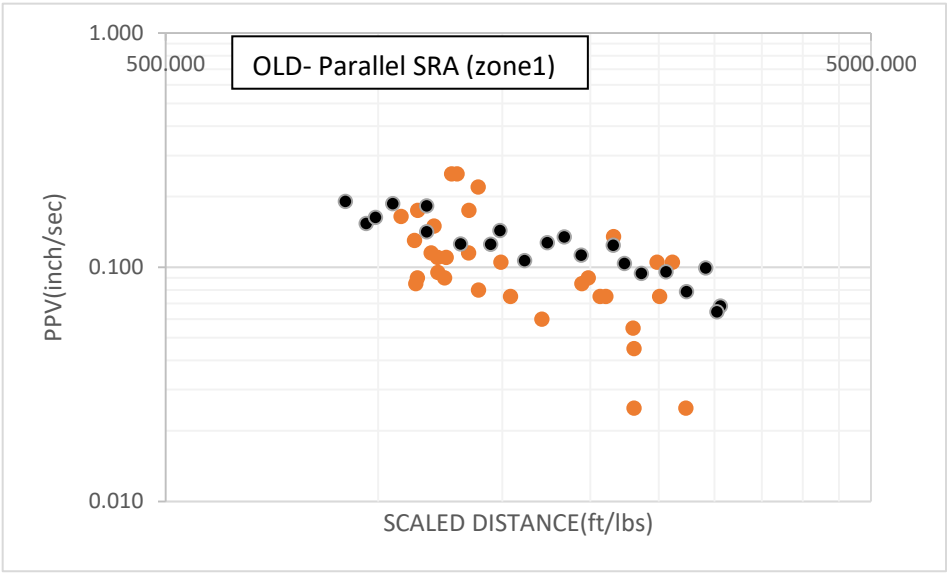

Figure 4.81: PPV vs. scaled distance at OLD location (Zone-5). Black circles represent modeled PPV (first phase) and orange dots represent measured PPV.

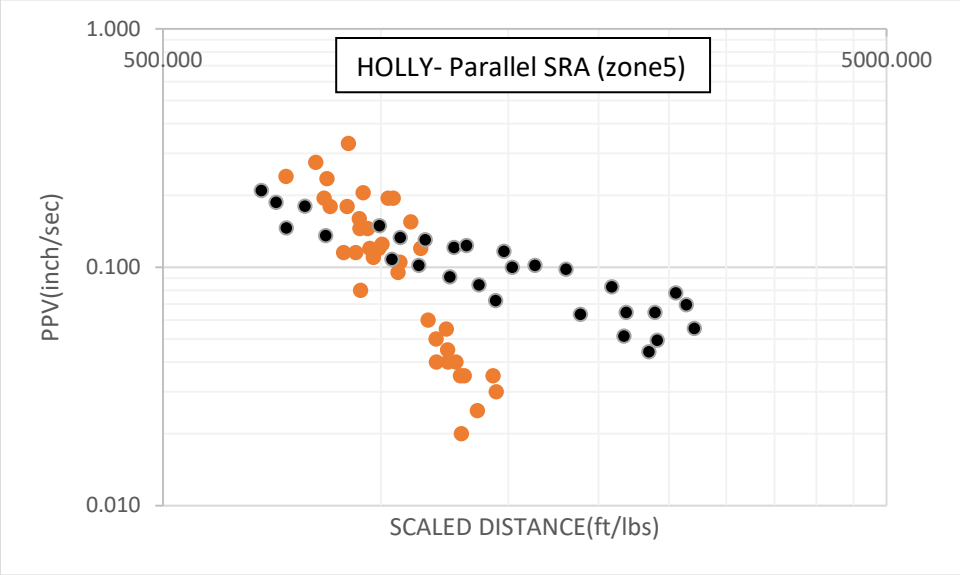

Figure 4.82: PPV vs. scaled distance at HOLLY location (Zone-5). Black circles represent modeled PPV (first phase) and orange dots represent measured PPV.

Figures 4.83-4.4 show the vertical component of velocity as a function of time for selected two events at OLD and Holly locations. Only the first 2 ms is shown in the figures before reflected waves from the artificial lateral boundaries start to interfere with the incoming stress waves. Seismic traces are digitized with sampling rate of 0.002 ms and using the commercial software Didger 3. The figures display examples of seismic traces, particularly comparisons between the modeled and measured data for one blast event at each location. These comparisons were performed using the same scaled distances of 5.5 m/kg.

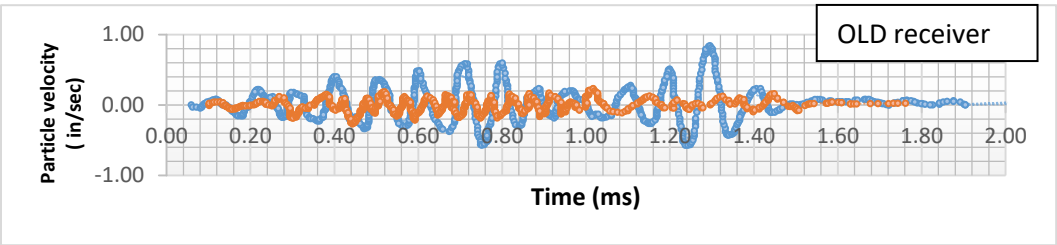

Figure 4.83: Predicted (orange) and measured (blue) vertical particle velocity versus arrival times at OLD location. Low matching is apparent.

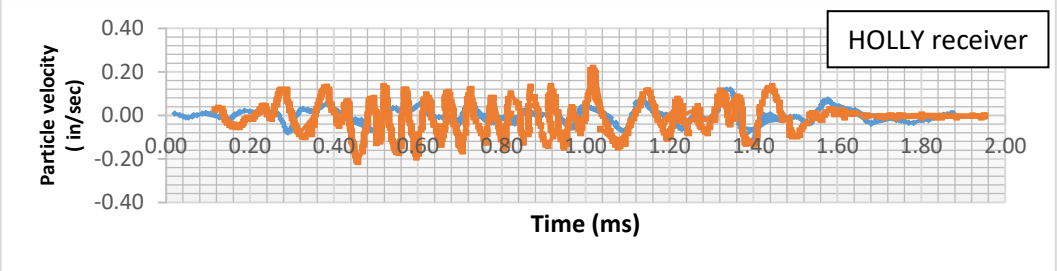

Figure 4.84: Predicted (orange) and measured (Blue) vertical particle velocity versus arrival times at HOLLY location. Relatively good matching is apparent.

Generally, the figures demonstrate that the modelled peak particle velocities for the locations of OLD, TRAVER, WARDEN and HOLLY fall entirely inside the time interval of significant vibrations shown by the field data. Both field data and numerical results show that attenuation is non-linear, as shown by log-log plots. In figure 4.80, as one example the numerical results for the peak particle velocity at HOLLY receiver of zone 5 are compared to measured data. Again, the numerical results fall within the range of measured data for the larger scaled distances, while for lower distances the modeled velocities seems to underestimate the actual peak particle velocity. This result is just a

representative-modeling example, more work would need to be done to draw definite conclusions.

Concerning the three receiver locations, OLD, WARDEN and TAVERS (Figures 4.77 to 4.79) the comparisons show a lower degree of matching comparing to the results from HOLLY, which is attributed to a complex geology at these areas (heterogeneous and anisotropic properties). It is worth mentioning that a linearization over the entire scaled distance range is not accurate, as the attenuation behavior seems to be much more complex than the direct comparison presented here allows for.

The best matching of the four data sets has been reached using the parameters shown in Table 4.25. The matching procedures was performed manually without any automated inversion techniques. However, more complex geological models and advanced inversion techniques are needed in order to simulate realistic geology and thereby increase the correlation factor. Numerical models for the other 18 receivers were tried but they failed to give acceptable correlation factor. The failure in modelling PPV at these receivers is attributed to the assumptions that simplified the geological structure of the study area.

Table 4.25: Optimum Parameters that gave the best correlation factor during the numerical simulation of the four receivers (OLD, TAVERS, WARDEN and HOLLY).

Parameters / Location	TAVERS Zone 2	HOLLY Zone 5	OLD Zone1	WARDEN Zone4
Material	Isotropic	Isotropic	Isotropic	Isotropic
Model Type	Gen Hoek Brown	Gen Hoek Brown	Gen Hoek Brown	Gen Hoek Brown
Av. Young's Modulus(E) (KN/m^3)	50,000	330,000	1,000,000	2,200,000
Av. Poisson's Ratio(v)	0.3	0.3	0.3	0.3
Av. Porosity (%)	25	30	18	21
Av. Intact Rock Parameter	5	10	22	30
Av. Geological Strength Index	26	35	57	76
Av. Uniaxial Compression Strength (KN/m^2)	5,000	23,000	35,000	54,000
Bulk Rock density	1000 (Low)	1200 (Low)	1500 (higher)	1800(higher)

Figures 4.85-4.86 show snapshots of the numerically modelled seismic wave propagation at Holly receiver location. Different colors indicate different PPV in/sec. In view of many uncertainties in the geology of the rock mass, the numerical prediction is considered to agree favorably with the observed data at four locations .The calculated attenuation is, however, severely shifted from that of observed data at most of the receivers. This might be caused by (1) material viscous damping not being included in the calculation; (2) the complicated site conditions are simplified in the numerical model as an equivalent isotropic and homogeneous rock mass. These observations indicate that the applicability of the proposed numerical modeling method and the suitability of using COMSOL and GTS-NX software to simulate blasting of geological media is limited by the accuracy of the input parameters.

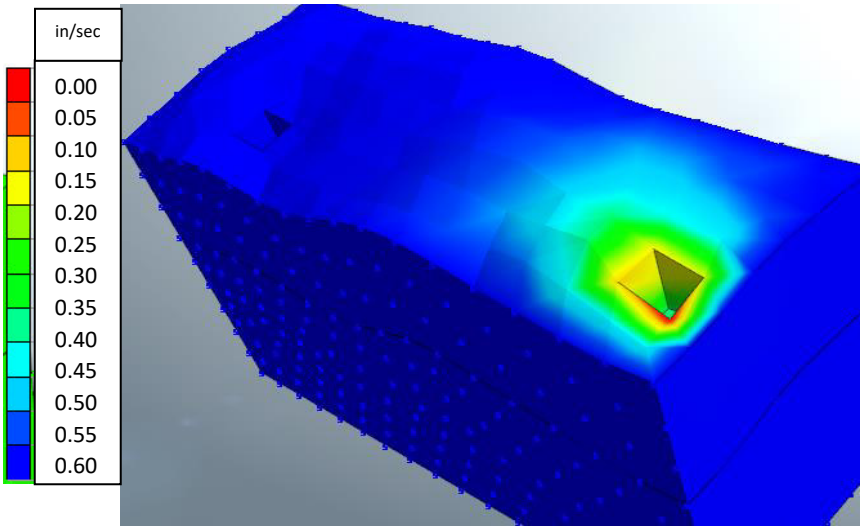

Figure 4.85: Snapshot of the numerically modelled seismic wave propagation at Holly location (time= 0.001s).

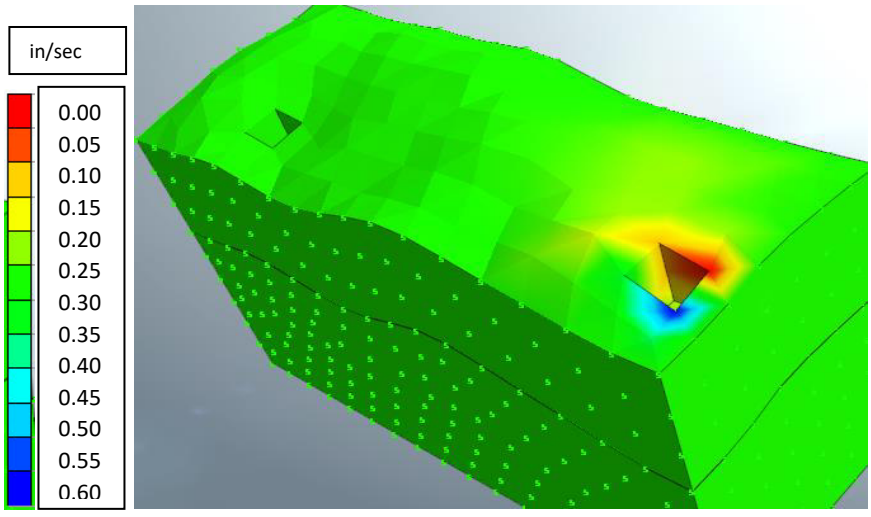

Figure 4.86: Snapshot of the numerically modelled seismic wave propagation at Holly location (time=0.002s).

CHAPTER V

INTERPRETATIONS

The amplitude of ground vibrations at the measuring sites are mainly influenced by the travel path of the propagated elastic wave. These effects are typically related to the attenuation and amplification of seismic waves as they travel across the site. It is generally accepted that there are many factors affecting seismic wave propagation in geological media; these include rock inhomogeneity, fractures (including both joints and faults), source and receiver elastic wave radiation pattern, and the incident angle of the blasting waves with respect to different geological structural boundaries. Attenuation can be enhanced by scattering of the elastic waves at the faces of cracks or pores, bubble movements in partially saturated cracks, liquid flowing into fully saturated cracks, and friction in thin cracks and along grain boundaries (Toksöz,1979). As well, spatial variations in wave phenomena like scattering, spherical divergence, wave focusing, and intrinsic attenuation, can be attributed to spatial variations in geological features, both stratigraphic and tectonic in origin.

All of these factors affect differently the vibration amplitudes and velocities at different locations within the study area. As shown in the previous chapter, three techniques have been used in order to model the wave propagation and to predict PPV values. They include simple empirical equations, the artificial neural networks, and an implementation of the finite element numerical method. A number of geological parameters have been extracted after calibrating the models using the field data (PPV,

propagation velocities). Such parameters include bulk rock density, Young's modulus, Poisson's ratio, porosity, the geological strength index, and uniaxial compressive strength.

Several studies in the literature such as Nolti et al. (1990), Cai et al. (2000), and Ai et al. (2005) describe the effects of discontinuities (i.e. fractures and faults) and spatial variations in bulk rock properties on elastic wave propagation. Based on these studies, five conceptual models are suggested in the current study. An attempt has been made to incorporate most of the factors affecting the vibrations in the study area. In this chapter, interpretation of the best fitting model parameters has been done and it is accompanied with an illustration depicting its relationship to the proposed conceptual geological models. Three modelling lines are followed in the previous chapter, the first is to investigate the effects of individual faults and the second is to consider equivalent material properties for the rock mass. The third approach is to study the effect of different lithologies has been detected. It is worth to be mentioned that, by observing the measured PPV values and the modelled parameters, one finds that the proposed "discontinuous single lithology model with all faults included" has successfully explained the PPV general distribution in the study area.

As previously mentioned, faults, the degree of rock consolidation, and presence of cavities are the most important geological features affecting seismic wave propagation in the study area. Attenuation that is caused by such geological features often result in anisotropy of various parameters, and SRA-dependence of PPV and propagation velocity. Numerous authors in literature such as John (1995) have observed that some regions tend to repeatedly experience stronger ground vibrations than others. This has been attributed

in large part to the soil/rock under these localities being relatively soft. Soft soils amplify the ground vibrations transmitted from seismic sources such as blasting and earthquakes. Therefore, if the region is located on the top of loose materials or soft soils, it is more likely that people and houses living in this area will experience stronger vibrations than others on more consolidated ground at comparable distance from the source. An example similar to blasting vibration is the earthquake effects that occurred in San Francisco (James, 1973). The study shows that many of the same surrounding districts were severely damaged in both the 1906 and 1989 earthquakes. The effects of the underlying rock/soil on the local amplification of ground vibrations is called the site effect. Other factors impact the strength of the ground vibrations at the site as well, including the site's proximity to discontinuities such as faults and fractures. Faults can attenuate the energy of seismic waves severely if the strike direction is perpendicular to the travel path. However, if the fault strike is approximately parallel to the wave propagation direction, vibration amplitudes may increase at certain locations due to the multiple reflection and refraction that traps seismic wave energy inside the fault zone.

Vibrations are usually stronger when the propagation velocity is lower, specifically the S and Raleigh waves. Therefore, amplification of ground vibrations and higher PPV values commonly appear at sites overlying unconsolidated and soft soils. Five soil types have been defined by the National Earthquake Hazards Reduction Program (NEHRP), according to their S-wave velocities (Table 5.1).

Table 5.1: General Classes of rocks/soil according to their S-Wave velocities as described by the National Earthquake Hazards Reduction Program (NEHRP).

General Description	Avreage shear wave velocity to 30m (m/s)
Hard rock	>1500
Rock	760<Vs<1500
Very dense soil and soft rock	360 < V< 760
Siff soil 15 < N<50	180<Vs<360
Soil with more than 3m of soft clay	<180

Generally, the observations can be summarized by five main points: (1) Scattering in the PPV and the low correlation coefficients that were observed in a large number of models (numerically and empirically) indicate a strongly heterogeneous and anisotropic geological medium. Consequently, more complex models are needed to incorporate additional geological structure; (2) The PPV values in the proposed fault zones (zones 1 and 4) are higher than those in the foot/ hanging wall rocks (zones 2 and 5), however the propagation velocity in zones 1 and 4 are higher than in zones 2 and 5; (3) By comparing the PPV values measured inside the same zone at the same scaled distance but at different locations, one finds significant differences. This is attributed to variations in lithology. For example in zone 2, at the same scaled distance, the measured PPV at a clay location is

higher than at limestone location; (4) The interaction of the seismic wave travel paths across one or more of the suggested 5 major faults produces a lower PPV values compared to the PPV produced by fault-parallel travel paths; (5) By performing an initial screening of the PPV modelling results, one finds that when the data sets were separated into paralleled and oblique SRA relative to the suggested faults, the scattering decreased at 8 different locations. Also, the correlation coefficients increased for each receiver location. This helps to confirm the effects of the assumed major faults on the PPV distribution pattern in the study area.

The effects of anisotropic elastic properties in the study area can be shown by the azimuthal dependence of attenuation coefficients for different blasting events and receiver locations. Using eq. (5.1) below, which is modified from equation (5.2) (Triphathy, 2002), it is possible to compensate for the variety of charges and source-receiver distances.

$$PPV2/PPV1 = (SD2/SD1)^{-n} * Exp^{-\alpha (SD2-SD1)} \quad \text{..... Eq. 5.1}$$

$$A2/A1 = (R2/R1)^{-n} * Exp^{-\alpha (R2-R1)} \quad \text{..... Eq. 5.2}$$

where A_0 and Ae are the vibration amplitudes at distances R_0 and Re, respectively; PPV_0 and PPVe are the peak particle velocities at scaled distances of SD_0 and SD_e. R_0 is defined

as the distance between the reference measuring location and the blasting source. While, R_e is the distance between the receiver location and the blasting source. The exponent (N) has been estimated from the best fit empirical equation for each location. The reference PPV_0 has been determined to have a value of 1.2 in /sec .The coefficient of attenuation has been calculated for each shot at the 22 receiver locations and is plotted versus SRA. It worth mentioning that the measurements locations are assumed to fall in the elastic zone away from blasting holes. Consequently, 22 azimuthal plots have been constructed for the wave attenuation coefficients at each of the 22 location. Examples for the 6 main receiver locations are provided below in Figures 5.1 to 5.6.

The anisotropic properties of the study area can be deduced easily from the azimuthal plots. It is observed that the attenuation coefficients of the propagated waves from sources around each location is not constant but changes with the azimuth of the blasting source. This indicates a relationship between the source-receiver azimuth (SRA) and the geological structure which affects the measured PPV values. In large part this can be attributed to multiple reflections of a fault-trapped wave in zones 1 and 4, and wave focusing by constructive interference of the generated signals. Meanwhile, the interaction with vertical fault planes in zone 2 and 5 causes a large dissipation in the transmitted energy and a decrease in vibration magnitudes. The decrease in PPV values has been indicated on the azimuthal plots by a positive attenuation coefficients, while negative attenuation coefficients represent amplified vibrations.

OLD

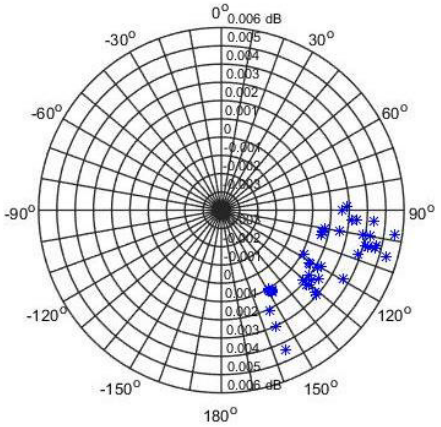

Figure 5.1: Azimuthal pot for the attenuation coefficients of the PPV values measured at OLD receiver.

TAVERS

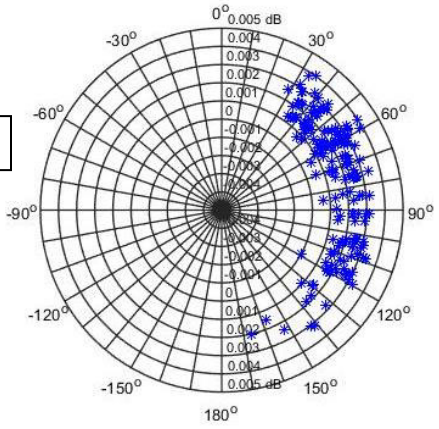

Figure 5.2 Azimuthal pot for the attenuation coefficients of the PPV values measured at TAVERS receiver.

CAIN

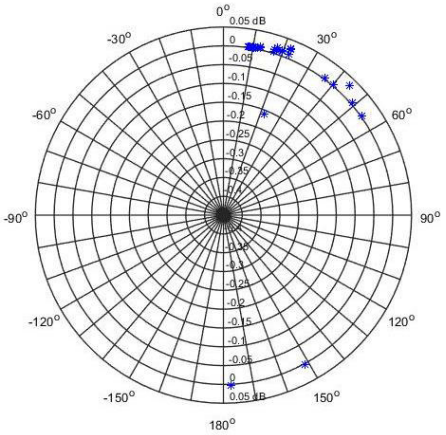

Figure 5.3: Azimuthal pot for the attenuation coefficients of the PPV values measured at CAIN receiver.

HOLLY

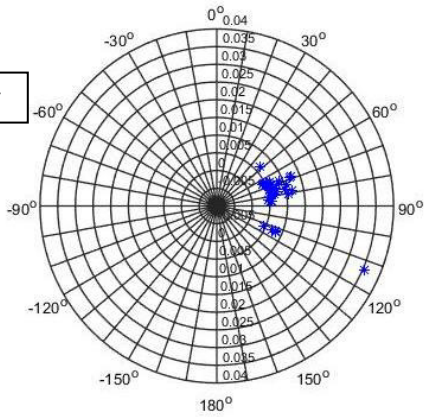

Figure 5.4: Azimuthal pot for the attenuation coefficients of the PPV values measured at HOLLY receiver.

MILDA

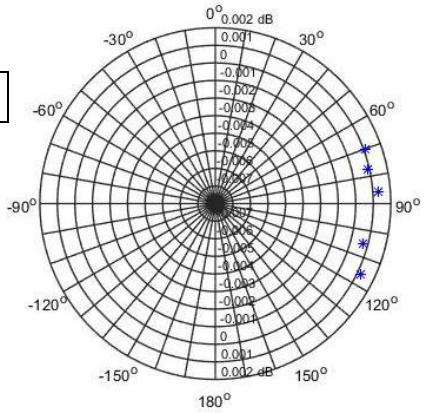

Figure 5.5: Azimuthal pot for the attenuation coefficients of the PPV values measured at MILDA receiver.

WAP

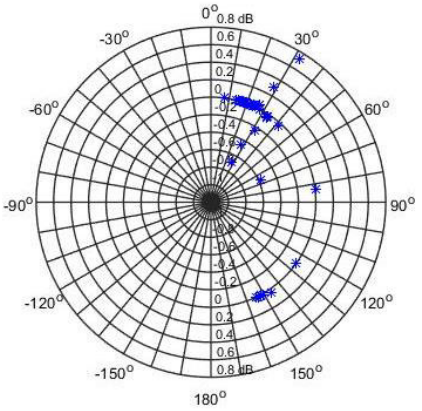

Figure 5.6 Azimuthal pot for the attenuation coefficients of the PPV values measured at WAP receiver.

5.1 Single Lithology Model with No Discontinuities

The argument here is that the study area consists of at least six geological media with different degree of rock consolidation and separated by 5 major normal faults (Figure 5.9), as earlier explained in the conceptual model (chapter 3). In the conceptual model, an assumption is made that the observed PPV differences between the zones are due to dissimilar degree of consolidation and no effects from the major faults. It is also suggested that the media are continuous with no internal fractures or faults. This type of approach combines the effect of the discontinuities and continues geological media into one material with equivalent properties.

In order to test this model the blasts with parallel SRA have been used solely while blasting sources were located inside the boundaries of each zone. This bounds the PPV for only travel paths that have no intersection with the 5 major faults. This was done in order to analyze the average attenuation coefficients of each prescribed zone individually. Thus, the attenuation and amplification will be only a function of the internal geological structure such as degree of consolidation.

Table 5.2 summarize the attenuation coefficients, R-wave velocities and mean PPV for the 22 locations of measurements. Although the histogram of the PPV measured by receivers at OLD (zone 1) and WARDEN (zone 4) shows a higher values, the attenuation coefficients that have been determined by the proposed empirical equation (4.9) gave lower values. In comparison with TAVERS and HOLLY locations in zone 2 and 5 respectively, the attenuation coefficients have high values with a lower mean PPV.

Moreover, the measured R-Wave velocities show higher values in zones with higher PPV (1 and 4) and lower values in zones with lower PPV (2 and 5).

The difference in attenuation trends can be further analyzed by comparing the full waveform response at the OLD and TAVERS locations, as shown in Figures 5.7 and 5.8. These plots correspond to the same scaled distances of 5.5 ft. /lbs. The relevant attenuation plots are shown in Figures 5.10 and 5.11. It can be seen from the figures that the amplitudes of ground vibrations at the OLD location (zone 1) have higher values compared to those from the TAVERS location (zone 2). Similarly, this difference has been found between WARDEN and HOLLY locations in zones 4 and 5, respectively, but with different amplitude ratios.

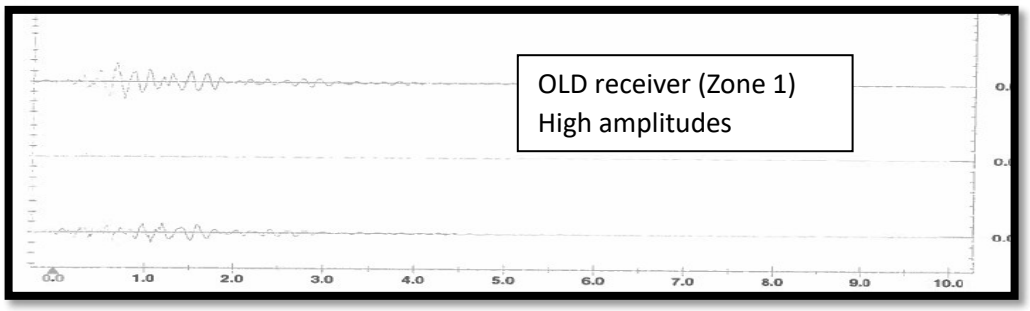

Figure 5.7: Vibration amplitudes arrivals measured in the three mutual directions, vertical, horizontal and radial. (Longitudinal) at OLD location.

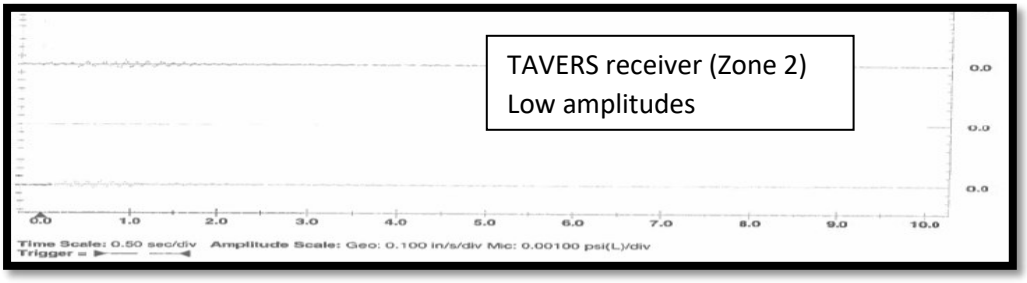

Figure 5.8: Vibration amplitudes arrivals measured in the three mutual directions, vertical, horizontal and radial (Longitudinal) at TAVERS location.

Table 5.2: Calculated parameters (R-wave velocity, attenuation coefficients) from the measured seismogram at each location. Attenuation coefficients empirically by regression.

Location	R-wave velocity (m/s)	Attenuation coefficient (1/m)
CAIN	600	0.005
ESTEVE	250	0.002
HOLLY	480	0.010
KLE	510	0.001
LEE	360	0.025
MAR	310	0.012
MICHELL	500	0.014
MILDA	200	0.021
MILLS	325	0.003
OLD	500	0.004
WOOD	410	0.003
POST	330	0.010
SCHNIEDER	300	0.023
SIDES	415	0.030
SMALL	400	0.100
TAVERS	350	0.021
THOMAS	510	0.100
TIM	420	0.003
WAP	520	0.004
WARDEN	560	0.003
WHITE	350	0.015
WINK	320	0.001

Based on the R-wave velocities, zones 2 and 5 have been interpreted as unconsolidated soil relative to than zones 1 and 4. This is inconsistent with the assumed conceptual model which considers only the degree of consolidation of the host rocks and assumes that higher mean PPV should be accompanied with a lower R-wave velocities. Similarly, zones 1 and 4 have been interpreted as a consolidated soil, which is also unexpected based on the assumed conceptual model. In addition, due to the randomness that appears in the attenuation plots from zones 3 and 6, these are interpreted in large part to be due to geological complexity (discussed in the next sections). It should be also mentioned that the modelling was done in accordance to each individual location being representative of the surrounding geology. Hence, in order to generalize the modelling results, more data acquisition is needed to decrease the uncertainty. This is due to the fact that variations in lithology and structure could exist between adjacent receivers within the same zone

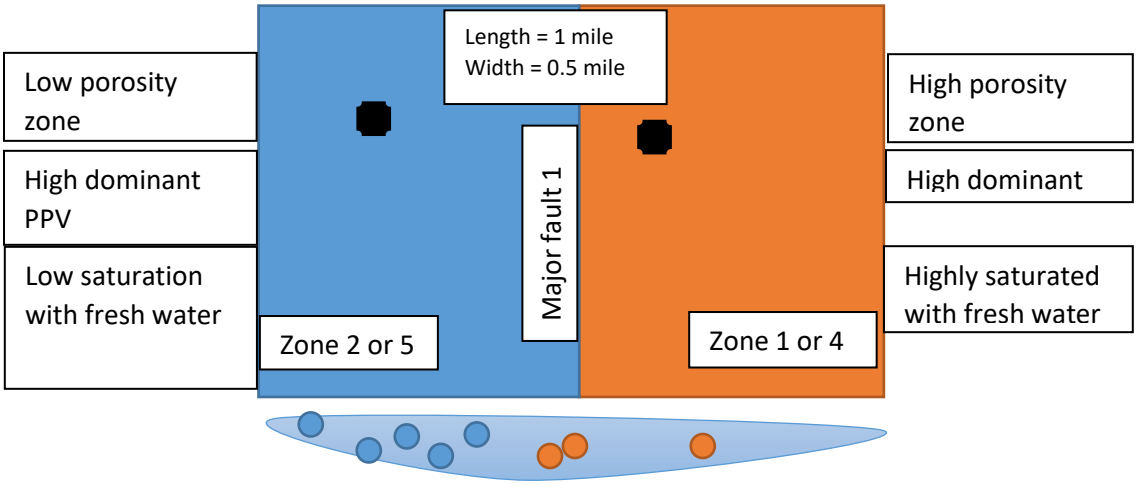

Figure 5.9: Schematic diagram of conceptual Model '1'. Black dots are the receiver location. Yeloow and Blue dots are the shot points.

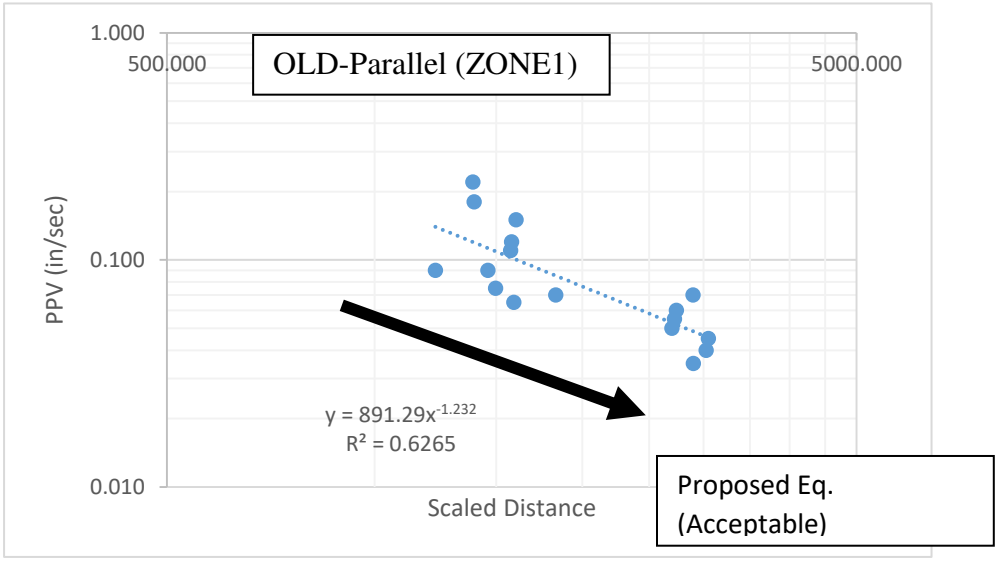

Figure 5.10: PPV vs. the scaled distance at OLD location (Zone-1). Blue dots represent the measured PPV from all SRA. Blue ditched line represent the best-fit line.

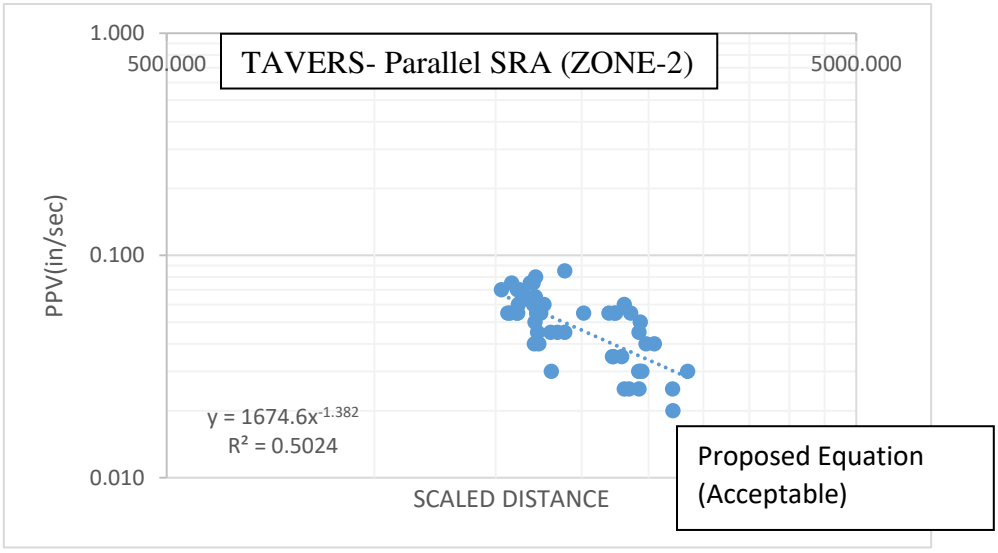

Figure 5.11: PPV vs. the scaled distance at TAVERS location (Zone-2). Blue dots represent the measured PPV from all SRA. Blue ditched line represent the best-fit line.

Although, the elastic moduli that were estimated from the wave propagation simulations numerical models is a beneficial tool in validating the suggested conceptual model for the study area. The numerical wave propagation modelling did not give a good fit for the entire data set in this conceptual model.

5.2 Single Lithology Model with Minor Faults

In this conceptual model, the specified zones of the study area are being assumed to be discontinuous media (Figure 5.12). The differences in PPV values from one zone to another is attributed to internal parallel and oblique faults. The amplification and attenuation of the vibrations could be produced by the interaction of the propagating waves with the faults through multiple reflections, refraction, etc. These effects are investigated by imposing a system of faults with different azimuths into each zone. A number of parallel and semi-paralleled faults within each of the four zones has been numerically modeled and compared to the previous modeling. These modifications increased the fitting of the modelled PPV with the field data. The discontinuities in the study area have thus been categorized into small/internal and macro/boundary faults. Model **'2'** focuses only on testing the effect of the internal fractures within each zone.

It has been described in the literature that the propagation of seismic waves in discontinuous media containing faults can increase or decrease the measured amplitudes in the study area. As observed in Model **1**, the PPV distribution in the area depends on the specified zones and its rock types. Zones 2 and 5 proved to have much higher attenuation than zones 1 and 4. Based on the current proposed model"2", these values are attributed to fractures that intersect the propagated waves by approximately a 90^{o} angle (Figure 5.13).

If the incident angle is perpendicular in this manner, the PPV values will be severely diminished (Zhao, 2006).This type of interaction could be the reason behind the higher attenuation coefficients observed in zones 2 and 5. Also, in the event of a semi-parallel or a parallel fault system, the trapped seismic waves could generate multiple reflection and refraction that would focus the propagated energy (Ben-Zion, 1998). This type of interaction is considered to be the responsible for the increase in PPV values in zones 1 and 4. Trapped waves are usually characterized by large-amplitudes, and consequently also PPV values.

Using this model an improvement has been observed in the correlation coefficients with the measured PPV values. Besides, by observing the elastic modulus, one finds that the average Young's modulus has a lower values due to the effect of the imposed fractures. This is shown in Table 5.3 below.

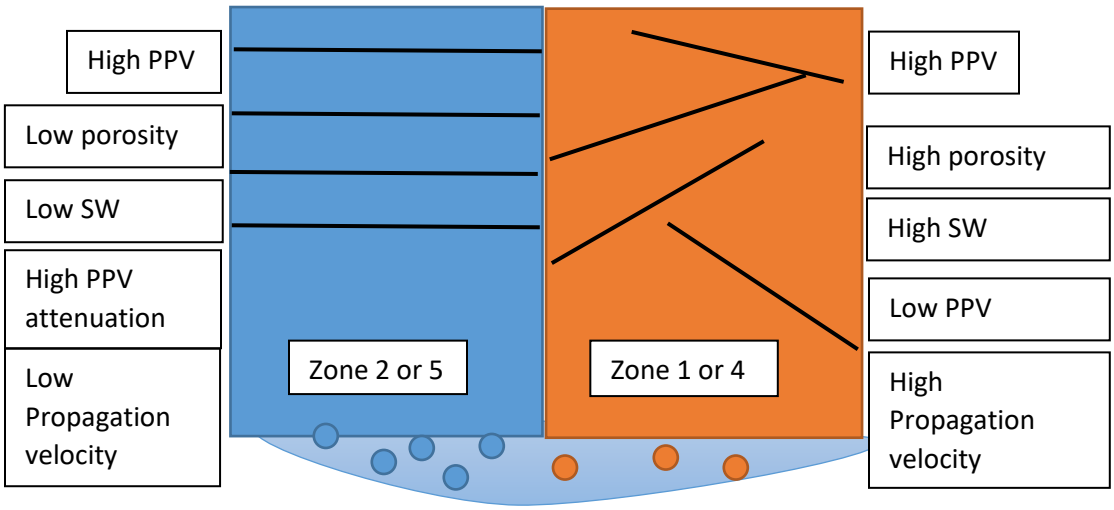

Figure 5.12: Schematic diagram of conceptual Model '2'. Orange and Blue dots are the shot points.Black lines represent the internal faults.

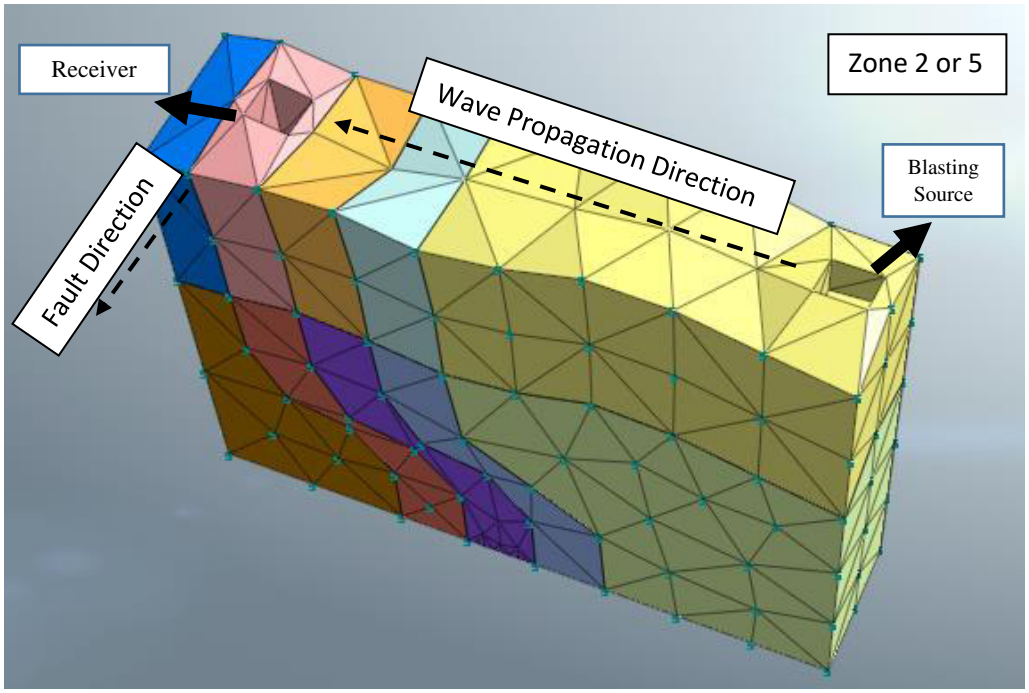

Figure 5.13: Meshed 3-D numerical model with a number of vertical faults in zone 2 or 5. Locations of source and receiver are indicated.

These results are in fact consistent with the propagation velocities of R- waves within the zones. Consequently, zones (1 and 4) have been interpreted as fault zones with loose materials consisting of semi-parallel or oblique internal faults. Zones (2 and 5) showed evidence for more consolidated lithology which is similar to the foot/ hanging wall rocks and intersected by 90^0 angle faults. However, more information is needed to explain the full distribution of the PPV values in the study area.

Table 5.3: Optimum geological Parameters that gave the best correlation coefficients during the numerical simulation of the four receivers (OLD, Tavers, Warden and Holly) considering the conceptual model '2'.

Parameters Location	TAVERS Zone 2	HOLLY Zone 5	OLD Zone1	WARDEN Zone4
Av. Young's Modulus(E) (KN/m^3)	50,000	330,000	1,000,000	2,200,000
Av. Poisson's Ratio(v)	0.3	0.3	0.3	0.3
Av. Porosity (%)	25	30	18	21
Av. Intact Rock Parameter	5	10	22	30
Av. Geological Strength Index	26	35	57	76
Av. Uniaxial Compression Strength (KN/m^2)	5,000	23,000	35,000	54,000
Bulk Rock density	1000 (Low)	1200 (Low)	1500 (higher)	1800 (higher)

5.3 Single Lithology Model with Major Faults

Macro-fractures can sometimes be dominant in a fractured rock mass as far as elastic behavior is concerned. Travel times and amplitudes of seismic waves are influenced by propagation throw rock mass fractures. The closure the deformation of voids inside fractures causing a compliant behavior, and produces the overall deformation of the fracture. Propagate across fracture causing the stress field to be continuous, however due to the fracture deformation the displacement field is discontinuous. As described in chapter 1, factors such as width, intensity and material filling affect the seismic wave transition throw fault zones.

In the study area, 5 macro-fractures, which are assumed to have a strike slightly towards northeast, are presumed to affect the distribution of the PPV. The influence of these major faults on the transmission of the incident ray path has been evaluated by considering the signals measured from shots outside each zone. For example, at the CAIN location, the receiver measures the signals that come from the northern and southern blasts (Figure 5.14). Based on the assumed fault location (Figure 5.16), the results show a significant increase in the attenuation coefficient as the incident angle increase, as shown in Figure 5.15. It should be noted that a few greatly "distorted" data, which are not shown in these figures, were dropped based on scientific judgement when the least squares fitting was carried out. The dropping of those data is justified because they are unlike most of the recorded data and do not seem reasonable. The poor data quality might be due to the malfunction of the recording equipment or lack of proper contact between the sensors and ground. Nevertheless, most data recorded by Vibra-Tech seem reliable. It is worth mentioning that ground coupling effects have been studied by many researchers such as Tae (2004) and Floyd (2001). Based on their results, the changes in PPV in the study area has been interpreted as such, rather than artifacts of uncertain ground coupling.

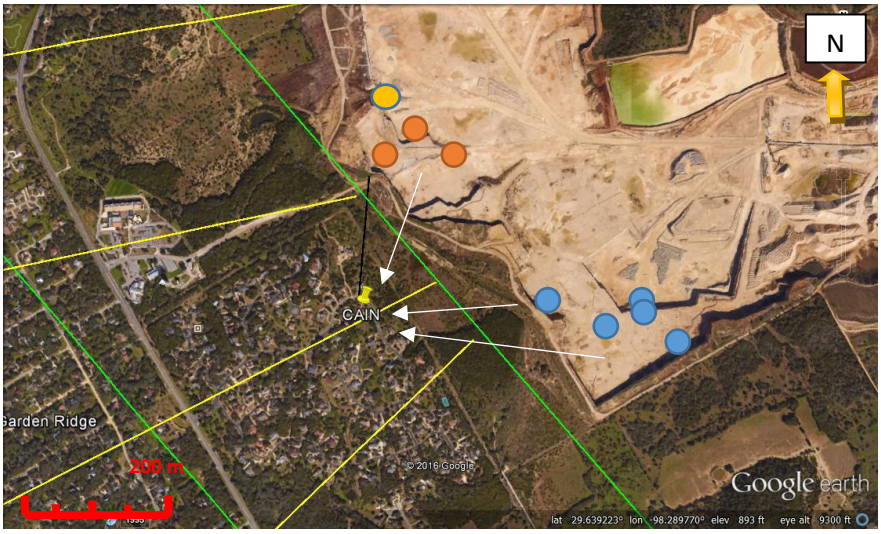

Figurer 5.14: Satellite photo of the study area shows different azimuths of measurements at the CAIN receiver.

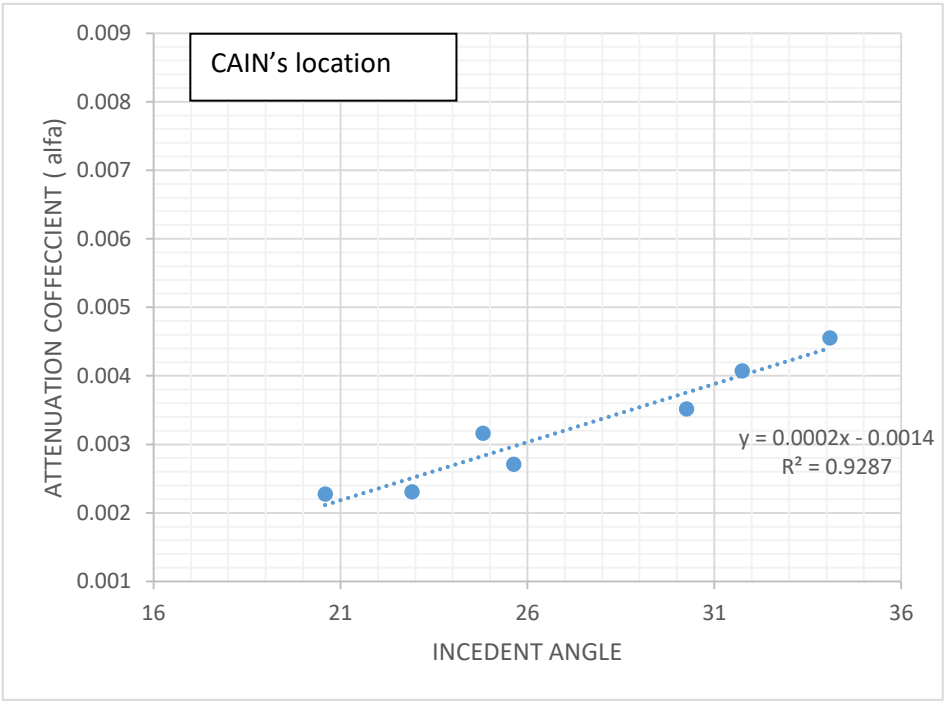

Figure 5.15: Plot of attenuation coefficient versus the incident angle of the SRA for the measured PPV at CAIN location.

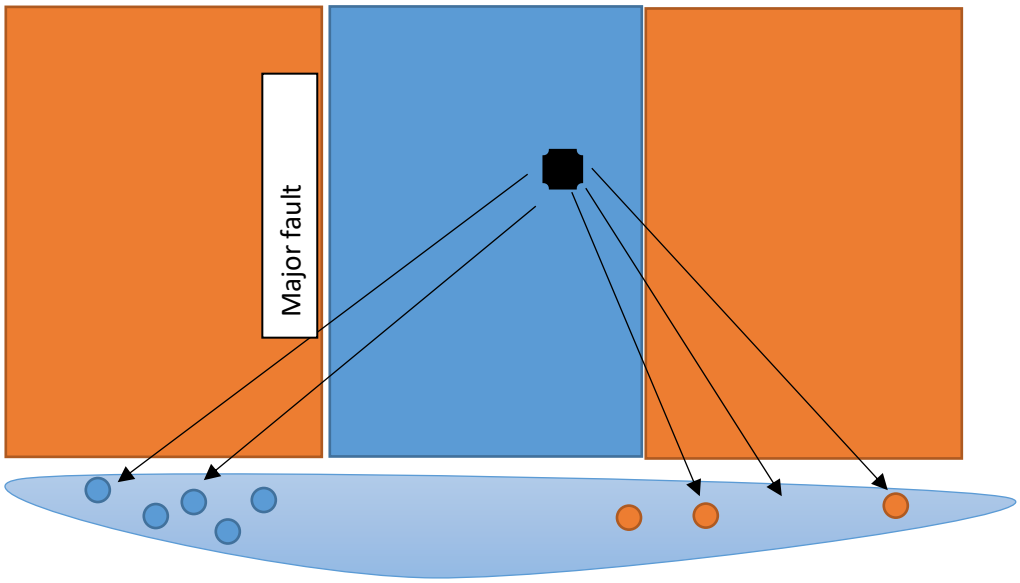

Figure 5.16: Schematic diagram of conceptual Model ‘3’.

5.4 Double Lithology Model with Discontinuities

A PPV amplification was clearly observed at a limited number of locations in the study area, such as in zone 3. Although the PPV values measured in this zone showed a higher degree of scattering during the modelling process, a general trend could be extracted. Figure 5.17 shows a proportional increase in the PPV values along with the scaled distance at three receiver locations SIDES, MILDA and ESTEVE. This increase can be attributed to the propagation of seismic waves through interfaces between different lithology. Juxtaposition of layers are common in the study are due to the normal fault system. This heterogeneity allows the waves to be transferred from a low PPV unit (Edwards limestone) into a high PPV unit (Delrio clay) (Figure 5.18 and 5.19).The transmission and the amplification effect was earlier studied in general by various authors such as Sheriff (1975).

An extensive investigation of the surface geology in zone 3 showed that the receivers in that area are located on Delrio clay while the shot points are located on the Edwards limestone. Consequently, the R-wave velocity contrast between Edwards limestone formation with the Delrio clay is considered to be the chief reason for the PPV amplification effect. In other words, as the wave is transmitted from the higher propagation velocity unit (such as Edward limestone) to the lower velocity unit (Delrio clay) the vibration amplitude will be intensified.

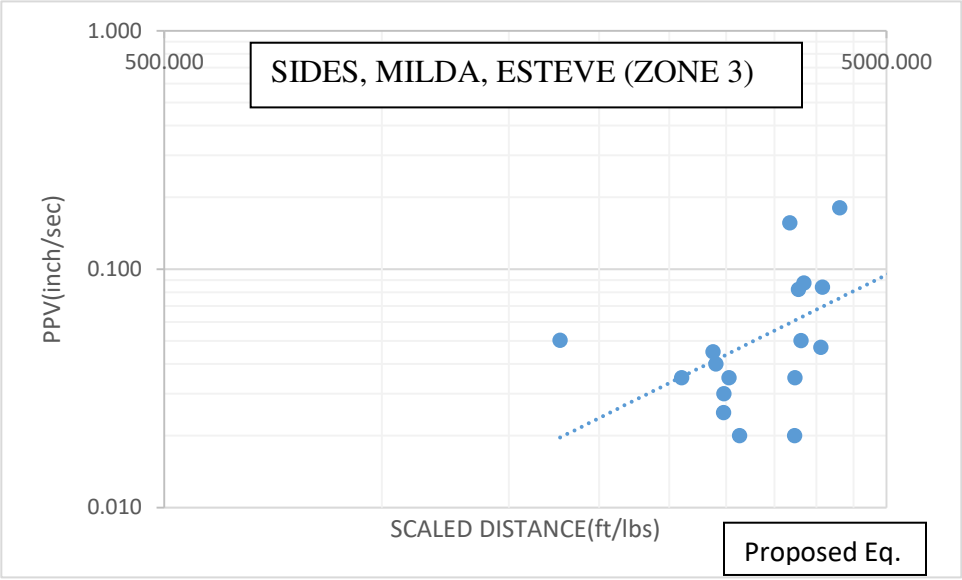

Figure 5.17: Plot of PPV versus the scaled distance for all receivers in zone 3.

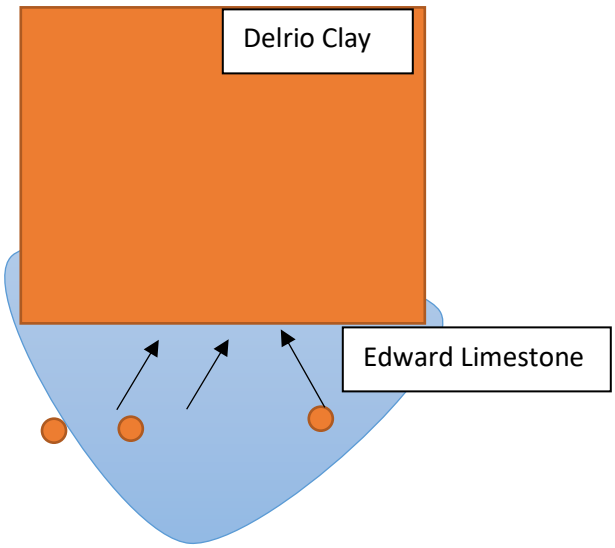

Figure 5.18: Schematic diagram of conceptual Model '4'.

Figure 5.19: Satellite image of the study area showing the location of ESTEVE receiver.

5.5 Topographic Irregularities Model

Another possible explanation for PPV enhancement is topographic and surface irregularity effects which can amplify seismic wave amplitudes. For example, the influence of the alluvial depositional environment surface topography on seismic wave amplification was found to be large by Francisco (1983). He investigated the phenomena of elastic waves scattering and focusing by surface irregularities of a three-dimensional half space using a numerical boundary method. Figure 5.20 shows a vertical cross section (A-B) across the study area. Topographic and geological irregularities can be seen on the surface which increase the probability of wave focusing by the surface topographic shape.

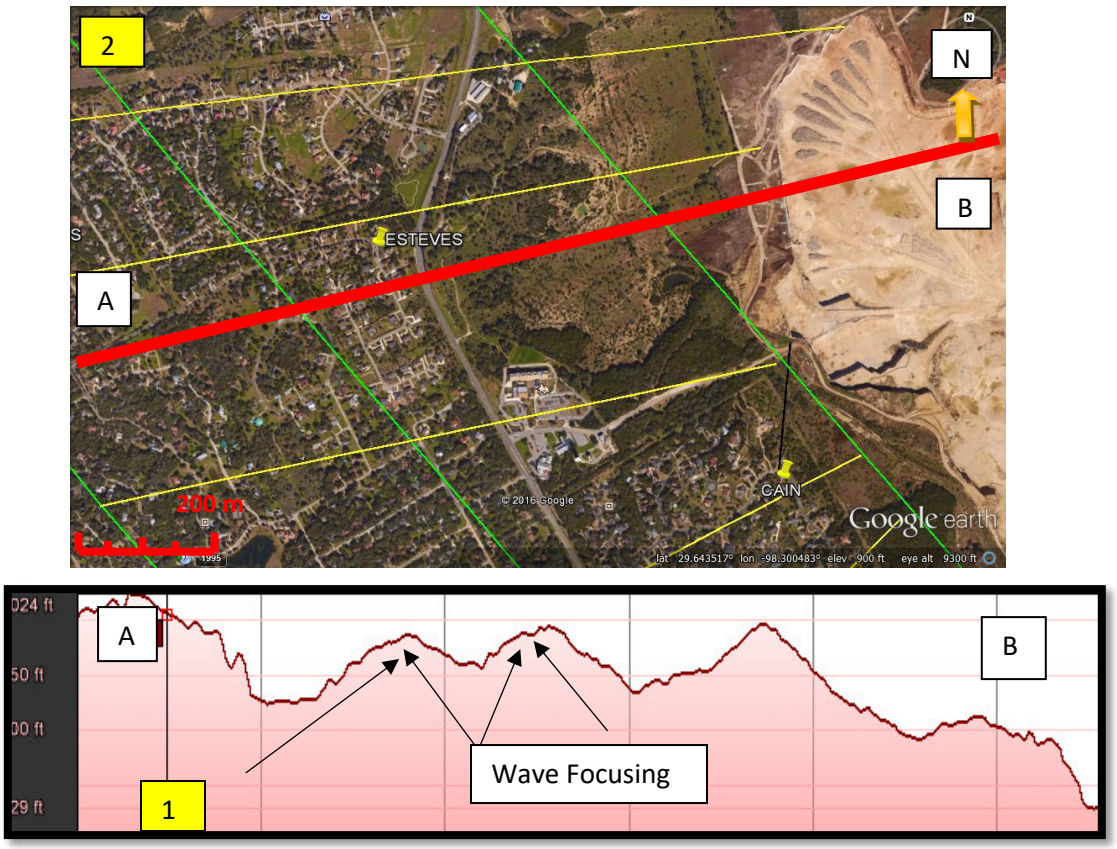

Figure 5.20: 1) Elevation profile showing the surface irregularities of the study area. 2) Actual map show profile location.

CHAPTER VI

CONCLUSION

Environmental issues arising from blasting increasingly restrict quarrying operations. Therefore, monitoring the shots and measurements of ground vibrations are extremely important in order to eliminate a wide array of potential environmental problems. Since PPV is the most commonly used vibration parameter for regulating blast designs, its prediction and interpretation constituted the objective of this study. Three approaches have been used namely, empirical equations, artificial neural networks (ANN), and the finite element numerical method for seismic wave propagation. These approaches have been applied to over 600 seismic events which were recorded by 22 receivers from approximately 200 blasts within the Hanson-Servtex Quarry, Garden Ridge city, Texas (between years 2012-2015).

Nine empirical relationships including a new proposed equation (4.9) have been tested by applying non-regression analysis on the PPV measured at the above-mentioned 22 locations. The proposed empirical equation was successful in predicting the PPV at 12 different locations within the study area with an acceptable correlation factor of '0.4'. Amongst all of the used approaches, ANN exhibited the highest correlation factors for the predicted PPV. Moreover, Feedforward Backpropagation proved to be the most suitable network type for PPV prediction. Additionally, Neural Network topology with 5 neurons and 1 or 2 hidden layers was revealed to be applicable for the prediction in most of the receivers' regions. With reference to the finite element analysis method, only vibration

amplitudes at 4 locations have been successfully predicted with a correlation factor of more than ‘0.4‘.

Understanding the controlling geological factors affecting the distribution of PPV in the study area has been considered a second objective of this study. Based on the background geology, complaints distribution, and the measured data (PPV, propagation velocity, and the attenuation coefficients), five conceptual models were proposed in an attempt to explain spatial variations of PPV amplification and attenuation in the study area. These models provided an initial step for advanced modelling. A proposed single lithology model with major and minor internal fault provided the best matching to the measured data. Based on this model, the study has been mechanically divided into six zones. In addition, lower PPV values were attributed to the presence of fractures intersecting the propagating waves by an oblique angle. This type of interaction could be the reason behind the higher attenuation coefficients and lower propagation velocities observed in both zones 2 and 5. These two zones have been interpreted as being host rocks with highly consolidated material.

In zones 1 and 4, a number of semi-parallel and parallel internal faults that caused seismic waves to become trapped entrapment were considered the reason behind the higher PPV values. This phenomenon involves the production of multiple reflections and refractions that focus vibration energy at some locations. These two zones have likewise been inferred as secondary fault zones within the Balcones normal fault system.

Finally, this study is could have a major impact on PPV prediction values to provide relief and prevent any possible damage or annoyance to the surrounding people and

infrastructure. More specifically, it is believed that these models can have a significant role as a practical guide for future blasting operations at the Hanson- Servtex quarry.

REFERENCES

Abbott, P.L., 1975. On the hydrology of the Edwards Limestone, south-central Texas. Journal of Hydrology 24, 251-269.

Ambraseys, N., 1968. Rock mechanics in engineering practice.

Amick, H., Gendreau, M., 2000. Construction vibrations and their impact on vibration-sensitive facilities. 6, 4-5.

Bakhsandeh Amnieh, H., Mohammadi, A., Mozdianfard, M., 2013. Predicting peak particle velocity by artificial neural networks and multivariate regression analysis-Sarcheshmeh copper mine, Kerman, Iran. Journal of Mining and Environment 4, 125-132.

Ben-Menahem, A., Singh, S.J., 2012. Seismic Waves and Sources. Springer Science & Business Media.

Biot, M.A., 1956. Theory of propagation of elastic waves in a fluid-saturated porous solid. I. Low-frequency range. J. Acoust. Soc. Am. 28, 168-178.

Bodare, A., (1981), "Trafik-alstrade vagor och . vibrationer" (in Swedish), Report Teknikum Uppsala University, UPTEC 81 45 R.
Butler, D.K., 2005. Near-Surface Geophysics. Society of Exploration Geophysicists Tulsa.

Case, E.D., Smyth, J., Hunter, O., 1980. Grain-size dependence of microcrack initiation in brittle materials. J. Mater. Sci. 15, 149-153.

Choquette, P.W., Pray, L.C., 1970. Geologic nomenclature and classification of porosity in sedimentary carbonates. AAPG Bull. 54, 207-250.

Cleveland, J., Bradt, R., 1978. Grain size/microcracking relations for pseudobrookite oxides. J Am Ceram Soc 61, 478-481.

Crampin, S., 1978. Seismic-wave propagation through a cracked solid: polarization as a possible dilatancy diagnostic. Geophysical Journal International 53, 467-496.

Crawford, R., Ward, H., 1965. Dynamic strains in concrete and masonry walls. Building Research Note 54, 14.

Demuth, H., Beale, M., 1993. Neural network toolbox for use with MATLAB.

Dowding, C.H., 1993. Blast vibration monitoring for rock engineering. Comprehensive Rock Engineering, Hudson (Ed.), Pergamon Press, Oxford 4, 111-135.

Dowding, C.H., Dowding, C., 1996. Construction Vibrations. Prentice Hall Upper Saddle River, NJ.

Draper, N., Smith, H., 1966. 1966 Applied regression analysis. New York.

Duvall, W.I., Fogelson, D.E., 1962. Review of Criteria for Estimating Damage to Residences from Blasting Vibrations. US Department of the Interior, Bureau of Mines.

Edwards, A.T., Northwood, T., 1960. Experimental Studies of the Effects of Blasting on Structures. Division of Building Research, National Research Council.

Ferrill, D.A., McGinnis, R.N., Morris, A.P., Smart, K.J., Sickmann, Z.T., Bentz, M., Lehrmann, D., Evans, M.A., 2014. Control of mechanical stratigraphy on bed-restricted jointing and normal faulting: Eagle Ford Formation, south-central Texas. AAPG Bull. 98, 2477-2506.

Ferrill, D.A., Sims, D.W., Waiting, D.J., Morris, A.P., Franklin, N.M., Schultz, A.L., 2004. Structural framework of the Edwards Aquifer recharge zone in south-central Texas. Geological Society of America Bulletin 116, 407-418.

George, W.O., Hastings, W.W., Breeding, S.D., 1947. Geology and ground-water resources of Comal County, Texas.

George, W.O., Seth, D., Hastings, W.W., 1952. Geology and ground-water resources of Comal County, Texas, with sections on Surface-water supplies and Chemical character of the water.

Gupta, R., Roy, P.P., Singh, B., 1988. Prediction of peak particle velocity and peak air pressure generated by buried explosion. International Journal of mining and geological engineering 6, 15-26.

Hao, H., Wu, Y., Ma, G., Zhou, Y., 2001. Characteristics of surface ground motions induced by blasts in jointed rock mass. Soil Dyn. Earthquake Eng. 21, 85-98.

Hoek, E., 1983. Strength of jointed rock masses. Geotechnique 33, 187-223.

Hoek, E., 1988. The Hoek-Brown failure criterion-a 1988 update. , 31-38.

Hoek, E., Brown, E.T., 1980. Empirical strength criterion for rock masses. J. Geotech. Geoenviron. Eng. 106.

Hoek, E., Brown, E.T., 1997. Practical estimates of rock mass strength. Int. J. Rock Mech. Min. Sci. 34, 1165-1186.

Kaneko, Y., Lapusta, N., Ampuero, J., 2008. Spectral element modeling of spontaneous earthquake rupture on rate and state faults: Effect of velocity-strengthening friction at shallow depths. Journal of Geophysical Research: Solid Earth 113.

Khandelwal, M., Singh, T., 2006. Prediction of blast induced ground vibrations and frequency in opencast mine: a neural network approach. J. Sound Vibrat. 289, 711-725.

King, M., Myer, L., Rezowalli, J., 1986. Experimental studies of elastic-wave propagation in a columnar-jointed rock mass. Geophys. Prospect. 34, 1185-1199.

Langhaar, H.L., 1951. Dimensional Analysis and Theory of Models. Wiley New York.

Li, Y., Leary, P., 1990. Fault zone trapped seismic waves. Bulletin of the Seismological Society of America 80, 1245-1271.

Li, Y., Vidale, J.E., 1996. Low-velocity fault-zone guided waves: numerical investigations of trapping efficiency. Bulletin of the Seismological Society of America 86, 371-378.

Lo, W., 2008. Propagation and attenuation of Rayleigh waves in a semi-infinite unsaturated poroelastic medium. Adv. Water Resour. 31, 1399-1410.

Maclay, R.W., 1995. Geology and hydrology of the Edwards Aquifer in the San Antonio area, Texas .

Maclay, R.W., Small, T.A., 1976. Progress report on geology of the Edwards Aquifer, San Antonio area, Texas, and preliminary interpretation of borehole geophysical and laboratory data on carbonate rocks .

Massarsch, K., 1993. Man-made vibrations and solutions.

Mavko, G., Mukerji, T., Dvorkin, J., 2009. The Rock Physics Handbook: Tools for Seismic Analysis of Porous Media. Cambridge university press.

Medearis, K., 1977. The development of rational damage criteria for low-rise structures subjected to blasting vibrations.

Meireles, M.R., Almeida, P.E., Simões, M.G., 2003. A comprehensive review for industrial applicability of artificial neural networks. IEEE Trans. Ind. Electron. 50, 585-601.

Mortazavi, A., Katsabanis, P., 2001. Modelling burden size and strata dip effects on the surface blasting process. Int. J. Rock Mech. Min. Sci. 38, 481-498.

Nicholls, H.R., Johnson, C.F., Duvall, W.I., 1971. Blasting Vibrations and their Effects on Structures. US Government Printers.

Oriard, L., 1982. Blasting effects and their control. Underground Mining Methods Handbook , 1590-1603.

Oriard, L.L., 1999. The Effects of Vibrations and Environmental Forces: A Guide for the Investigation of Structures. International Society of Explosives Engineers (ISEE).

Poggi, V., Fäh, D., 2010. Estimating Rayleigh wave particle motion from three-component array analysis of ambient vibrations. Geophysical Journal International 180, 251-267.

Popp, T., Kern, H., 1994. The influence of dry and water saturated cracks on seismic velocities of crustal rocks-a comparison of experimental data with theoretical model. Surv. Geophys. 15, 443-465.

Rose, P., 1972. Edwards Formation, surface and subsurface, Central Texas: Austin, Texas, University of Texas Bureau of Economic Geology. Report of Investigations 74, 197.

Rüger, A., 1997. P-wave reflection coefficients for transversely isotropic models with vertical and horizontal axis of symmetry. Geophysics 62, 713-722.

Semblat, J.F., Pecker, A., 2009. Waves and vibrations in soils: earthquakes, traffic, shocks, construction works. Waves and vibrations in soils: Earthquakes, Traffic, Shocks, Construction works, 500 p.

Sibson, R., 1977. Fault rocks and fault mechanisms. Journal of the Geological Society 133, 191-213.

Silva-Castro, J., 2012. Blast vibration modeling using improved signature hole technique for bench blast.

Small, T.A., Hanson, J.A., 1994. Geologic framework and hydrogeologic characteristics of the Edwards Aquifer outcrop, Comal County, Texas.

Small, T.A., Hanson, J.A., 1998. Geologic Framework and Hydrogeologic Characteristics of the Edwards Aquifer Outcrop, Comal County, Texas.

Stein, W.G., Ozuna, G.B., 1995. Geologic framework and hydrogeologic characteristics of the Edwards Aquifer recharge zone, Bexar County, Texas.

Toksöz, M.N., Cheng, C.H., Timur, A., 1976. Velocities of seismic waves in porous rocks. Geophysics 41, 621-645.

Tripathy, G., Gupta, I., 2002. Prediction of ground vibrations due to construction blasts in different types of rock. Rock Mech Rock Eng 35, 195-204.

United States. Bureau of Mines, Siskind, D., 1980. Structure Response and Damage Produced by Ground Vibration from Surface Mine Blasting. US Department of the Interior, Bureau of Mines.

University of Texas. Bureau of Economic Geology, Barnes, V.E., 1979. Geologic Atlas of Texas: Seguin Sheet. University of Texas at Austin, Bureau of Economic Geology.

Veni, G., 1994. Hydrogeology and evolution of caves and karst in the southwestern Edwards Plateau, Texas. The Caves and Karst of Texas, William R.Elliot and George Veni, eds., National Speleological Society, 13-30.

Veni, G., 1995. Revising the boundaries of the Edwards (Balcones Fault Zone) aquifer recharge zone: Water for Texas. , 99-107.

Wang, Z., 1990. Laboratory measurements and applications of seismic velocities.

Wiss, J., Linehan, P., 1978. Control of vibration and blast noise from surface coal mining.Volume II.Open file report (final) 1 July 1975-28 February 1978.

Yan, W.M., Tham, L.G., Yuen, K., 2013. Reliability of empirical relation on the attenuation of blast-induced vibrations. Int. J. Rock Mech. Min. Sci. 59, 160-165.

Zisman, W.A., 1933. Comparison of the Statically and Seismologically Determined Elastic Constants of Rocks. Proc. Natl. Acad. Sci. U. S. A. 19, 680-686.

Cai, Y., Gould, P., Desai, C., 2000. Nonlinear analysis of 3D seismic interaction of soil–pile–structure systems and application. Eng. Struct. 22, 191-199.

Toksöz, M., Johnston, D., Timur, A., 1979. Attenuation of seismic waves in dry and saturated rocks: I. Laboratory measurements. Geophysics 44, 681-690.

Ai, Y., Zhao, D., Gao, X., Xu, W., 2005. The crust and upper mantle discontinuity structure beneath Alaska inferred from receiver functions. Phys. Earth Planet. Inter. 150, 339-350.

Ben-Zion, Y., 1998. Properties of seismic fault zone waves and their utility for imaging low-velocity structures. Journal of Geophysical Research: Solid Earth 103, 12567-12585.

Sheriff, R.E., 1975. Factors affecting seismic amplitudes. Geophys. Prospect. 23, 125-138.